Characterization of Viral inhibiting 2D Carbon-based structures using Scanning Probe Microscopy and Raman Spectroscopy

Dissertation

zur Erlangung des akademischen Grades

doctor rerum naturalium

(Dr. rer. nat.)

im Fach Physik

Spezialisierung: Experimentalphysik

eingereicht an der

Mathematisch-Naturwissenschaftlichen Fakultät

Humboldt-Universität zu Berlin

Von

M.Sc. Mohammad Fardin Gholami

Präsidentin/Präsident der Humboldt-Universität zu Berlin

Prof. Dr. Julia von Blumenthal

Dekanin/Dekan der Mathematisch-Naturwissenschaftlichen Fakultät

Prof. Dr. Caren Tischendorf

Gutachter:

1. Prof. Dr. Jürgen P. Rabe
2. Prof. Dr. Oliver Benson
3. Prof. Dr. Dieter Neher

Tag der mündlichen Prüfung: 22.11.2023

Contents

List of Abbreviations

1D	1-Dimensional
2D	2-Dimensional
3D	3-Dimensional
SLG	Single Layer Graphene
TRGO	Thermally Reduced Graphene Oxide
GO	Graphene Oxide
VSV	Vesicular Stomatitis Virus
SFM	Scanning Force Microscopy
SFM-QI	Quantitative Imaging Mode Scanning Force Microscopy
SFM-QNM	Scanning Force Microscopy in Quantitative Nanomechanical Mapping
STM	Scanning Tunnelling Microscopy
dPG	Dendritic Polyglycerol
dPGS	Dendritic Polyglycerol Sulfate
hPG	Hyperbranched Polyglycerol
hPGS	Hyperbranched Polyglycerol Sulfate
PFTUNA	Peak Force Tunneling current
I-V curve	Current vs Voltage Curve
PBS	Phosphate Buffer Solution
BHK	Baby Hamster Kidney
HSV-1	Herpes Simplex Virus Type 1
EHV-1	Equine Herpes Virus Type 1

Table of Figures

Abstract

The activity of matter can be ascribed to a system, consisting of individually active components, which exhibit a collective behavior. Multivalent interactions are common in the activity of matter. They are based on the cooperation of many individual local bindings leading to multivalent bonds and consequently emerging behaviors of matter at various scales in nature. Controlling and precise adding of multivalency to nanomaterials is the route towards a bottom-up approach to designing them, based on form and consequent functions. Therefore, understanding the structure and control of specific activities and functionalities of those nanomaterials are of great interest and necessary for further advancement of active materials and interfaces in various biological and sensor applications.

Multivalency of nanomaterials render them useful for biological mimicking and viral inhibition applications. Only precise control and comprehension of their multivalent interactions allow for designing them with advantageous efficiency of interactions. Due to the large surface area of two-dimensional multivalent platforms, the overall required concentration reduces for efficient binding with the material of interest. 2D carbon-based nanosheets such as graphene and graphene oxide can be great candidates for multivalent platforms of high efficiency but adding controlled and precise multivalency to them is very difficult. Graphene oxide contains many chemical functional groups, randomly distributed in terms of type, number and position within its structure. However, bio-interactions of those chemical functional groups are non-specific, leading to non-reproducible and complex interactions for graphene oxide. In addition, further chemical modifications of the 2D graphene nano sheets affect their electronic properties and may hinder their scope of applications in sensors and active interfaces. Therefore, understanding how novel multivalent functionalization methods affect the 2D carbon-based sheets of graphene in terms of their geometry, physical interaction specificity, and their electronic properties, is the goal of this thesis as they are highly necessary for advancement of bottom-up design of 2D nanomaterials of the future.

The objective of this thesis is to investigate two novel methods of modifying 2D graphene nanosheets through "graft to" and "graft from" techniques, which involve [2+1] nitrene cycloaddition reactions at ambient conditions and ring-opening multibranch polymerization of glycerol, respectively. These modified nanosheets were then studied for their interaction with viral particles such as vesicular stomatitis virus

(VSV) using scanning probe microscopy. The findings reveal that only sulfated post-functionalized 2D TRGO sheets were able to strongly bind to VSV and other enveloped viral particles. The results also suggest that the 2D multivalent binding of functionalized TRGO sheets with viral envelopes is mostly due to non-specific electrostatic interactions, similar to that of the extracellular matrix of a cell. However, further specialization of these interactions is possible through the variation of post-functionalization molecules. Overall, this study sheds light on the potential of functionalized graphene nanosheets in various applications, particularly in the field of virology, and provides valuable insights for future research.

Scanning probe microscopy surprisingly revealed that while functionalized 2D TRGO could bind to VSV particles and remains flexible enough to wrinkle on a flat mica interface, they were unable to completely wrap the envelope proteins surrounding the viral particles. This is attributed to the high energy cost of bending large lateral dimensions (~1-2μm) of the functionalized 2D sheets compared to the 200 nm length of the bullet-shaped VSV particles. An optimum lateral dimension of ~300 nm for functionalized 2D TRGO sheets was found to exhibit maximum viral interactions, inhibition efficiency, and signs of viral envelopment. Additionally, it was discovered that the triazine-based functionalization of TRGO did not disturb electronically the conjugated graphitic structure of 2D sheets. Contrary to previous beliefs, the conductivity of triazine-functionalized TRGO sheets was actually enhanced after functionalization. Furthermore, triazine could be used as a monomer to create 2D triazine structures on a gram scale in the presence of calcium ions. Unexpectedly, Raman spectroscopy revealed that the water content during the synthesis plays an important role in the crystallinity and carbon content of the synthesized structures. It was found that the crystallinity and carbon content of the 2DTS sheets were affected by the water content during the synthesis. Synthetic graphitic crystals were observed to form at low temperatures due to the presence of water, while a semi-crystalline 2DTS structure was formed during an anhydrous synthesis process. Potential applications of functionalized graphene include platforms or templates for developing new specialized antiviral therapies. For example, functionalized graphene could potentially be used to design targeted therapies that exploit the multivalent interactions between viruses and their cellular receptors. This could involve exploring the use of functionalized graphene as a delivery platform for antiviral drugs. Furthermore, in case of 2D triazine structures, electronics, optical and mechanical properties must be

explored in addition to the effect of functional groups on their surface properties and doping.

Keywords

Graphene, graphene oxide, thermally reduced graphene oxide, functionalization, hyperbranched polymers, 2D materials, active interface, atomic force microscopy, scanning probe microscopy, Raman spectroscopy, extracellular matrix, nanographene

Zusammenfassung

Die Aktivität von Materie kann einem System einzelner aktiver Komponenten mit kollektivem Verhaltenzugeschrieben werden. Dabei sind multivalente Wechselwirkungen typisch. Sie beruhen auf dem Zusammenwirken vieler individueller lokaler Bindungen, die zu multivalenten Bindungen und folglich zu emergentem Verhalten von Materie auf verschiedenen Längen- und Zeitskalen in der Natur führen. Das kontrollierte und präzise Hinzufügen von Multivalenz zu Nanomaterialien ist die Basis für einen bottom-up-Ansatz bei der Gestaltung von Form und damit verbundenen Funktionen. Daher sind das Verständnis der Struktur und die Kontrolle spezifischer Aktivitäten und Funktionalitäten dieser Nanomaterialien von großem Interesse und notwendig für die weitere Entwicklung von aktiven Materialien und Schnittstellen in verschiedenen biologischen und sensorischen Anwendungen.

Die Multivalenz von Nanomaterialien begründet ihre Nützlichkeit bei der biologischen Nachahmung und Anwendungen von viralen Hemmungen. Nur eine präzise Kontrolle und das Verständnis ihrer multivalenten Wechselwirkungen ermöglichen deren hohe Effizienz. Die große Oberfläche zweidimensionaler multivalenter Plattformen reduziert die insgesamt erforderliche Konzentration für effiziente Bindungen mit dem interessierenden Material. Zweidimensionale kohlenstoffbasierte Nanoschichten wie Graphen und Graphenoxid sind gute Kandidaten für multivalente Plattformen hoher Effizienz, aber eine kontrollierte und präzise Multivalenz hinzuzufügen ist schwierig. Graphenoxid enthält viele chemische funktionelle Gruppen, die in Bezug auf Typ, Anzahl und Position innerhalb seiner Struktur zufällig verteilt sind. Die biologischen Wechselwirkungen dieser chemischen funktionellen Gruppen sind jedoch unspezifisch, was zu nicht reproduzierbaren und komplexen Wechselwirkungen für Graphenoxid führt. Darüber hinaus beeinflussen weitere chemische Modifikationen der 2D-Graphen-Nanoschichten ihre elektronischen Eigenschaften und können ihren Anwendungsbereich in Sensoren und aktiven Schnittstellen einschränken. Das Ziel der vorliegenden Arbeit besteht in dem Verständnis, wie neuartige multivalente Funktionalisierungsmethoden die zwei-dimensionalen kohlenstoffbasierten Graphenschichten hinsichtlich ihrer Geometrie, ihrer spezifischen physikalischen Wechselwirkungen sowie ihrer elektronischen Eigenschaften beeinflussen. Damit sollte es möglich werden, das Bottom-up-Design von 2D-Nanomaterialien wesentlich zu verbessern.

Das konkrete Ziel dieser Arbeit ist die Untersuchung von zwei neuartigen Methoden zur Modifizierung von 2D-Graphen-Nanoschichten durch die Techniken "Graft to" und "Graft from", welche [2+1]-Nitren-Cycloadditionsreaktionen bei Umgebungsbedingungen und ringöffnende mehrfach verzweigende Polymerisation von Glycerin beinhalten. Diese modifizierten Nanoschichten wurden dann mittels Rasterkraftmikroskopie auf ihre Wechselwirkung mit viralen Partikeln wie Vesicular Stomatitis Virus (VSV) untersucht. Die Ergebnisse zeigen, dass nur sulfatierte post-funktionalisierte 2D-TRGO-Sheets in der Lage waren, stark an VSV und andere umhüllte virale Partikel zu binden. Die Ergebnisse deuten auch darauf hin, dass die 2D-multivalente Bindung von funktionalisierten TRGO-Sheets mit viralen Hüllen hauptsächlich auf unspezifischen elektrostatischen Wechselwirkungen beruht, ähnlich wie die extrazelluläre Matrix einer Zelle. Eine weitere Spezialisierung dieser Wechselwirkungen ist jedoch durch Variation von post-funktionalisierten Molekülen möglich. Insgesamt wirft diese Studie ein Licht auf das Potenzial funktionalisierter Graphen-Nanoschichten in verschiedenen Anwendungen, insbesondere im Bereich der Virologie, und liefert wertvolle Erkenntnisse für zukünftige Forschung.

Die Rasterkraftmikroskopie zeigte überraschenderweise, dass zwar funktionalisierte 2D-TRGO an VSV-Partikel binden konnten und flexibel genug waren, um sich auf einer flachen Glimmeroberfläche zu kräuseln, jedoch nicht in der Lage waren, virale Hüllen vollständig zu umschließen. Dies lag an dem hohen energetischen Preis für das Biegen der funktionalisierten 2D-Schichten mit großen lateralen Abmessungen (~1-2µm) im Vergleich zu den 200 nm langen, kugelförmigen VSV-Partikeln. Es wurde eine optimale laterale Abmessung von ~300 nm für funktionalisierte 2D-TRGO-Schichten gefunden, um maximale virale Interaktionen, Hemmungseffizienz und Anzeichen für virale Einkapselung zu zeigen. Zusätzlich wurde entdeckt, dass die Triazin-basierte Funktionalisierung von TRGO die konjugierte graphitische Struktur der 2D-Schichten nicht elektronisch stört. Im Gegensatz zu früheren Annahmen wurde die Leitfähigkeit von Triazin-funktionalisierten TRGO-Schichten tatsächlich nach der Funktionalisierung erhöht. Darüber hinaus kann Triazin als Monomer zur Herstellung von 2D-Triazin-Strukturen im Gramm-Maßstab in Gegenwart von Calciumionen verwendet werden. Unerwarteterweise zeigte die Raman-Spektroskopie, dass der Wassergehalt während der Synthese eine wichtige Rolle bei der Kristallinität und dem Kohlenstoffgehalt der synthetisierten Strukturen spielt. Es wurde festgestellt, dass die Kristallinität und der

Kohlenstoffgehalt der 2DTS-Schichten vom Wassergehalt während des Syntheseprozesses abhängig waren. Synthetische graphitische Kristalle bildeten sich bei niedrigen Temperaturen in feuchter Umgebung, während in einem Wasser-freien Syntheseprozess eine teilkristalline 2DTS-Struktur gebildet wurde. Potenzielle Anwendungen von funktionalisiertem Graphen umfassen Plattformen oder Vorlagen zur Entwicklung neuer spezieller antiviraler Therapien. Zum Beispiel könnte funktionalisiertes Graphen potenziell zur Entwicklung zielgerichteter Therapien eingesetzt werden, die die multivalenten Wechselwirkungen zwischen Viren und ihren zellulären Rezeptoren ausnutzen. Dies könnte die Erforschung der Verwendung von funktionalisiertem Graphen als Übertragungsplattform für antivirale Medikamente umfassen. Darüber hinaus müssen bei 2D-Triazin-Strukturen neben dem Effekt funktionaler Gruppen auf ihre Oberflächeneigenschaften und Dotierung auch elektronische, optische und mechanische Eigenschaften erforscht werden.

Schlüsselwörter

Graphen, Graphenoxid, thermisch reduziertes Graphenoxid, Funktionalisierung, hyperverzweigte Polymere, 2D-Materialien, aktive Schnittstelle, Rasterkraftmikroskopie, Rastersondenmikroskopie, Raman-Spektroskopie, extrazelluläre Matrix, Nanographen

Chapter 1

1. Introduction

1.1. Motivation

Viral diseases such as Influenza, Herpes, SARS-COVID-19 and HIV are of the most common viral infections that humanity is facing every day. Dealing with such viral diseases cannot be ignored and its highly necessary to be ready with new tools for the future pandemics and new mutations of such viral infections. Prevention, Diagnosis, and Treatment are all needed as a preparation plan for pandemics, but advancement from prevention to treatment preparedness always takes time, cost, and results in life loss due to the time needed. Therefore, humanity requires viral inhibitors that can possibly play an efficient role in the main three segments of preparedness (Prevention, Diagnosis and Treatment) to deal with viral infections. Such infection inhibitors work based on prevention of the interaction with cells both mechanistically and chemically.

Viral particles interact with cell membrane through a process of "Multivalent interaction" that is, a strong interaction between viral particle and cell as a consequence many weaker interactions between the ligands and receptors present on viral particle and cell membrane, respectively. Previously, Vonnemann *et al*.[1] demonstrated that Gold nanoparticles with Polysulfated multivalent groups are capable of interaction and inhibition of the viral particles. However, two main problems were encountered. Firstly, the high concentration of Gold nanoparticles was needed for a successful inhibition of viral particles from entry into the cells. And secondly, gold nanoparticles had limited contact area with the viral particles due to their, size, geometry and rigidity. Therefore, in this research I focused on overcoming those shortcomings by investigating a two dimensional and flexible interface utilized for multivalent interactions for viral inhibition final goal.

Since the experimental isolation of graphene by Geim et al. [2,3], physicists and organic chemists have extensively investigated its physical and chemical properties, resulting in thousands of scientific articles within their communities. Indeed, the geometrical state of graphene as a two-dimensional and atomically thin material has been a motivator behind many experimental and theoretical investigations regarding its mechanical strength and flexibility [4–8]. Due to the difficulty in achieving single-layer and uncontaminated graphene with large surface areas, physicists and chemists have

been forced to work with graphene variants that are also capable of undergoing physicochemical modifications. Materials such as graphene oxide (GO) and thermally reduced graphene oxides (TRGO) are capable of numerous modifications. Many new applications of graphene, including the research within this thesis, are being realized using GO and TRGO.

The large surface area of graphene and its oxidized version, GO, makes them very interesting for biomedical interactions and sensors [9–14]. Additionally, utilizing the mechanical flexibility of graphene and its variants to maximize their surface area of interaction for interfacial activities is an intriguing way of creating active nanomaterials at interfaces. For example, sulfated gold nanoparticles as multivalent heparan mimic interfaces have been successful in inhibiting viruses [1]. Inspired by those functionalized gold nanoparticles, two-dimensional polysulfated TRGO sheets as multivalent and flexible structures for viral inhibition were conceived. Previously, attention has been given to the thickness [15], lateral size [11], and structure [16,17] of carbon-based 2D materials and their antiviral capabilities. However, there has been a lack of attention to modification and control of individual 2D sheet interfaces and their precise vertical functionalization (vertical to the plane of the 2D sheet). Thus, parameters such as the controllability of functional groups and control of selective targeting for such 2D functional interfaces need further research.

The two aforementioned parameters must be researched for the novel methods of functionalization of the 2D carbon-based sheets, i.e., TRGO and graphene, for [2+1] nitrene cycloaddition and "Graft from" strategies. In the first part of my research, I aim to investigate and demonstrate the step-by-step post-functionalization of TRGO through these two mentioned methods and investigate their potential for interfacial interactions with model viral envelopes, such as Vesicular stomatitis virus and Human/Animal Herpesvirus.

Additionally, the lateral direction of stepwise multivalent addition "2D polymerization" based on [2+1] nitrene cycloaddition could be a controllable, low-cost, and environmentally friendly process for creating future semiconductors. To determine if lateral 2D growth is possible, in the second part of this research, I aim to investigate the 2D Triazine structures and their crystallinity using Scanning Probe Microscopy and Raman Spectroscopy. Furthermore, water, as a commonly found solvent in our environment, could have immense effects on the nanomaterials, specifically on the

growth of 2D structures and their crystallinity. Therefore, investigating the effects of solvents on the structure of Triazine 2D polymerization, Graphite oxide, and the production of the nanographenes, as well as Raman spectra of graphene, are critical and informative for assessing the material state quantitatively and qualitatively.

1.2. Outline of Thesis

In **Chapter 2**, I will present the scientific fundamentals related to my research. A brief overview of multivalent interactions and materials, along with their novelty, will be described. Furthermore, I will outline the components of the multivalent functionalized graphene system, specifically the base nanostructures such as graphene oxide (GO) and thermally reduced graphene oxide (TRGO), in addition to discussing the known properties of multivalent functionalization strategies, both 'Graft to' and 'Graft from.' Additionally, Muscovite mica and highly oriented pyrolytic graphite, common substrates for most experiments, will be described. Subsequently, I'll fundamentally describe hyperbranched polymer structures based on polyglycerols. The final segment of Chapter 2 will explain scanning probe microscopy, scanning force microscopy with its quantitative nanomechanical methodology, and PeakForce TUNA mode, complemented by the fundamentals of Raman spectroscopy and mapping. These analytical tools were extensively used in this research and its conclusions.

Chapter 3 will describe the analytical techniques, methods, and experimental preparations employed in my research. This includes the preparation of 2D carbon-based nanosheets at various interfaces, both with and without viral model mixtures. It will cover scanning force microscopy sample preparations and calibration methodologies, quantitative nanomechanical mapping, PeakForce TUNA custom-made sample preparations, and experimental descriptions, in addition to notes on Raman spectroscopy experiments.

In **Chapter 4**, I will present the main findings and results of my research, including datasets acquired using scanning force microscopy in quantitative nanomechanical mapping and Raman spectroscopy and mapping. The section 4.1.1 and 4.1.2 will focus on the results of the stepwise Triazine-based functionalization and the potential interaction activity between the functionalized TRGO and viral envelopes.

Section 4.1.3 will describe the characteristics of 'Graft from' functionalized TRGO nanosheets, lateral dimension statistical observations, and their combination with viral particles. Section 4.2.1 will demonstrate the scanning force microscopy results of electronic characterization via PeakForce TUNA methodology and Raman spectroscopy of the 'Graft to' novel functionalization method for 2D carbon-based nanosheets. Lastly, in section 4.2.2, the scanning force microscopy topography and Raman spectroscopy of the metal assisted 2D Triazine structures will be demonstrated.

Chapter 5 will delve deeper into discussing the findings demonstrated in Chapter 4, emphasizing their importance and relevance to the current and future design and applications of functional 2D carbon-based structures. It will primarily discuss the covalent functionalization of thermally reduced graphene oxides (TRGO) in two main forms: via a multistep [2+1] nitrene cycloaddition functionalization process 'Graft to' or through an in situ ring opening polymerization of polyglycerol hyperbranched in 'Graft from' methodology utilizing the oxygen-containing sites of TRGO. Using SFM-Quantitative nanomechanical mapping data, I will model the topography and extent of successful functionalization of multivalent functionalized graphene nanostructures. Additionally, in collaboration with Dr. Daniel Lauster, the viral inhibition capacity of their interaction with vesicular stomatitis viruses in vitro will be demonstrated. In section 5.3. I expand on that collaborative research by demonstrating the importance of the size variations of active graphene multivalent sheets on the viral inhibition of human and animal herpesviruses. The results of my experimental work introduce chemists and physicists to the topography and characteristics of the latest variations of active nanomaterials, combining the structural functionality of a hyperbranched polymer and a highly flexible 2D atomically thin carbon sheet—a 2D multivalent hybrid platform. Moreover, these study results find applicability in surface modifications mimicking the extracellular matrix of cells, viral filtration devices, and will provide information necessary for designing robust counter methods to deal with future pandemics, as suggested by some external publications.

Furthermore, in the last part (section 5.4), I will discuss the 'Graft to' [2+1] nitrene cycloaddition functionalization of TRGO not only as a successful method of functionalization but also as a nondestructive process to the electronic structure of the

Nanographene sheets, as suggested by scanning force microscopy in PeakForce-TUNA mode and Raman spectroscopy of functionalized Nanographene structures. Results show a conductivity enhancement in Nanographene after covalent [2+1] nitrene cycloaddition reactions, contrary to the expected reduction of electron mobility due to covalent modification and disruption of the conjugated system of graphene. This implies that the π-conjugated system is rather preserved in a 'Graft to' functionalization method, and an n-type doping could be responsible for the conductivity enhancement of nanographenes functionalized by Triazine.

Regarding the Triazine carbon and nitrogen-based structure, I will describe the last segment of my research in Chapter 5. I will present the results of scanning force microscopy and Raman spectroscopy investigations of the Triazine-based covalent structures synthesized under the supervision of Prof. Rainer Haag and Dr. Abbas Faghani. The results indicate that the covalent synthesis of the Triazine-based structures is not only mediated by water as a solvent but also that the water content during the synthesis process defines the long-range crystallinity of those nanostructures. Using scanning force microscopy, I observed that the synthesized Triazine structures are indeed two-dimensional and layered in their topography. However, using Raman spectroscopy, I found that the fine line between the synthesis resulting in the production of synthetic Graphite versus Triazine structure is the water content during the synthesis process. This information would provide chemists and physicists with a better understanding of the Triazine-based structures and possible synthesis directions based on the water content of the environment.

In Chapter 6, I summarize the essence of this thesis and propose the prospects of my work based on the current findings.

Chapter 2

2. Fundamentals

This chapter describes the basic concepts, theoretical fundamentals, and the most important experimental results reported in the literature, which are the basis of this thesis. These include:

1) A general view of the field of Multivalent interactions and its main key concepts.

2) The chemical, physical, and topographical information on the two-dimensional carbon-based sheets and membranes.

3) Graphene folding and its flexibility as the background for maximization of viral inhibition through bending of 2D functionalized sheets and further, the hyperbranched polyglycerols as the main and most important post functionalization molecules in this research.

Moreover, the technique of scanning force microscopy and its relevant modes to this thesis, in addition to Raman spectroscopy, are discussed, including their theoretical principles, instrumentation, and application to a multivalent functionalized 2D material Carbon Triazine crystalline and polycrystalline structures.

2.1. Multivalent Interactions

Nature often utilizes the most efficient ways of creating harmony and interactions. This principle is often observed in reversible strong interactions between biological matters. Independent of scale of matter the multivalent interactions result in strong cohesion between surfaces and prevent the shearing between those interfaces. Making multivalency a ubiquitous phenomenon of nature involving complex binding of matter non-covalently between m-valent ligands and n-valent matching receptors where m & n are always more than 1 and $m \neq n$. An example of large-scale manmade multivalency is the Velcro materials. Entanglements of hooks of a surface with the loops of the opposing surface result in many similar weak bindings resulting in simultaneous strong locking.

At the molecular and nanoparticle scale, multivalent interactions are readily observable. Molecular components, such as ligands and receptors, exemplify this concept by facilitating self-organization, adhesion, and signal recognition in numerous

biological processes[18–20]. For instance, within biological systems, the multivalent interactions of multiple ligands and receptors at cell membrane and virus interfaces play a crucial role in viral interaction, cellular uptake, and subsequent viral infections. Nature demonstrates the ability to modulate the efficiency of biological interactions by varying parameters such as size, geometry, density, and types of ligand/receptor pairs (e.g., viral particle evolution).

In proteins, proper folding is essential for functionality[21]. Stabilization of the protein's folded structure relies on multivalent interactions among multiple hydrophobic amino acids[22]. The reversibility of multivalent interactions is another crucial factor contributing to their advantages over monovalent interactions. Given that multivalent interactions are often based on numerous weaker individual interactions, they can exist in a dynamic state of binding and unbinding, resulting in a multi-stable configuration.

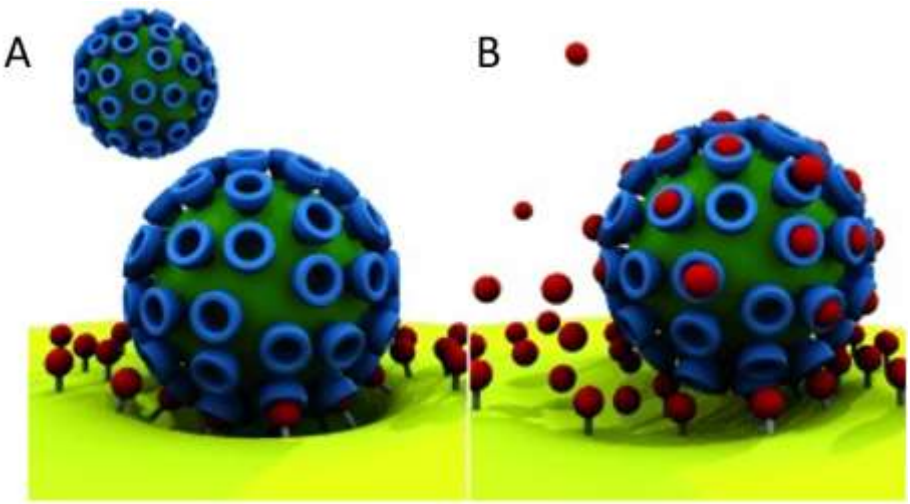

Figure 2.1, A multivalent interaction of the viral particles with the cell extracellular matrix. *A) without any inhibitor B) monovalent interaction of inhibitor particles, requires high concentrations to successfully occupy the viral particle receptors. Adapted from reference* [23].

2.2. Viral Inhibition

Viral infections are often significant threats to life on Earth, recent outbreaks of diseases like, SARS-CoV-19 (COVID-19), Influenza H1N1, human immunodeficiency virus (HIV), and various others [24–26], Requires addressing them and preparing for later potential epidemics and pandemics. This preparation involves three key steps: 1) Prevention, 2) Diagnosis, and 3) Treatment. Each of these steps requires the

development and establishment of methodologies before widespread application. Starting from prevention to treatment, the time and cost of research and development increases. A versatile approach applicable across all three steps involves the development and utilization of new "viral inhibitory" materials. Viral inhibition is a preventive process that aims to block viral particle entry into cell membranes, primarily using nanomaterials at the scale of the viral particle to interfere with multivalent receptors on the viral particle's outer membrane.

2.2.1. Viral inhibition quantification and measurement

Viral inhibition measurements and quantifications are scientific experimental processes typically conducted by virologists and biologists. However, various microscopy methods allow access to the scale of viral particle observations, making it possible for specific sets of microscopy methods to observe viral interactions with materials of interest and investigate the viral inhibition process. The inhibition process may involve all or parts of the following processes, depending on the design and functionalities of the inhibitory nanomaterials or interfaces used: [27,28] 1) interaction between the viral particle and inhibitory material, 2) competition between viruses in binding with host cells, 3) inactivating virus particles before entry into live cells, and 4) creation and release of reactive oxygen species. [29]

Viral inhibition can be quantified experimentally through various methods, specifically: 1) Virus capture assays, 2) Cell viability assays, and 3) measuring the infection quantity of healthy, live cells when incubated with viral inhibition nanomaterials compared to a reference. In this context, the emphasis is on methods suitable for investigating viral inhibition by 2D carbon-based nanomaterials.

Virus capture assays employing nanoparticles are designed to investigate interactions between viral particles and host cells [30]. In these assays, a combination of the nanomaterial and a specific concentration of viral particles is prepared in a suitable buffer solution, such as phosphate buffer solution (PBS). This combination is then allowed to incubate for a specified duration known as the incubation time. After incubation, the mixture is centrifuged to pellet and separate the nanomaterials and viral particles from the supernatant. The supernatant is subsequently titrated for infectious particles using an endpoint dilution assay called the “50% tissue culture infections dose” or (TCID50). This involves infecting cultured cells in multiple wells and counting

the infected vs. uninfected wells after a few days of incubation. Quantification of the number of infected vs. non-infected wells can be performed either manually or through automated means using microplate reading devices.

Cell viability assays provide another methodology for quantifying viral inhibition by materials. These assays focus on determining cell proliferation, cytotoxicity, and the number of healthy and viable cells in a culture after exposure to certain conditions, such as drugs, toxins, and chemicals.[31] In viability assays, it is crucial to quantify the number of living cells at the end of the experiment. This can be achieved using the tetrazolium (MTS) reagent to assess the metabolism or enzymatic activity of the living cells.[32] The incubation of the reagent with viable cells results in the conversion of a substrate to a colored or fluorescent product, which can be detected using automated microplate reading devices. Measurement of the fluorescence signal is critical for deducing the proportional number of viable cells since the fluorescence signal decreases with a reduction in the number of living cells.

2.3. Graphene and functionalized Graphene

Graphene, an allotrope of carbon, represents a single layer of graphite crystal consisting of a π-conjugated structure of carbon atoms. It forms a two-dimensional covalently bonded structure of carbon rings arranged in a hexagonal pattern (Figure 2.2). Initially predicted to exist theoretically, graphene was experimentally rediscovered in 2004[1]. Subsequently, in 2010, Geim and Novoselov were awarded the Nobel Prize in Physics for their groundbreaking experiments involving isolated graphene[33]. Extensive experimental investigations into graphene have revealed remarkable properties, including high electrical conductivity at room temperature[34], high thermal conductivity[35], optical transparency[36–38], as well as notable high flexibility (low bending stiffness) and a high Young's modulus[39].

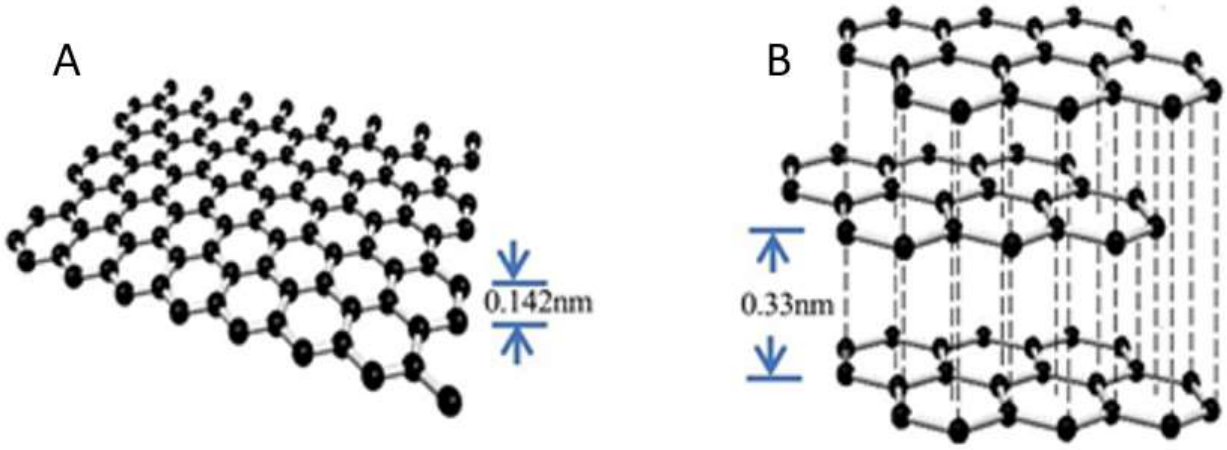

Figure 2.2, Schematic view of A) Graphene Vs B) Graphite. Adapted from reference [40].

Graphene has been proposed to be an ultra-barrier, that is an ultra-thin impermeable barrier to small molecules [41]. This ultra-barrier property has been considered to be due to the dense net like delocalized electron cloud that block the center of the aromatic ring structure with a repulsion field. [42]

A functionalized graphene is essentially an interface with expanded moieties for facilitation of certain requirements. Since covalent modification of graphene is essential for its stable functionalization, the conjugated structure modification cannot be avoided which often leads to disruptions of the basal plane of graphene and its electronic properties. These electronic properties that define the conductivity of the graphene can be affected by 1) hybridization state of carbon, 2) dipole interactions enhanced via quantum capacitance and 3) orbital hybridization with an interfering molecule. [42] often the chemical functionalization of graphene results in disruption of the sp^2 hybridization of carbon rings in graphene.

2.3.1. Graphene Folding

Graphene as a single layer of carbon atoms with in-plane covalent bonds is considered to be a self-avoiding structure that does not self-penetrate if it overlaps with another layer of graphene unlike the two-dimensional lipid membranes. Graphene single layer has been observed experimentally to undergo extreme bending resulting

in an overlap onto itself creating a bilayer graphene structure and curvature “a folded region” and yet remain stable in this conformation. The simulation studies have demonstrated that graphene can be modeled using finite deformation beam theory. [6,43] This further suggests that the graphene multilayers also may follow similar mechanical bending behavior similar to a stack of sheets of paper. Single-wall carbon nanotubes are in principle made by the stable longitudinal bending of the single-layer graphene sheets, similar to rolling of a sheet of paper. Graphene bending can be considered as highly necessary for the process of maximizing the multivalent interactions with nanoparticles of interest within this study. Since graphene differs from a classical sheet of paper due to its single-atom thickness, Lu Qiang et al [44] used a first-generation Brenner potential to calculate and drive the analytics of bending modulus for a single-layer graphene sheet, with a bending stiffness being found to be 0.133 nN nm. This value is a factor of 10 lower than the force required to rupture a typical covalent bonding. Therefore, a stable folding of graphene becomes possible that is further enhanced by the added stability of van der Waals adhesion interaction between the overlapping layers onto each other.

Graphene fold involves at least two flat regions and an arched segment in between. Flat regions will remain stable as long as there is enough area of interaction, and they keep interacting via the Van der Waals forces with an interlayer distance “d” equal to graphene thickness. The arched segment remains stable due to both the stability of adhered flat regions and the carbon bonding flexural hindrance.

Energy requirement for a stable graphene fold is described in the below (Equation 1) as the sum of Energy required for bending of a certain number of C-C bonds and Van der Waals energy of adhesion between the overlapping graphene layers after bending. Additionally, for graphene to be triggered to self-fold, 1) overlapping flat regions should have greater adhesion energy than the bending energy required for the arched segment. 2) A total energy is gained by bending graphene, and therefore self-folding is preferred configuration. Based on the described, the following formulation as shown in Equation 2, demonstrates that larger length of the overlapping region of graphene increases the adhesion energy and further stabilizes the folded graphene sheet.

$$E_{fold} = E_{bending} + E_{adhesion} \qquad \textit{Equation 1}$$

&

$$L_{fold} = 2(L_0 + L) \qquad \text{Equation 2}$$

where L0 and L represent the length of the flat region and the length of the half-arc region, respectively. Figure 2.3 demonstrates the experimental observation of graphene fold via Scanning Force Microscopy and schematics of the folded regions.

A process of folding can be initiated when there is a chance of gaining energy by doing so or due to an external shearing force enough to induce the bending. External energy required to bend the graphene structure could be provided by various sources such as; possible interfacial interactions, nano-manipulation or by physicochemical interactions between the graphene interface and other particles.

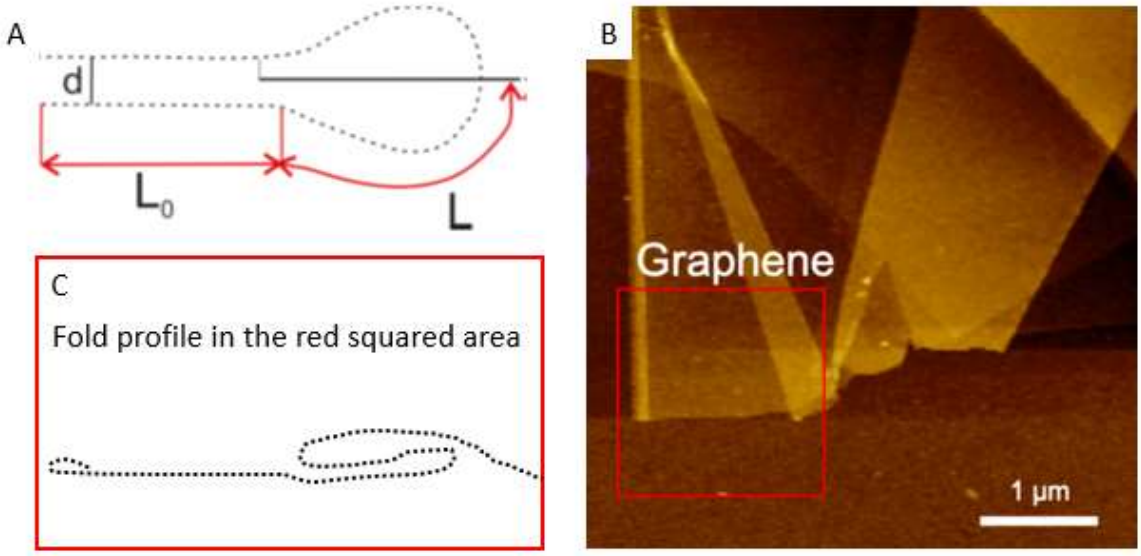

Figure 2.3, Graphene bending. A) Profile of a hairpin folded graphene sheet with its denoted regions, where d is the bilayer distance, L0 and L are the lengths of the flat and half arc (hairpin) regions, respectively. B) Scanning force microscope height image of the folded single l layer graphene deposited onto SiO2 layer of Si wafer. C) Schematic fold profile of the red square area in the (B). Image copyright by Mohammad Fardin Gholami. Adapted from reference [45].

2.3.2. Graphene electronic properties

Crystal structure of the graphene is based on a lattice consisting of two atoms of A and B per unit cell. These form a triangular structure with two sub-lattices of 'A' and 'B'. Carbon atoms are bonded to each other by the covalent σ-bonds with a length

of 1.42 Å. These covalent bonds are created by the sp^2 hybrid orbitals of those carbon atoms positioned neighboring to each other, creating a bond angle of 120º. A model describing the Graphene electronic band structure is known as the tight-binding model (TBM) [46]. This model considers that the in-plane σ-bonds are formed by three of the valence electrons, and the fourth valence electron occupies the 2pz orbital perpendicular to the graphene plane, forming π-orbitals with the neighboring 2pz orbitals[47]. It is further assumed that the contribution of the in-plane σ-bonds is negligible, and the electronic properties of the graphene can be described by the π-electrons. The band structure of the honeycomb hexagonal structure of the graphene is shown in Figure 2.4; as it can be seen, the valence band is formed by the π-states, and π* states form the conduction band. The conduction and valence bands of the hexagonal carbon ring touch at 6 neutral zones known as Dirac points, and due to the structural symmetry, one can consider the points K and K´ that are independent of each other. The touching of the valence and conduction bands in graphene at the Dirac points (point of vanishing density of states) [46,47] demonstrates the Zero Band gap semiconductor behavior of this 2D atomically thin material[48]. The Zero band gap state of the graphene is expected to be modified by means of strain or covalent modification of the in-plane σ-bonds within its hexagonal structure. Any disruption to the π system, namely conversion of sp^2 to sp^3 hybridization, would result in a variation of electron dispersion, lattice variation, and modification of band structures of graphene[42].

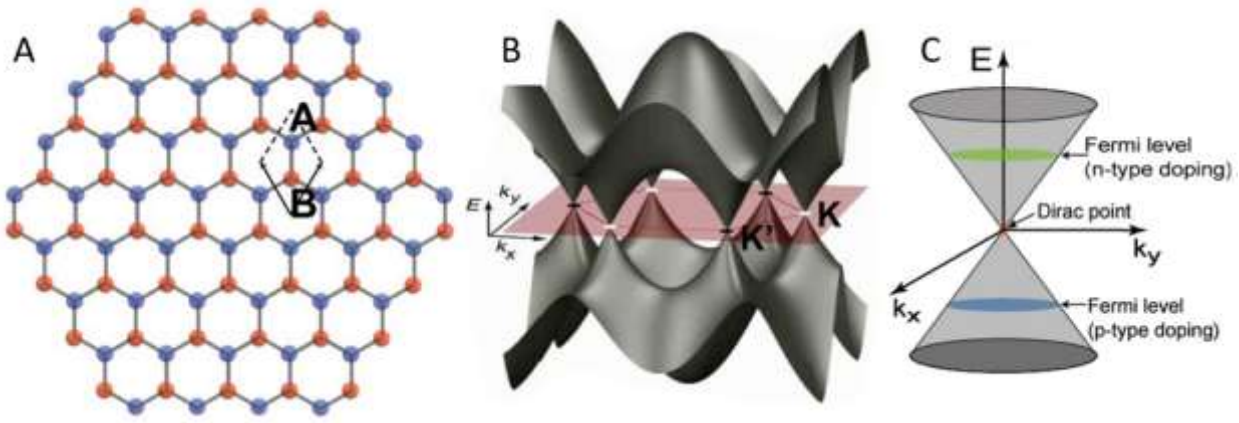

Figure 2.4, Graphene structure and Band structure. A) Graphene honeycomb hexagonal structure and positions of two atoms of the unit cell A and B. B) The 3D band structure of the graphene and positions of the K and K´ points. C) Dirac cone dispersion of states in graphene. Adapted from reference [48].

2.3.3. Graphene Oxide

Graphene oxide (GO) is a variation of graphene synthesized through the oxidation process of graphite crystals and later exfoliation of it to single layer sheets. The oxidation involves adding oxygen containing chemical functional groups such as -OH, -COOH, -O, -COO onto the basal plane of the graphite layers, creating Graphite oxide. These oxygen-containing functional groups are hydrophilic and capable of forming hydrogen bonds with water molecules. This hydrophilicity allows GO to stabilize within aqueous solutions. Several synthesis methods for graphene oxide have been developed[49]. The initial method, based on Hummer's oxidation method, also known as Hummers -Offerman oxidation, involves reacting Graphite crystals with oxidizing agents such as potassium hydroxide in the presence of concentrated H_2SO_4 acid[50].

Numerous models have been proposed for the basal plane structure of graphene oxide. However, most of these models remain ambiguous due to uncertainties regarding the distribution of functional groups across the structure and variations in graphene oxide samples across different studies. Graphene oxide can be considered as a berthollide (non-stoichiometric) compound[51,52] due to the oxidation process being influenced by point defects on the graphene sheets. The quantity and distribution of oxidizing groups depend on the random locations of these defects on the graphene sheets. Models proposed by Anton Lerf and Jacek Klinowski account for the non-stoichiometric nature of graphene oxide. Nevertheless, their models remain uncertain about the locations and presence of the (-COOH) functional groups at the edges of each GO sheet[53,54]. Figure 2.5 demonstrates the latest structural model of the single-layer Graphene oxide.

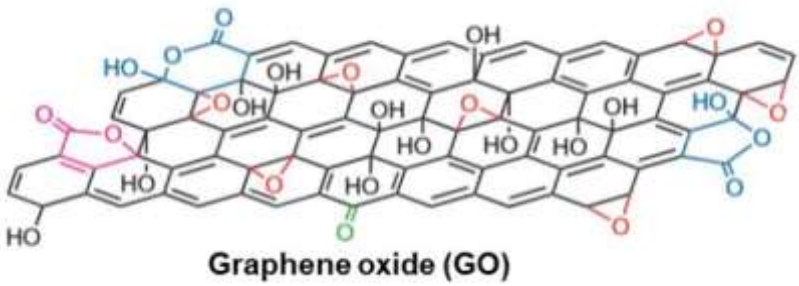

Figure 2.5, Latest structural model for graphene oxide. Only the structural connectivity is shown and steric orientations are not demonstrated. The blue colored groups demonstrate

the 5 and 6 membered lactol groups, epoxy groups are shown as red, ester of tertiary alcohol is shown as pink and hydroxyl groups as black, while green only shows the keton edge groups. Adopted from reference[55].

Graphene oxide contains both states of bonded carbon, namely sp^2 and sp^3. The ratio of the sp^2 and sp^3 is tunable with the help of reduction chemical reactions. Therefore, graphene oxide is transformable from an insulator into a poorly conductive material[56,57]. Using a scanning force microscope, it is possible to measure the thickness of a single-layer graphene oxide over a hydrophilic and atomically flat surface such as freshly cleaved mica. The GO thickness was measured to be in a range of ~0.7 nm to 1 nm[58–60]. The lateral dimensions of the graphene oxide sheets can range from 1 to 10 μm. Dimensions often depend on the duration of ultrasonication and oxidation reaction time. Ultrasonication can help the exfoliation of graphene oxide from graphite oxide stacks. Fast oxidization can lead to tearing of the graphene sheets at over-oxidized regions and non-uniform oxidization of graphene sheets. Very similar to graphene, self-folding of the graphene oxide has also been experimentally observed, as shown in Figure 2.6.

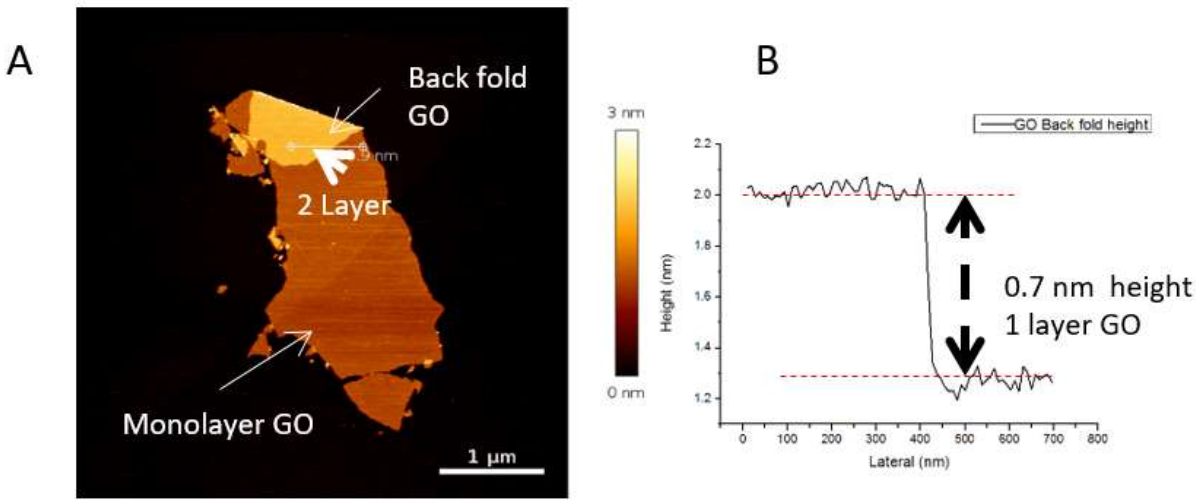

Figure 2.6, Graphene oxide bilayer thickness. A) Scanning force microscope height image of single layer graphene oxide deposited onto freshly cleaved muscovite mica. B) Step Height profile of the Graphene oxide stable back fold onto itself.

2.3.4. Thermally reduced Graphene Oxide

Graphene can be converted to thermally reduced graphene oxide (TRGO)[61,62]. This conversion is purely a synthetic process, and in the first step, graphite has to be oxidized into graphite oxide. The oxidation methods vary. However, Hummer's oxidation method has been vastly studied, leading to the insertion of oxygenated functionalities within the basal plane of graphene. This oxidation disrupts the basal plane continuity while increasing the solubility of the graphene in water.

Thermally reduced graphene oxide (Figure 2.7) is produced using at least two methods of thermal or chemical reductions. In the chemical process of reduction of oxygenated groups from the graphene basal plane, often hydrazine hydrate or borane tetrahydrofuran is used, which may not be environmentally friendly[63]. When graphite oxide is subjected to a thermal exfoliation process that increases its volume by 100 to 300 folds, with 80% of those graphene-based sheets being monolayers with an average lateral size of 500 nm and above[64]. The thermal reduction happens under a nitrogen atmosphere in a tube furnace at 400°C. Since in the thermal reduction process, enough energy is supplied to the GO at above 230°C, the usual functional groups present at GO basal plane are rapidly released. For example, the carbon dioxide, carbon monoxide, water, diols, carbonyls, and carboxyl's[64].

Furthermore, TRGO loses the oxygenated groups but does not recover its sp^2 hybridization since there still exist some remaining hydroxyl group functionalities. The hydroxyl groups then can be specifically targeted and modified through various methods for covalent binding of other molecules. In this research, thermally reduced graphene oxide was used without any more modifications by the organic chemists before further functionalization.

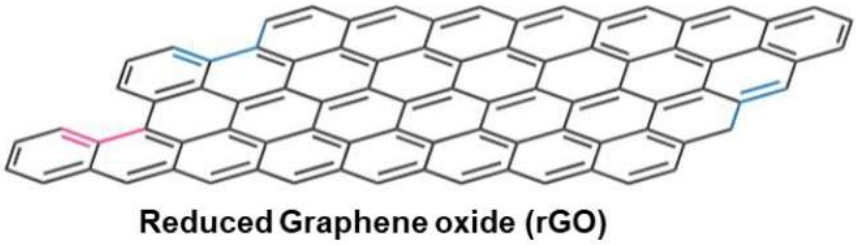

Figure 2.7, Structural model suggested for the Reduced graphene oxide and Thermally reduced graphene oxide. Adopted from reference [55].

2.4. Highly oriented pyrolytic Graphite (HOPG)

Highly Oriented Pyrolytic Graphite (HOPG) (Figure 2.8) is the IUPAC name for a synthetic graphite crystal that is highly crystalline in addition to that the graphene layers being highly aligned with each other. HOPG is mainly produced by heating a hydrocarbon source and allowing the crystallization of carbon layers under a tensile stressed substrate[65]. HOPG is a very interesting atomically flat substrate and source of experimental graphene layers. It is possible to exfoliate the HOPG mechanically using a tweezers to produce few layers or sometimes a single layer graphene on other atomically flat substrates such as Muscovite Mica. Freshly cleaved HOPG is used as a hydrophobic substrate in my research.

Using HOPG as a substrate requires understanding of its interactions with subject molecules. This is considered as the substrate adhesion and is largely dependent on the surface energy of the graphite or the graphene layer at interface of HOPG crystal. [66]

Furthermore, the process of adsorption of matter is a parameter dependent on the surface energy and is affected by the efficiency of a substrate in its role for microscopy procedures.

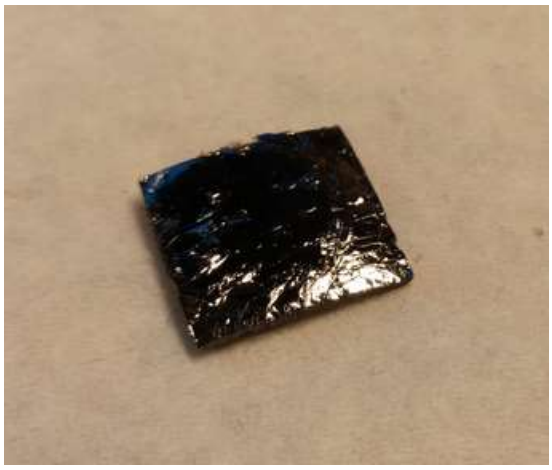

Figure 2.8, Highly oriented pyrolytic graphite block 1x1 cm.

2.5. Hyperbranched and dendritic polyglycerols

Dendritic and Hyperbranched polymers are a class of highly branched polymers where each branch is a linear chain that is well defined. The topography of the dendritic macromolecules often consists of random branch on branch structure (Figure 2.9), that resembles a tree. Many different synthesis routes and methods are available for production of dendritic and hyperbranched polymers[67]. However, the most precise synthesis methodology for hyperbranched and dendritic polyglycerols has been introduced by Haag *et al* and in similar time frame Sunder *et al* via Ring Opening multibranching polymerization (ROMP) process of glycidol.[68,69] The polydispersity index (PDI) is a sign of molecular weight variation in the synthesized polymer bulk and for ROMP process of glycidol is between 1.2 – 1.9 which is considered a narrow range for this polymerization method[70]. The chemical structure of the hyperbranched and dendritic polyglycerols (hPG & dPG) are shown in Figure 2.10, as it can be seen, hydrophilic hydroxyl (-OH) groups can be found within the structure making it a hydrophilic configuration soluble in water. Since the dimensions of hPG and dPG can be controlled precisely in addition to their functionalities[71] and rigid globular structure, they are emerging as drug carrier and anti-cancer delivery drugs, supramolecular encapsulators of guest molecules. [72]

The hydroxyl groups of a hyperbranched or dendritic polyglycerol can further undergo sulfation modification process. This process involves a change of the electrostatic interaction capability of the hPG or dPG interface.

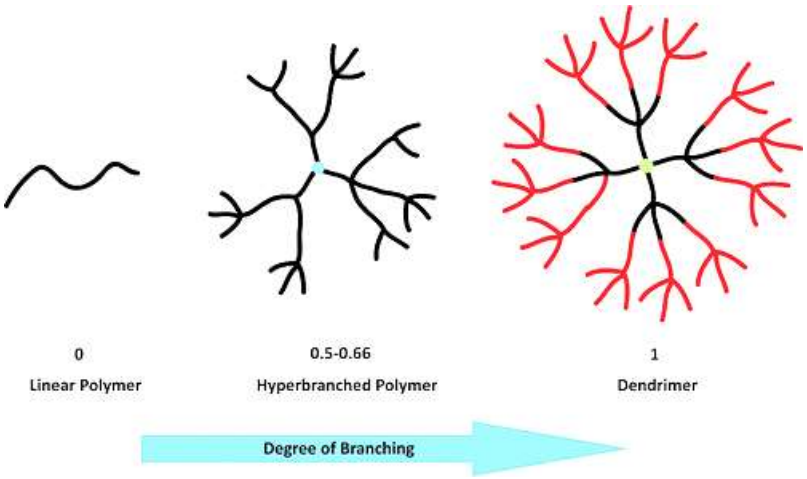

Figure 2.9, Illustration of various polymer architectures and their respective degrees of branching, DB. Adapted from Reference [70].

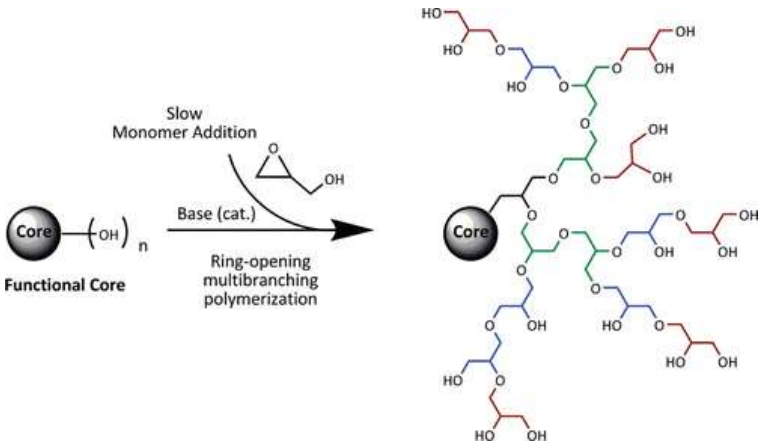

Figure 2.10, Synthesis of hyperbranched polyglycerols by ROMP process. Adapted from Reference [70].

2.6. Trichloro-triazine (triazine)

Also known as Cyanurchloride with IUPAC name of 2,4,6-Trichlor-1,3,5-triazine (triazine) is white solid powder. It is a very important molecule used within this study as it is a trimer of cyanogen chloride with 3 chlorine atoms that are replaceable under certain conditions at 0, 25 and 50 ºC temperature. Triazine is highly useful in basal plane functionalization of the 2D carbon-based structures used within this study, such molecule not only is capable of multivalent site creation within the 2D carbon-based structures but also is capable of further trimerization from its chlorine sites to possibly grow in two dimensions.

2.7. Herpesvirus

There are at least 120 types of various enveloped viruses within this family that are able to infect humans and other mammals.[73] Herpes simplex virus type-1 (HSV-1) (Figure 2.11) and equine herpesvirus type 1 (EHV-1) is both examples of family of Herpesvirus. The geometry of herpesviruses is often observed to be varying from spherical to pleomorphic, usually with envelope diameters ranging from 155 to 240 nm depending on the state of the virus. The viruses contain an icosahedral capsid with a diameter of approximately 125 nm.[74–76] it is known that this virus interacts with cell extracellular matrix through a charge interaction of the Glycoproteins B and C. [77,78]

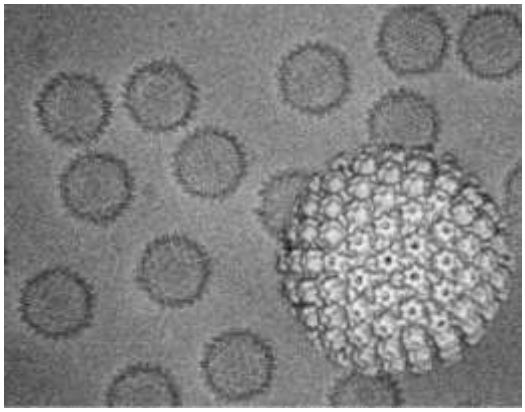

Figure 2.11, Background is a cryo-electron micrograph of herpes simplex virus (type 1) A-capsids, empty of DNA. Foreground shows a surface shaded representation of a 3D computer reconstruction obtained from 104 2D images. Adopted from reference [79]

2.8. Vesicular stomatitis Virus (VSV)

Vesicular stomatitis virus also known as VSV, is an enveloped virus particle that belongs to the family of *Rhabdoviridae* or rabies virus as the most famous species. VSV is known to interact with heparin mimic materials.[1,80,81] The structure of VSV is bullet shaped and is very distinct. Ge et al. accurately observed and modelled the bullet shape of VSV using Cryo- electron microscope.[80] VSV has application in therapeutic

and anti-cancer agents and vaccines as some of its strains are mom toxic to normal tissue.[82,83] There exist a lipid membrane that acts as the envelope to the structure of VSV. The envelope consists of G spikes of glycoproteins and encloses the RNA and other associated proteins. According to the Cryo-Electron microscopy imaging of the VSV (Figure 2.12), the bullet like structure has a dimension of 196 ± 8 for its length and 70 nm diameter. As it can be seen in Figure 2.12, VSV envelope may be damaged occasionally and the particles may be broken in half or 1/3rd smaller pieces.

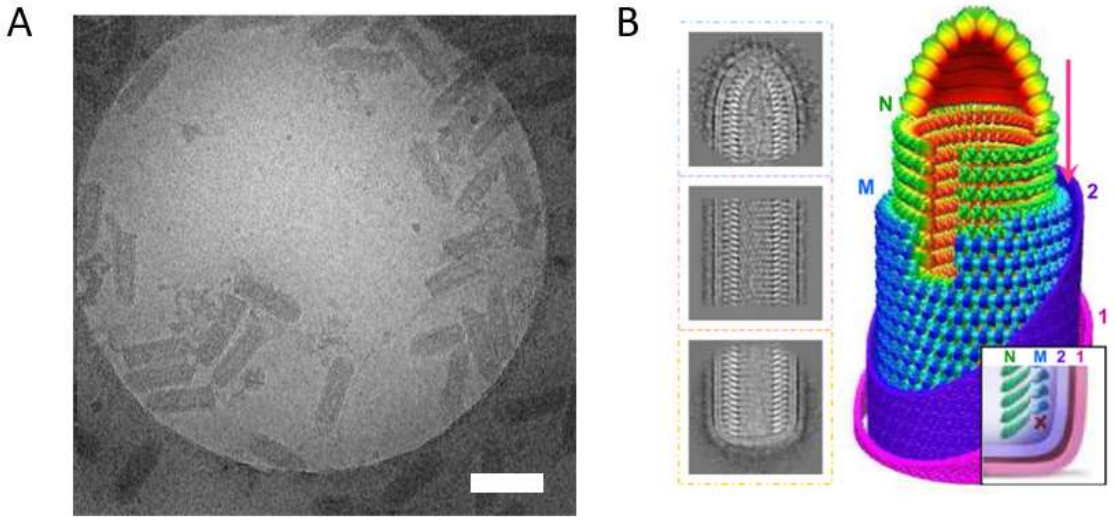

Figure 2.12, Cryo-TEM image of VSV, A) VSV as seen by Cryo-TEM, the scale bar corresponds to 200 nm. Adapted from Reference [32]. B) Representative 2D averages of conical tip, trunk and base of VSV and a montage model of the tip and the Cryo-TEM map of the trunk. N (nucleoprotein) is green, M (Matrix protein) is blue, and the inner ("2") and outer ("1") leaflets of the membrane are violet and pink. Inset: illustration of the base region of the VSV virion. The "X" marks the absence of a turn of M helix below the lowest turn of the N helix. "B" is Adapted from Reference [80]

2.9. Multivalent functionalization of TRGO

2.9.1. "Graft to" [2+1] nitrene cycloaddition reaction

The "Graft to" procedure or [2+1] cycloaddition reactions have proven to be highly potent in overcoming the drawbacks and inefficiencies associated with traditional covalent functionalization methods [84]. In these reactions, simultaneous bond formation and cleavage occur, making them easy to perform without the need for catalysts, all while preserving the π-conjugated structure of TRGO or graphene [85–87].

An essential aspect of [2+1] nitrene cycloaddition, employed in the investigated carbon-based 2D structures in this research, is its low defect content, as functionalization utilizes only the π-electron instead of dangling bonds in the basal plane (Figure 2.13).

In [2+1] cycloaddition, two expected approaches involve the formation of aziridine adducts and cyclopropane. Nitrene groups serve as intermediates, enabling the creation of aziridine adducts upon reaction with the π-conjugated structure of graphene or TRGO. Furthermore, cyclopropane is formed through carbine insertion reactions [87,88]. The main advantages of cycloaddition reactions include not requiring dangling bonds over the basal plane of 2D carbon-based sheets and forming strong covalent attachments. Additionally, the addition of azido ligands to the nanomaterial allows for the investigation of different ligand conformations on the activity of these 2D interfaces. The azido moiety is traceable using Fourier-transform infrared spectroscopy (FTIR) to monitor reaction conversion processes.

Thermal activation of azido moieties at easily accessible temperatures, such as 0, 25, and 160^{o}C, enables controlled post-functionalization density (Figure 2.14). This is exemplified in the synthesis of TRGO with triazine groups, post-functionalized by hyperbranched polyglycerols attached only to the secondary chlorine atom (TRGO-Trz-hPGlow) and another version with both secondary and tertiary chlorine atoms reacted to contain hyperbranched polyglycerols (TRGO-Trz-hPGhigh). It is important to note that in case of hyperbranched polyglycerols as the post functionalization macro molecules, the process of sulfation to create a mostly negatively charged surface charge is possible. This variation is known as TRGO-Trz-hPGS and can be created based on both the hPGlow and hPGhigh variants of TRGO-Trz-hPG.

Furthermore, the high reactivity of nitrene species in these reactions initiates a pericyclic [2+1] cycloaddition reaction within the graphene in-plane, forming an aziridine ring that may or may not affect the conjugated system of graphene. Further insights into this question are addressed in the results of this thesis in subsections 4.2.1 and 5.4.

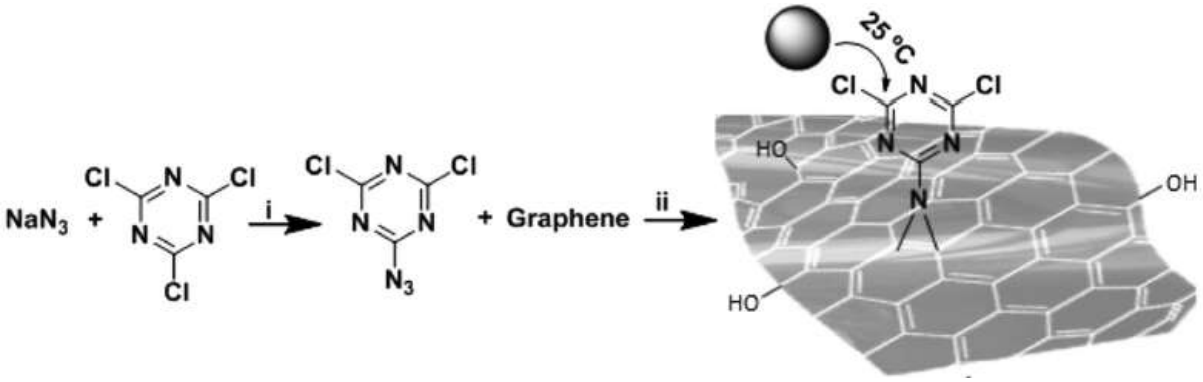

Figure 2.13, Functionalization of graphene by [2+1] nitrene cycloaddition using 2-azido,4,6-dichloro-1,3,5-triazine as nitrene precursor. Reaction conditions; i)N-methyl-2-pyrrolidon, 0 °C, 1 h and ii)Sonication, stirring, room temperature 70 °C, 24 h. Adapted from reference [32]

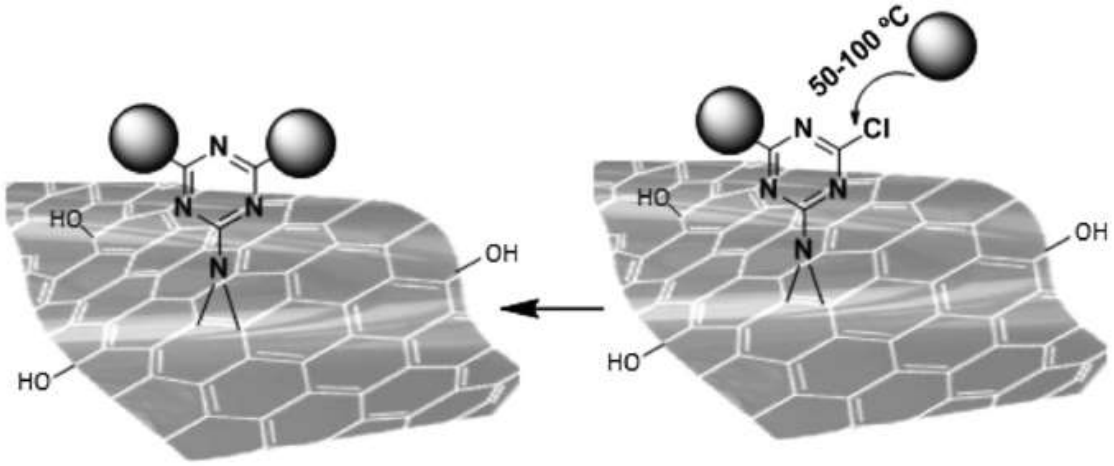

Figure 2.14, Stepwise nucleophilic substitution of chlorine atoms of Triazine groups at different temperatures resulted in controlled post-functionalization of TRGO-Trz. [32]

2.9.2. “Graft from” ring-opening multibranching polymerization

Previously, Schwartz et al. [89] introduced an approach based on surface initiated ring opening multibranching polymerization (ROMP) for direct synthesis of specific scaffold materials. This methodology has been shown to be applicable at the nanomaterial scale.[90] However, to achieve the access to this chemical modification in case of 2D carbon-based nanomaterials like Graphene, oxidation and a subsequently a thermal reduction of those groups are still necessary.

As mentioned previously, thermal reduction process results in exfoliation and remains of some hydroxyl groups within basal plane of 2D sheets. Polyglycerols then could graft onto the basal plane by utilization of those hydroxyl groups using ROMP.

This methodology has been tried for fullerenes and has been demonstrated by Adeli et al. to work. [91]

Thermally activated ROMP requires the monomer in large quantity and a weak nucleophile like hydroxyl groups that are already present within TRGO basal plane (Figure 2.15). At the right temperature, 120 °C the hydroxyl groups are able to interact with the monomer here glycidol. During this process an epoxide ring is opened and polymerized. The ending of the polymerization process is then controlled using lowering temperature or quenching [92]. Furthermore, a Polysulfation process is required to introduce the ability for potential electrostatic interactions of the now “Graft from” functionalized TRGO sheets as active surfaces. Alban et al.[93] worked extensively on the sulfation process in which specific amount of the hydroxyl groups of polyglycerols could be converted into sulfated groups with negative charge at their interface.

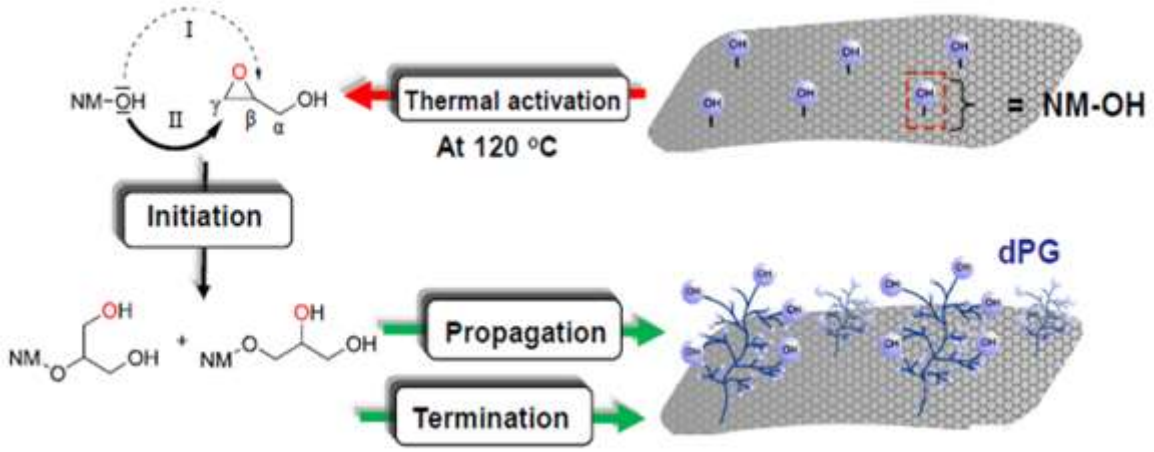

Figure 2.15, Schematic demonstrating the route in synthesis and interfacial modification of TRGO using "Graft from" methodology.

2.10. Triazine as monomer for 2D growth

Based on the topological understanding within polymer science, the linkage of the monomers can take place in various dimensions. One dimensional growth that is the most common process of polymerization, often results in growth of polymer single chains that may or may not entangle to from globular structures. A three - dimensional growth is often observed in the process of polymerization and cross linkage, such as seen in diamonds, that is a sp^3 hybridized carbon atoms in 3D and vulcanization of rubber. Indeed, a two - dimensional polymer also can exist, that is as long as the

monomer contain an n+1 number of binding sites, an n-dimensional polymerization process is possible.

In my collaborative research work, cyanuric chloride (or Triazine) were used as a monomer for 2D polymer synthesis and [2+1] cycloaddition reactions. Cyanuric chloride has three highly reactive chlorine atoms that could be utilized due to its thermally active chemical selectivity for reaction with nucleophiles. Therefore, by manipulation of temperatures in triazine chemistry, synthesis of a mono-, di-, and tri-substituted cyanuric chloride/ triazine derivatives became possible. Monosubstitution of chlorine can occur below or at 0 °C, the di-substitution occur at 25 °C, and the third chlorine could be replaced at temperatures above 60 °C (75 °C), which then creates tri-substituted triazine derivatives (Figure 2.16) in a one-pot reaction.

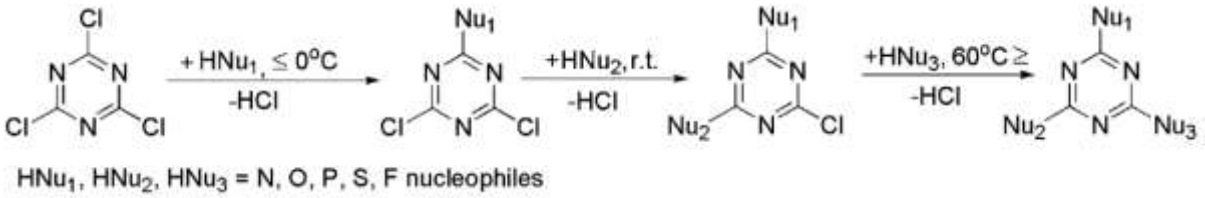

Figure 2.16, Schematic of step-wise substitution of 2,4,6-Trichloro-1,3,5-triazine(CC) by manipulating the temperature. Adapted from reference [94].

2.11. Muscovite Mica

Muscovite mica, also known commonly as mica, is a naturally occurring inorganic monoclinic mineral crystal with a chemical composition of KAl_2 (Si_3Al) O_{10} $(OH)_2$ (Figure 2.17). Muscovite Mica was named based on the location of its first application, based on Muscovy Glass, Mica was used as glass substitute in Russia. Water content in the structure of mica depends on the location of its formation. Mica ranges from optically transparent to translucent depending on its thickness. It is a suitable workbench for many atomically sensitive physical measurements such as scanning force microscopy. This is because of its perfect layer by layer cleavage at [001] crystal planes. Perfectly cleaved layers provide atomically flat surfaces which are

very useful in height and other quantitative measurements done by Scanning force microscopy.[95]

Additionally, Mica with just a few micrometers of thickness is transparent to visible range of wavelengths that make it a suitable candidate as substrate for carbon-based materials graphene with at least ~ 10% visible light absorption[38] and further Raman spectroscopy. In this work, I use mica as transparent substrate for Graphene, Graphene Oxide and 2D Triazine covalent structures. The highly ordered crystalline structure of mica makes it a very good barrier to small molecules such as water and oxygen[41] and due to its hydrophilicity water molecules and hydrophilic structures tend to adsorb onto it without need of further modifications[95].

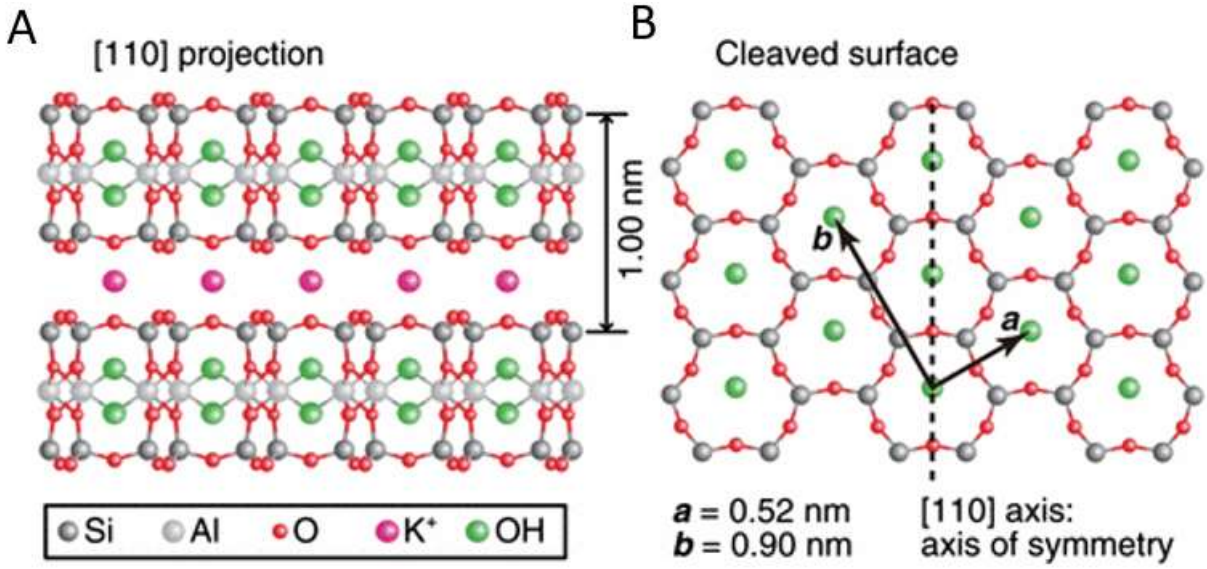

Figure 2.17, Mica crystal structure, Potassium atom is always present at the surface when mica is cleaved. Adapted from Reference [96].

The covalent bonding between the silica, aluminum and hydroxide present in the crystal structure is much stronger than the weak bonding with the potassium molecules present between each layer.

Scanning force microscopy height image of the freshly cleaved mica is then shown in (Figure 2.18). As it can be seen in the figure, Mica is seen as an atomically flat surface with minimal features, that is the standard deviation of variation of the mica flat atomically surface as measured by scanning force microscope in tapping mode is just 26 picometers that is mainly the instrumental noise. Furthermore, Raman spectroscopy of the freshly cleaved mica surface is shown in the Figure 2.19. When mica is exposed to laser wavelengths 532, 638 and 784 nm, it demonstrates a few

vibrational peaks in the range of 265 to 1115 cm^{-1} with highest intensity of frequency at 699-702 cm^{-1} depending on instrumental calibration and grating used. Mica Raman spectra is featureless between 1115 to 2800 cm^{-1}.

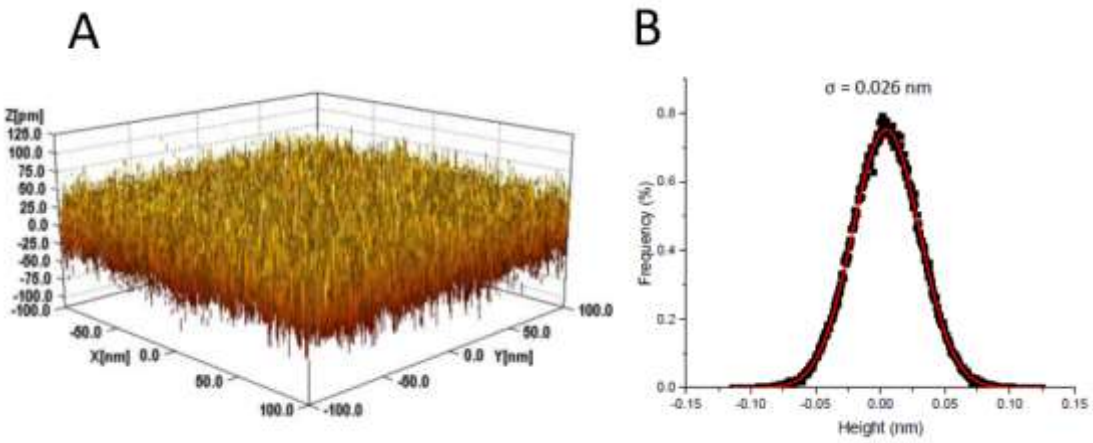

Figure 2.18, Tapping Mode-SFM roughness analysis of the mica surface a, 3D view of the height variations over freshly cleaved mica. b, Histogram of the height data extracted from image (a). Sigma shows the RMS surface roughness to be ~ 0.026 nm. Adapted from Reference [97].

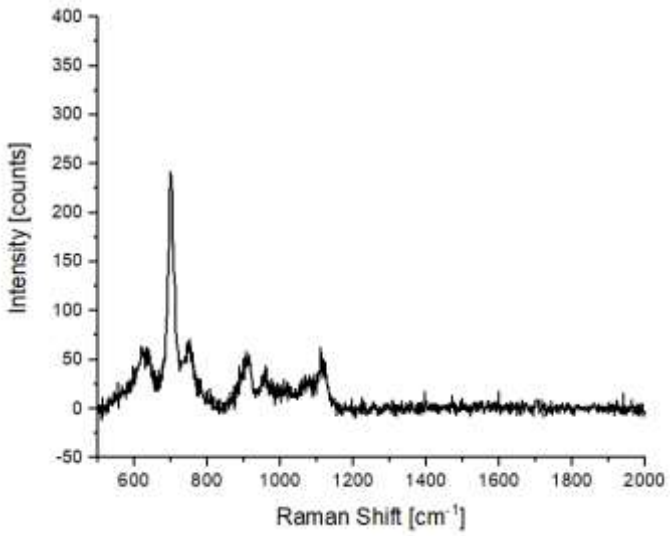

Figure 2.19, Raman spectrum of freshly cleaved muscovite mica at ambient conditions 35-45%rH. The band at 1115 cm^{-1} is the highest frequency Raman mode of mica. No other mode is detected above this wavenumber.

2.12. Epitaxial Gold Au (111) on Mica

Gold is an element with atomic number of 79 and symbol of Au. Chemically it is a transition metal and is considered as a noble metal. As a result, gold does not react with oxygen in ambient conditions or higher temperatures.[98] Therefore, it remains stable as within experiments requiring a highly conductive substrate and ambient conditions. Epitaxial gold can be grown over various surfaces such as Muscovite mica freshly cleaved crystal or glass within a controlled high vacuum depositing system. Often depending on the thickness of the gold grown over the surfaces, the morphology of the film varies, in which case, films thinner than 200 nm demonstrate islands and terraces of gold over the mica or glass with gaps and holes separating or in between them. Often a thickness of 200 nm over freshly cleaved mica is reproducibly manufactured and is commercially available.

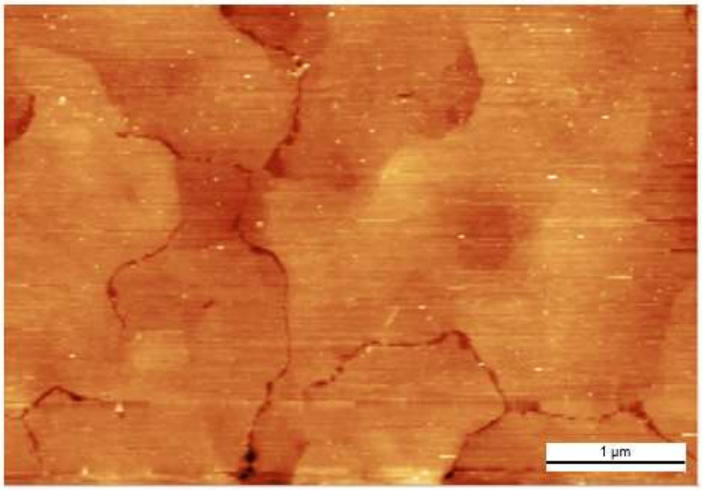

Figure 2.20, Scanning force microscopy height image of Epitaxial Au (111) grown over the Muscovite mica.

2.13. Scanning Probe Microscopy

Scanning Probe microscopy (SPM) has been one of the most influential microscopy methodologies of the 21st century. It was invented in 1986 by Binning et al.

as a surface characterization methodology[99] initially known as scanning tunneling microscopy. In SPM, a probe is often used to interact with the matter at the interface of interest under ambient, liquid and or vacuum environments. The probe may interact, mechanically, chemically, electrically and or through quantum tunneling of electrons with the molecules or atoms of the various interfaces as it periodically scans over an area. The probe follows the topography of an interface following changes of the interaction between the probe and the sample interface.[100] There exist various modes of SPM and they are often called differently, yet the common factor between them is the scanning process of the surface of interest using a probe interaction with that interface.

In this study, scanning probe microscopy (SPM) was employed as a methodology to understand the topography, nanomechanics, and structure of the functionalized 2D carbon-based structures and their two-dimensionality at scales of few nanometres up to a few micrometres. Scanning force microscopy (SFM), also known as Atomic force microscopy or scanning force microscopy (AFM or SFM), is a subset of probe microscopy that includes the measurement of the attractive and repulsive forces acting between the atoms of the probe and the interface of interest. SFM measurements are based on a micro cantilever with a very sharp pyramidal tip apex or blunt spherical tip at the free end, acting as an optical lever (probe) and interacting with the interface of interest (sample). In SFM, the material and geometry of the micro cantilever define its spring constant and consequent sensitivity to forces of interactions. For the cantilever probes to be sensitive to the interatomic forces of attraction and repulsion, the spring constant must be smaller than that of the interatomic spring constant of the sample crystal lattice or molecular arrangements. To have such small spring constant values, the cantilever probes are often in the micrometer dimensions.

The bending of the cantilever concerning the load applied to it is monitored as the reflected laser beam from the cantilever's Aluminum or Gold coating is detected by a set of photodiode arrangements. The photodetectors often consist of multiple photodiodes arranged together in square or other forms to detect the vertical and horizontal movement of the laser beam position reflected from the cantilever. [101,102] The SFM probe is located at the free end of the cantilever and is often geometrically

pyramidal with a typical apex radius of ~7 nm, which could be as sharp as ~1 nm too. [103] The force between the probe tip and sample interface is absolutely directly proportional to the distance between them. SFM obtains force and topographic information of the sample based on the interatomic forces within the regions of repulsion and attraction, as also described in the Leonard-Jones potential for probe tip and sample interatomic distances.

$$V_{LJ}(r) = 4\varepsilon \left[\left(\frac{\sigma}{r}\right)^{12} - \left(\frac{\sigma}{r}\right)^{6}\right] \qquad \textit{Equation 3}$$

Where r is the distance between two interacting atoms (atoms from the probe tip and sample interface), ε is the depth of the potential energy and σ is the distance at which the particle-particle potential energy V is zero.

There are two commonly used modes of SFM microscopy that are known as, contact mode and Tapping mode. Another SFM mode that is currently growing in its popularity of use is Quantitative nanomechanical mapping (QNM) also known as Quantitative imaging mode (QI) mode. In this study, I utilize both Tapping modes and Quantitative nanomechanical mapping mode. As it can be seen in Figure 2.21 and Figure 2.22 the interaction forces between tip and the sample causes a deflection of the cantilever, changing the reflected position of the laser beam from the cantilever probe onto the photodetector.

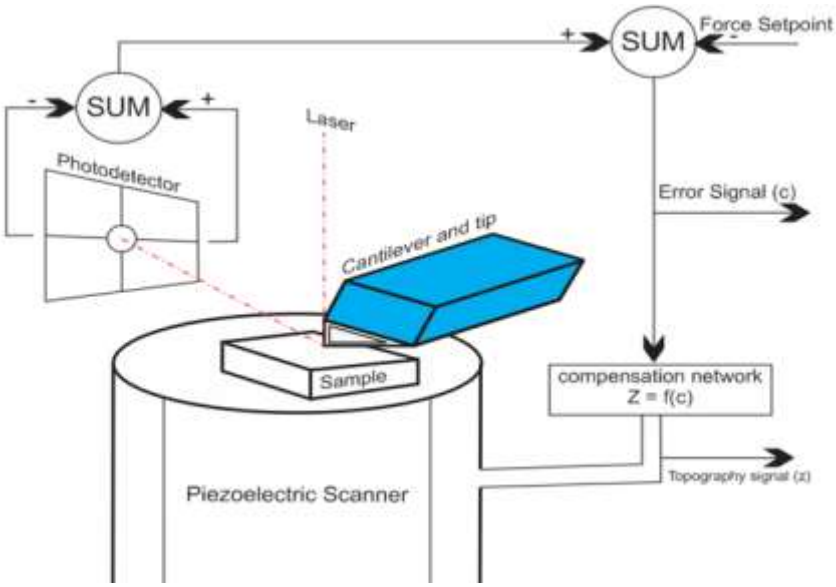

Figure 2.21, Feedback loop system in Scanning force microscopy.

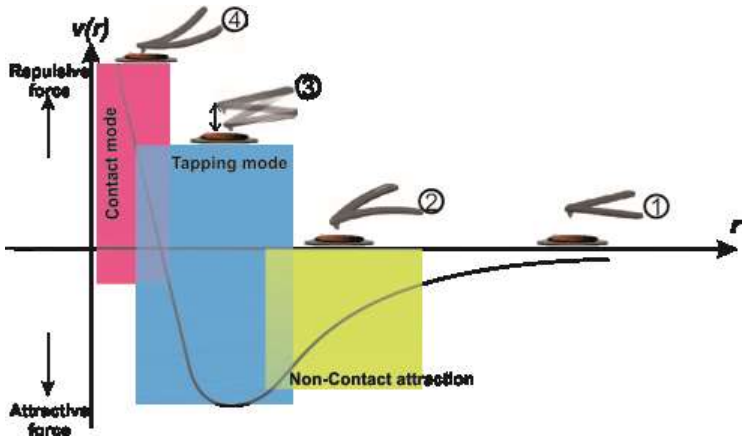

Figure 2.22. Scanning force microscopy modes overlay on Leonard Jones potential curve for interatomic forces.

2.13.1. Contact mode

Scanning force microscopy in contact mode was the original methodology utilizing a constant applied force during the scanning of the sample interface. A probe that is within the repulsive regime of the Lennard-Jones interatomic potential (Figure 2.22) with the sample interface follows the topography of the interface. Keeping the probe tip in the constant repulsive regime potential requires constant bending of the cantilever probe. This is achieved by means of a feedback loop system that works based on the laser reflection from the cantilever probe, as seen by the photodiode (Figure 2.21).

Therefore, the probe tip always exerts a constant setpoint force while in contact mode scanning of the sample interface. During scanning, the piezoelectric Z-scanner is responsible for adjusting for variations of the probe tip and sample distance while maintaining the cantilever probe bending constant within the feedback loop signal. This method allows for following the topography of hard and rigid interfaces, such as crystals and atomically flat layers of graphene.

Voltage used by the feedback system to adjust the Z-piezo scanner extension or retraction following the sample interface is a measure of sample height variations. Contact mode can be destructive to adsorbed molecules at interfaces, as it can manipulate their configurations and locations via exerted shear forces during constant force scanning. Therefore, tapping mode, or the oscillatory mode of intermittent contact with the sample interface, was invented.

2.13.2. Tapping mode Scanning Force Microscopy

Tapping mode SFM is based on the prevention of sample interfacial modification by the shear forces induced by the SFM probe onto the sample interface, as was observed in case of SFM contact mode. This is achieved by the aid of a piezoelectric crystal in physical contact with the micro cantilever base and that oscillates the cantilever probe with a frequency close or equal to the cantilever's natural resonance frequency. Thus, the micro cantilever probe of the SFM will be oscillating between the attractive and repulsive regimes based on the Leonard-Jones potential can be modelled as a driven and damped harmonic oscillator. This minimized the contact between the probe tip and the sample interface, preventing excessive shear forces resulting in surface manipulations in lateral and vertical directions. The oscillatory excitation of the cantilever is also possible to be carried out using photo thermal excitation (cyclic thermal expansions) with a laser beam focused at the base of the cantilever body.[104]

Due to the nature of Tapping mode SFM in oscillating the probe tip within the repulsive and attractive regimes of the interatomic distances, it can be modeled as driven and damped harmonic oscillator. A harmonic oscillator experiences a force directly proportional to a displacement quantity as it undergoes harmonic motion modeled as a sinusoidal displacement from equilibrium.

$$F = -k\,x \qquad \textit{Equation 4}$$

$$ma = -kx \qquad \textit{Equation 5}$$

$$x(t) = A\cos(\omega_0 t + \varphi) \qquad \textit{Equation 6}$$

Were φ is the phase and ω_0 is the undamped angular frequency, $\omega_0 = \sqrt{\frac{k}{m}}$

In Tapping mode, the oscillating tip experiences both a driving force and a damping force, either due to the environment and tip-sample interactions. According to Newton's second law, forces present in a driven and damped oscillator can be considered through force balance as below:

$$F = mx = m\,.\,\frac{d^2x}{dt^2} = -kx \qquad \textit{Equation 7}$$

The force of damping is then expressed as a frictional force in an opposite direction to the movement of oscillator. With “b” being the damping coefficient.

$$F_{damping} = -b\frac{dx}{dt} \qquad \textit{Equation 8}$$

The expression for driving force of the (tip) oscillator is written as:

$$F_{driving} = F_0\ cos(\omega t) \qquad \textit{Equation 9}$$

Where F_0 is the maximum amplitude and ω is frequency. The sum of all the forces

present in the system can be written as the expression for a driven and damped oscillator.

$$\sum F = F_{driving} + F_{spring} + F_{damping} = m.\frac{d^2x}{dt^2} = -kx - b\frac{dx}{dt} + F_0 cos(\omega t)$$

Equation 10

Equation 7 is then solved by rewriting it in the form of,

$$\frac{d^2}{dt^2} + 2\gamma\omega_0\frac{dx}{dt} + \omega_0^2 x = \frac{1}{m}F_0 sin(\omega t) \qquad \textit{Equation 11}$$

Where F_0 is the driving amplitude and ω is the driving frequency of the sinusoidal driving mechanism.

Meanwhile, the damping ratio can be calculated by the $\gamma = \frac{c}{2\sqrt{mk}}$ as it will define the behavior of the damped driven oscillations of the probe. Where for $\gamma > 1$ oscillator is overdamped and so its oscillations decay to a steady state. For the case of driven oscillator probe in microscopy, the overdamping can occur due to experimental parameters and environmental factors such as oscillation amplitude, sample topography variations and water meniscus formation between probe tip and sample interface.

Furthermore, for $\gamma = 1$ the oscillator is critically damped and that signifies its return to steady state to be as soon as possible. However, in case of the $\gamma < 1$ the system is underdamped.

Tapping mode involves oscillation of the SFM probe tip at or close to its natural resonance frequency in either 1st, 2nd or higher eigenmodes. [105] often the these

eigenmodes are based on the geometry of the SFM cantilever probe and ranges are between few to hundreds of kHz.

Proportionality of the steady state solution to the driving force and induced phase change of φ is unavoidable. Both the amplitude and the oscillation frequency of the cantilever probe of SFM may be modified as it gets closer to the interface of the sample. These are due to various forces such as electrostatic or Van der Waals or even effect of meniscus of water. Therefore, the damping of the amplitude or frequency shift could be used as a trigger of feedback to control the distance of the cantilever probe from the sample interface. Feedback loop then reacts to the variation of the sample topography as the oscillating cantilever probe tip is scanned line by line over its interface. The oscillation amplitude and frequency of the tip is damped as it transits over surfaces of different heights or chemical difference. This is both an advantage and disadvantage of Tapping mode SFM as the chemical variation of the sample with similar height topography may still result in tip amplitude change and consequently unrealistic height measurements. These height artifacts and uncertainties are mostly inherent in tapping mode and are due to the difference between Hamaker constants of different materials which SFM tip interacts with.[106] Therefore, to accurately and reproducibly avoid the uncertainties of the height measurements by Tapping mode SFM and manipulative shear forces inherent within the contact mode SFM, the third mode of scanning force microscopy, namely, Quantitative Nanomechanical mapping & Quantitative Imaging are of great interest.

2.13.3. Quantitative Nanomechanical mapping & Quantitative Imaging (QNM-QI)

A great advancement of the scanning force microscopy was the development of the new Nano mechanical probing modes. Unlike the Tapping mode SFM, Quantitative Nanomechanical mapping (QNM) and Quantitative imaging mode (QI) are not subject to the height artifact measurements due to chemical variations of the sample interface. This is mainly because nanomechanical mapping in SFM does not use tip oscillation amplitude variation as height feedback trigger. In this mode of SFM, data is collected as the cantilever probe undergoes approach until repulsive interaction with sample interface reaches a previously set quantity. This is done based on the

deflection of cantilever which depends on its cantilever probe spring constant. It is possible to accurately control and measure applied force to the sample along with topography variation detection. The height signal trigger in these nanomechanical modes is dependent on the deflection of the cantilever probe of specific sensitivity and as it reaches a set-point applied force onto the sample. Therefore, it is possible to extract also a zero-force height topography of the sample in various environments, vacuum, air or within clear liquids. That is topographical measurements of the sample with experimentally minimal manipulative normal forces (isoforce).[107]

During approach of the cantilever probe, parameters such as pull-in force is measured as cantilever bends downward towards the sample, that is due to the attractive interaction between the probe tip and sample interface. As the approach further continues, cantilever bends upwards and reaches its initial bending state (relative to its status far away from sample interface), that is point of contact with sample but with zero force applied. Further upward bending of the cantilever probe is possible as it approaches further into the sample interface. This upward bending of cantilever can continue until a previously setpoint bending threshold in units of nm/V is achieved. Sensitivity of the cantilever plays a direct role in conversion of its bending into a quantified applied force onto the sample interface. This depends on calibration of the bending of the cantilever in units of nm in relation to the reading from the SFM photodiode arrays variation in Volts that depends on the variation of the position of laser beam reflection from the cantilever reflective coating (Figure 2.23). Sample deformation and elasticity can be extracted from the bending behavior of the cantilever probe during approach into the sample interface. Additionally, during reversing of the approach of the cantilever probe, pull-off force (adhesion of tip and sample) and hysteresis (variation of the cantilever deflection vs sample distance between approach and retract) are measured.

In QNM and QI mode tip is not oscillated but rather it is approached and retracted from the sample surface using either a sinusoidal (QNM) or a triangular movement (QI). As it approaches, cantilever and tip are subject to an attractive force with sample which may include also the contribution of the meniscus of water molecules between tip and sample, if the experiment is carried out in ambient atmosphere. The tip-sample separation may include various forces including but not limited to the specific and non-specific pull-off (adhesion) interactions. Calibration of

the cantilever bending is further explained in 3.8. Stiffness and Young's modulus of the sample can be extracted from the slope of the force-distance curves (calibrated cantilever deflection vs tip sample distance curve).

Sensitivity of the cantilever is calculated based on the slope of the cantilever deflection reading from photodiode array vs distance traveled by the cantilever towards sample (Z-Piezo movement). Sensitivity estimation is absolutely required in conversion of the cantilever deflection into quantified force applied by the probe tip onto the sample interface.

Forces involved in the SFM nanomechanical mappings can be written in general, as the sum of elastic ($F_{elastic}$) and inelastic forces ($F_{inelastic}$) of interactions. First approximation of the forces can be written as:

$$F_{total} = F_{elastic} + F_{inelastic} \qquad \textit{Equation 12}$$

The sample is modelled by two independent parameters, such as the Young's (elastic) modulus E and the Poisson ratio ν. Elastic constants can be expressed as a function of any two other constants. Therefore, the concluding expression is expressed in terms of the bulk modulus *K* and the shear modulus *G*.[108,109]

In a tip–sample interface interaction, it is common to introduce an effective elastic modulus also known as "reduced elastic modulus" E_{eff}.

$$\frac{1}{E_{eff}} = \frac{1-\nu^2}{E} + \frac{1-\nu_t^2}{E_{tip}} \approx \frac{1-\nu^2}{E} \qquad \textit{Equation 13}$$

$$F(D_{Def}) = \frac{E}{1-\nu^2}\frac{\sqrt[4]{r_{tip}}}{3} D_{Def}^{\frac{3}{2}} \qquad \textit{Equation 14}$$

Since the sample and tip both have finite elastic modulus then the E_{tip} is important to be considered. F denotes the force, E is young's modulus, ν is Poisson ratio and r_{tip} is the SFM probe tip radius. D_{Def} is the deformation depth. Various models of the material elasticity, adhesion and deformation has been defined. However, mainly Hertz model of contact for a SFM tip of paraboloid [110] and a relatively planar sample surface is valid and also could be used while experimentation in liquid as no further meniscus effects exist. As it can be seen in the Figure 2.23 C & D, Approach and Retract force distance curves each contains the mechanical information of the sample interface. In approach curve we can expect information regarding the extend of

Deformation, $D_{Def} = D_{Flow} - D_{Fi}$ That is the numerical difference of tip-sample distance at any setpoint force smaller than that of setpoint force (PeakForce).

Retract force distance curve contains Energy dissipation of the process as well as the tip sample adhesion forces and often is used for extraction of the Young's Modulus value of the Sample. However, Hertz and Derjaguin-Müller-Toropov (DMT) [111] models both could be used to fir approach force- distance curves and extract Young's Modulus of sample.

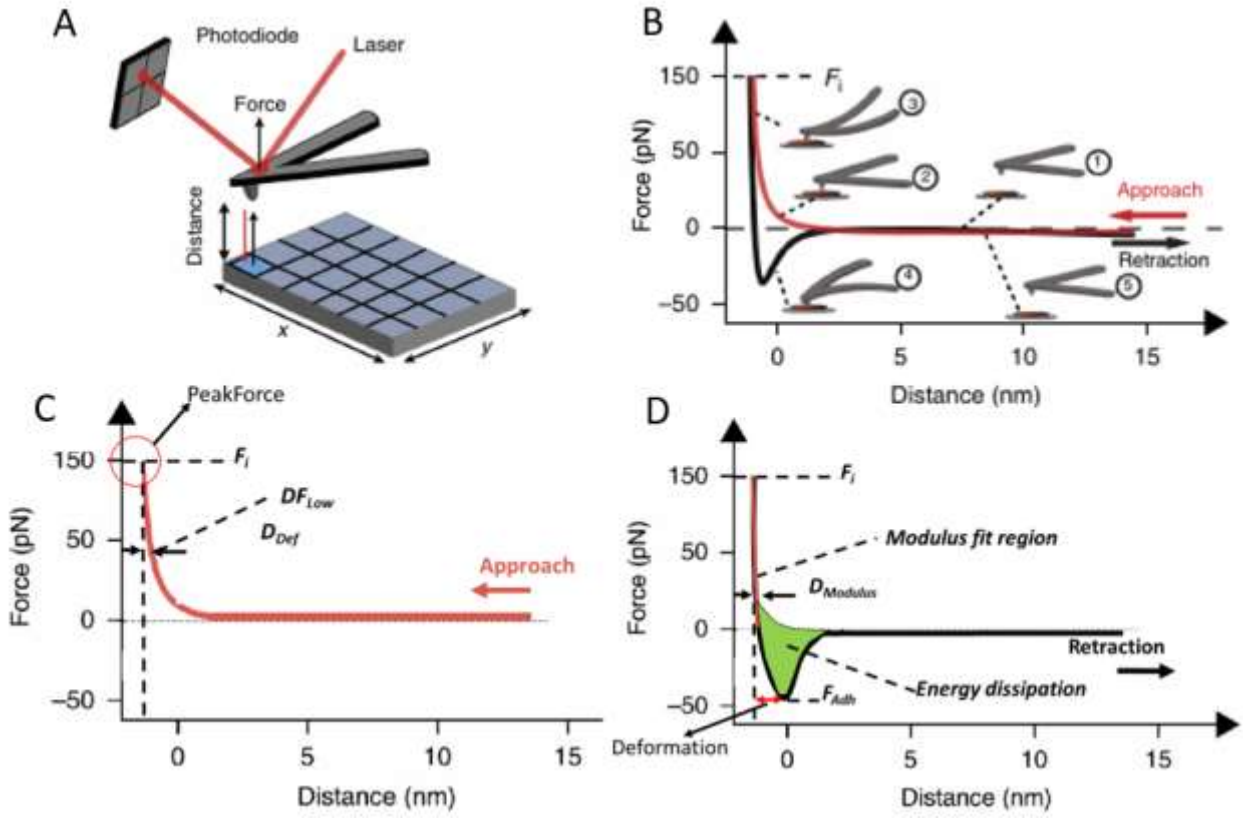

Figure 2.23, SFM-QNM & QI Schematics. A) Schematics of the tip-sample interaction during QNM and QI imaging modes. B) Force calibrated SFM probe Cantilever bending as a result of tip-sample interactions during approach and retract data collections. C) Approach data curve and the noted information within it. D) Retract data curve and the important data points contained within it. Adapted from reference [112].

2.13.4. Scanning force microscopy Tunneling current – (Peak Force TUNA)

Scanning force microscopy in Peak Force tunneling current (TUNA) mode is also known as SFM-PFTUNA. It is a relatively new mode of SFM and is based on

Quantitative nanomechanical mapping with ability to measure contact current during approach and retract steps. SFM-PFTUNA can measure the resistivity of the nanostructures on conductive substrates only. A conductive cantilever probe is often made of Platinum or Silicon or silicon with oxide layer coated by a 100 nm thick layer of Platinum is used to quantitatively map contact current of the sample in addition to measurement of nanomechanical variations of the sample interface.

The measured quantitative values of this mode of SFM are limited by the stiffness, conductivity and roughness of the measured interfaces. For this method, substrates such as Au (111) or HOPG or other conductive and atomically flat substrates would be required.

SFM-PFTUNA is in principle very similar to the SFM-QNM or QI with main difference of having an extra step between approach and retract of the cantilever. That is the contact current flow measurement due to applied voltage bias between the sample and tip during the contact time while reaching or at the setpoint force. Therefore, not only force – distance curves are extracted but also a Current-Distance curve and I-V spectroscopy data can be extracted for each point of the sample interface during pre-defined duration of tip-sample contact with time.

SFM-PFTUNA is advantageous in compare to scanning tunneling microscopy, mainly due to its robust handling of the complicated and rough sample interfaces. This is because the contact current over a rough interface is measured rather than the tunneling current over a smooth sample interface during the microscopy.

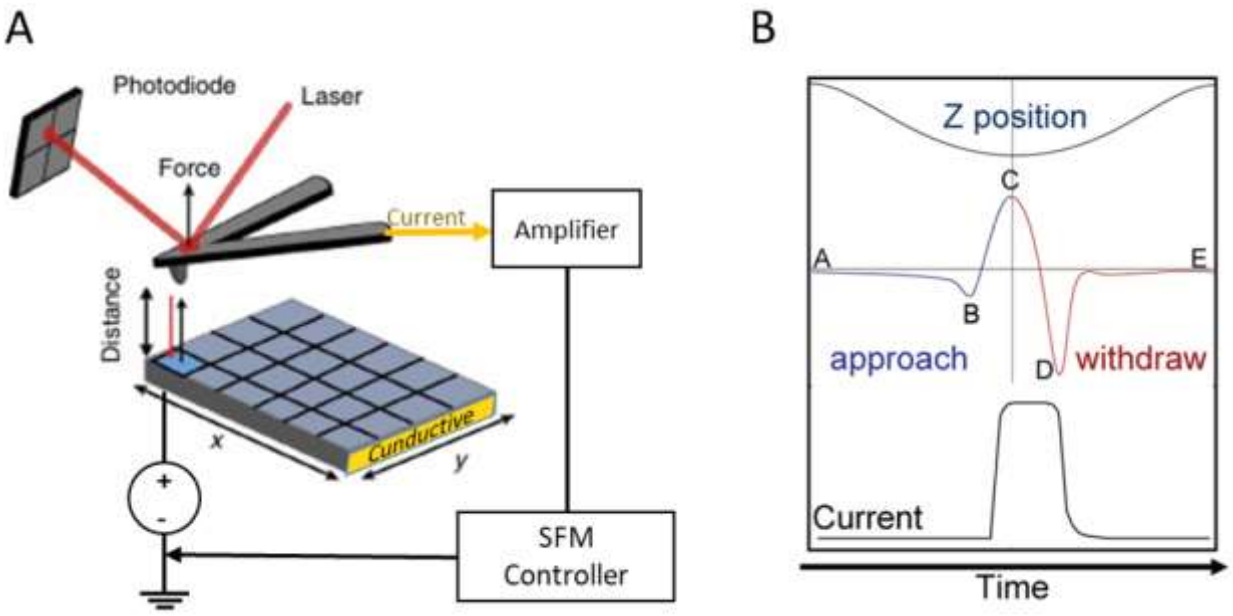

Figure 2.24, Schematics of SFM-PFTUNA. A) Schematics of approach and retract of the conductive SFM probe onto a conductive substrate and sample in SFM-PFTUNA. B) The position, Force and Current as a function of time during one SFM-PFTUNA. Blue indicates approach curve while red indicates retract curve data.

2.13.5. SFM tip Broadening

Lateral dimensions of objects in SFM height images are broadened by the finite SFM tip apex size. This is known as SFM tip dilation or convolution, which is highly relevant in case of estimation of the lateral dimension of molecular structures. The SFM tip dilation becomes critical to be avoided when the molecular structure measured by SFM is expected to have lateral dimensions smaller than that of the SFM tip apex.

A geometry-based calculation can result in estimation of the radius of the tip from measurement of objects of known dimensions or geometry for example gold Nano particles with precise diameters.

$$FWHM = 2\sqrt{2R_{tip} + R_{sample} + R_{sample}^2} \qquad \textit{Equation 15}$$

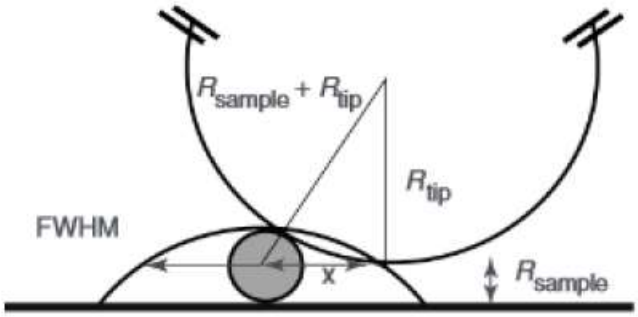

Figure 2.25, Estimation of SFM tip broadening for a spherical object.

In the case of the measurements carried out within this research, I estimated the broadening of the VSV virus particles by the SFM tip apex. As the SFM tip apex radius is much smaller compared to a VSV particle, the apparent width can be calculated by assuming the SFM tip has a pyramidal shape terminated by a hemispherical tip apex. I also assume, for simplicity, a rectangular cross-section object. Therefore;

$$\text{SFM Imaged object width} = 2\left(X + R_{tip}\right) + real\ object\ width$$

$$X = \left(\text{Measured object height} - \mathrm{R_{tip}}\right) \cdot \tan\theta$$

With θ is the tip cone half angle (18° according to the tip manufacturer) and R_{tip} is the radius of the SFM tip apex.

2.14. Raman Spectroscopy

2.14.1. Theory

Raman spectroscopy, introduced by CV. Raman in 1928, who was later awarded the Nobel Prize in Physics in 1930 for his work on light scattering and the subsequent phenomena named the Raman effect[113], it involves the "elastic" or "inelastic" scattering of light, typically in the visible range of the electromagnetic spectrum, after interaction with matter (optical phonons)[114]. This non-destructive and rapid spectroscopy technique enables the identification of materials, both in a general and specialized context. The "inelastic" scattering of light in Raman spectroscopy involves an energy exchange between the incoming light photon and a molecule. This exchange results in the photon gaining or losing energy, which can be observed by

recording the energy change in the scattered photon. The Raman spectrum provides information about this energy gain or loss, known as Stokes or anti-Stokes shifts in the inelastic scattering process. The shift in the energy of the scattered photon, compared to the initial energy of the incident photon, is expressed as the Raman shift and is measured in wavenumbers (cm-1).

Interaction of the electromagnetic waves and matter could be described as both a wave or particle interaction. In classical physics, Raman effect is mainly based on the interaction of electric field of an electromagnetic wave with electrons and nuclei of a molecule or atom and associated with polarizability α.

$$\vec{p} = \alpha\vec{E} \qquad \textit{Equation 16}$$

Where α is atomic polarizability and E is the electric field, and p is the induced dipole moment. The electric field E of the light exerts a force on all electrons, and tends to displace them from their average positions around the positively charged nuclei. This is polarization of the molecule. According to the "Gross selection rule" [115] the α of a molecule varies during vibration. Therefore, when an oscillating electric field is present, such as electric field of an incident laser beam, it can be expressed as:

$$E = E_0\, sin(\omega_i t) \qquad \textit{Equation 17}$$

As a consequence of oscillating electric field and induced dipole, a vibration is induced within the crystal lattice of atoms with a frequency of ω_q that is in sync with the optical field.[116]

$$\alpha = \alpha_0 + \alpha_1\, sin(\omega_q t) \qquad \textit{Equation 18}$$

The polarization via the electric field is then can be shown by a rearrangement of the equations:

$$\begin{aligned} \vec{p} &= E_0(\alpha_0 + \alpha_1 \sin(\omega_q t)) \sin(\omega_i t) \\ &= E_0 \left[\alpha_0\, sin(\omega_i t) + \frac{1}{2} a_1 \cos(\omega_i - \omega_q)\, t - \frac{1}{2} a_1 \cos(\omega_i + \omega_q)\, t\right] \end{aligned}$$

Equation 19 (from reference [117])

Above equations describe the fundamental interaction between the light and molecular or atomic structures that result in the elastic scattering (Rayleigh scattering) or inelastic scattering of light known as Raman scattering. Inelastic scattering involves loss or gain of the photon energy that is also equal to the energy difference between initial and final electronic levels. [118]

In this study Raman spectroscopy and Raman mapping was utilized to identify the structure of the 2D carbon-based Triazine structures. It is known that the identification of the number of graphene layers is possible using Raman spectroscopy.[119]

2.14.2. Raman spectra of Graphene

Graphene Raman spectra can be considered as one the most informative data sets on the structure and extend of its crystallinity. This is not limited to the graphene but also to other 2D carbon-based structures. Raman spectroscopy would provide immense information in regards to the number of layers, presence of charges at interface, doping, strain,[120,121] polymorphism, structural defects, edge forms and further density of defects for graphene sheets. There are special features in the Raman spectra of graphene that their band positions, band widths and even just by observation of them, various information regarding the atomic scale structure of graphene could be concluded both qualitative and quantitatively. This methodology would complement other microscopy methods in deeper understanding of novel 2D carbon-based structures and also effect of functionalization on the atomic scale of 2D carbon-based nanosheets.

Raman spectra of Graphite and Graphene demonstrate typical features that are specified with names and their Raman shift wavenumber. Each of the Raman bands observed for the Graphitic structures provide various information at its atomic scale as it provides an understanding of phonon dispersion within graphene. The two typical Raman bands of Graphitic structures are G band at ~1580 cm^{-1} and G´ also known as 2D band at ~2700 cm^{-1}. Other typical Raman features often observed for graphene are D band at 1350-1360 cm^{-1} and D' band at ~1610-1620 cm^{-1}. [121,122]

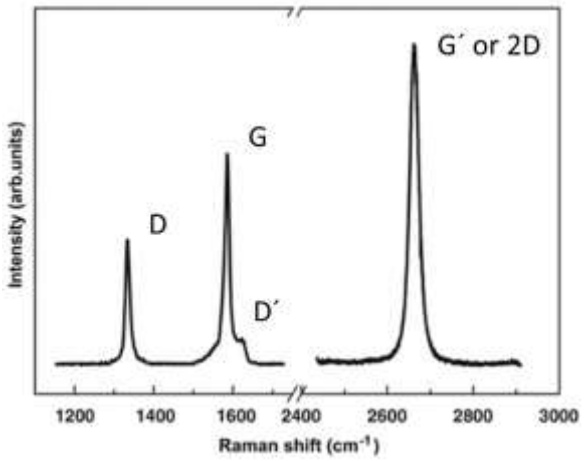

Figure 2.26, Example Raman spectra of Graphene. G and 2D bands are always observed and D and D´ bands observations depend on the physical status of the graphene. Adopted from reference [120].

The G band has been discovered to be due to the stretching of the sp^2 carbon atoms in the basal plane of graphene. The 2D band (G') has always been observed independent of the presence of physical defects within the basal plane of graphite or graphene. However, it is called 2D since it is observed at the doubled frequency of the D band while being a second-order phonon activity that is not affected by defects.[119] Furthermore, the shape and symmetry of the 2D band have been utilized to define the number of graphene layers (Figure 2.28). For example, the observation of a sharp 2D band in graphene denotes a single-layer graphene, and as the number of layers increases, the 2D band width increases and becomes further unsymmetrical.[125]

In regards to the G band in single layer graphene, it is a result of the in plane Transverse optical (iTO) and in plane longitudinal optical (iLO) phonon modes at the Brillouin zone center and It is the first order Raman scattering. [120] in comparison to G band, 2D and D bands are both due to a second order Raman scattering process. Additionally, it has been demonstrated in previous experimentations that the width of the G band increases with increase in the sp^3 C-C bonding within the graphene plane.[125] This is specifically further observed in case of the Raman spectroscopy of the amorphous Graphene oxide sheets.[126] Therefore, depending on the shape of the G band it is possible to qualitatively infer regarding the extend of polymorphism of the graphitic structures.

The D band of graphene is activated when structural defects exist within the basal plane, as it is affected by the hexagonal ring breathing modes of the C-C

bonds.[121] The D band is also observable when Raman spectra are collected from the edges of the graphene sheets, where armchair or zig-zag arrangements are possible due to incomplete ring structures. The D band is often observed in graphene sheets produced through the chemical vapor deposition methodology and is often absent in mechanically exfoliated graphene sheets. [121,123,124]

Furthermore, in regards to the D´ band, as shown also in the Figure 2.27, the band is observed due to a weak disorder within the structure that is known to occur because of a double resonance process. Various literature has shown that the D´ band is experimentally observable when there exist a charge doping at the interface of the graphene sheet. [127–129]

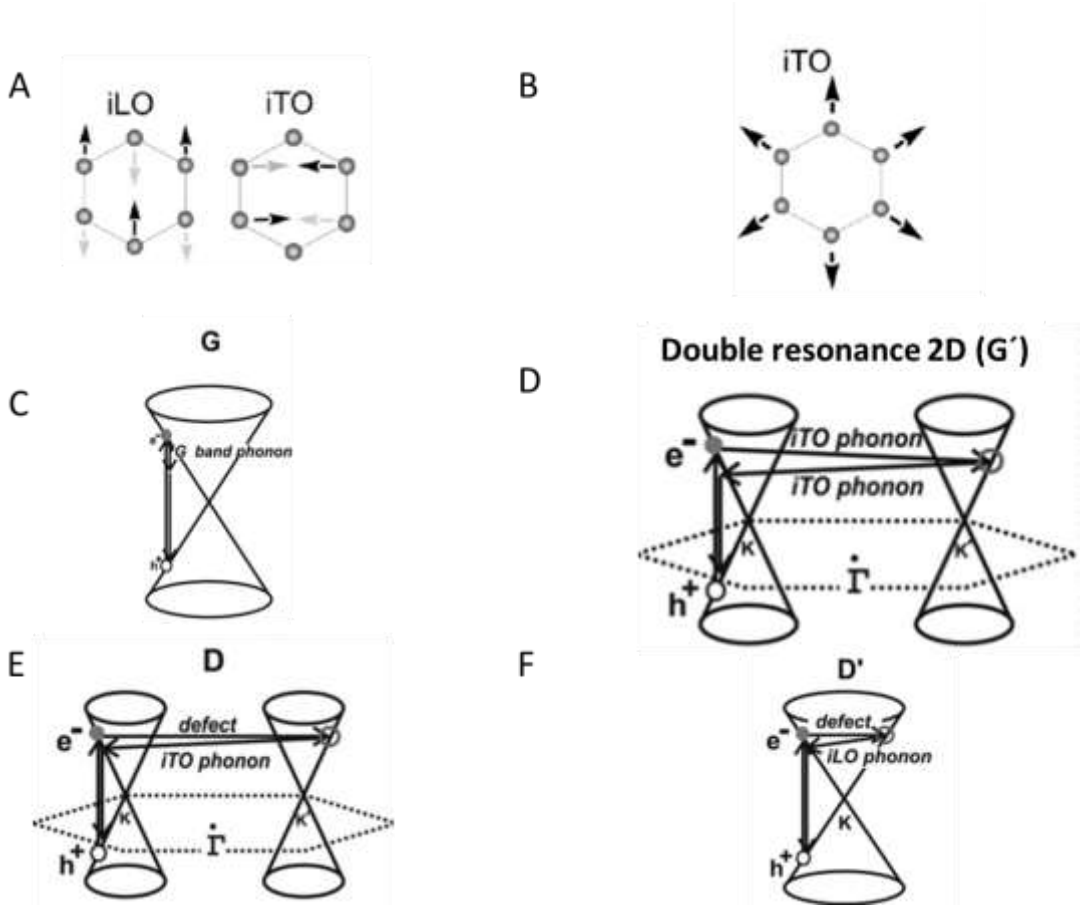

Figure 2.27, Stretching and breathing modes of Graphene ring. A) in plane stretching of G band. B) vibrations associated with the 2D band. C) schematic representation of first order single resonance process for G band. D) representation of the two phonon and second order double resonance process for 2D Band. E) representation of one phonon and second order double resonance for D band. Adapted from reference [120].

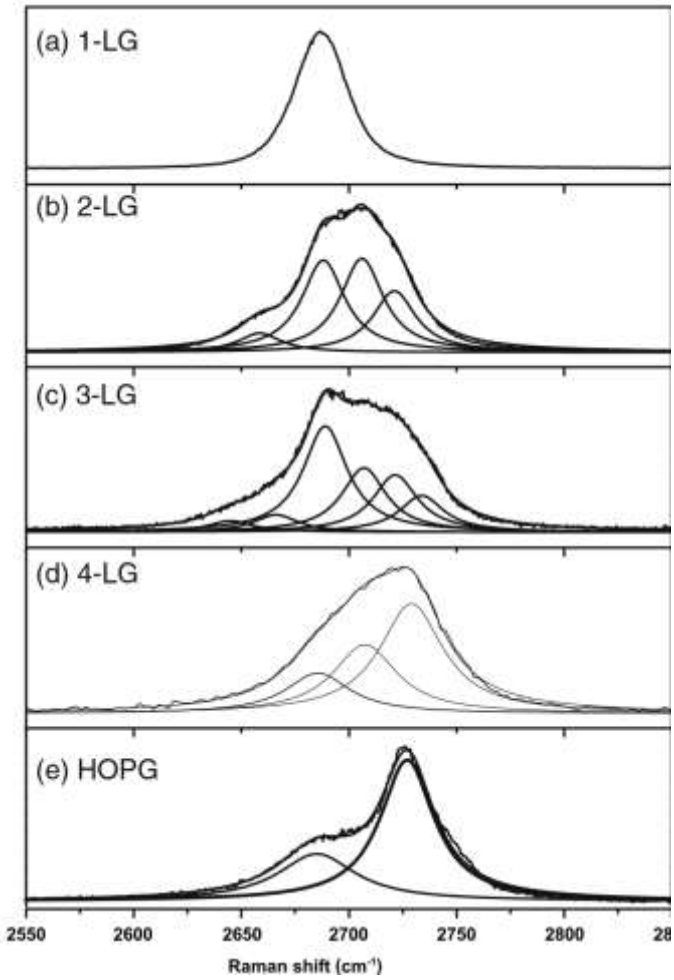

Figure 2.28, G´ or 2D band variation and number graphene layers. a) single layer graphene. b) 2 layers of graphene. c) 3 layers of graphene. d) 4 layers of graphene. e) highly oriented pyrolytic graphite crystal. Adopted from reference [120].

Chapter 3

3. Experimental & Methods

In this chapter, the experimental procedures and methods are explained in detail. The rationale behind the order of the description of methods and experiments is based on the order of the motivated questions as discussed in the Introduction chapter of this thesis. To reiterate, to achieve the initial aim of characterizing novel 2D functionalized carbon-based sheets, experimental sample preparation followed the requirements of scanning force microscopy for interfacial experimentation and observation of those materials. Later, to answer the question of whether viral interaction (immobilization) is possible with the novel functionalized 2D carbon-based sheets, sample preparations were adjusted to experiment with the hypothesis that no interaction may exist unless observed within experiments. The hypothesis considers that if viral particles do not immobilize at the interface of the material, they have minimal successful interaction, and consequently, minimal inhibition is expected.

Additionally, the size variation of viral functionalized 2D sheets was addressed statistically, which was later observed from virologists experiments to affect viral interactions quantity and consequently the inhibition capability of viral infections[130]. Furthermore, the question of what is the electronic effect of "graft to" functionalization on 2D carbon-based sheets was addressed via SFM-PFTUNA methodology, which is an extension to SFM-QNM and SFM-QI that was used in previous experiments.

Confirmation of ccapability of functionalization of 2D carbon-based sheets perpendicular to their basal plane using Triazine molecule has been part of the experimental objectives as described previously. However, the possibility of in plane trimerization of the triazine as a monomer molecule and 2D growth in plane is then experimented with in the last segment of this chapter. Investigations is carried out using both scanning force microscopy and Raman spectroscopy. These experiments include sample preparations for questioning the 2D nature of the triazine-carbon-based material synthesized as 2D triazine -carbon structure and it extend of crystallinity as investigated via Raman spectroscopy.

Initially, sample preparations of the novel functionalized 2D carbon-based structures for experimental methodologies are described based on the publications in

which they appear. Later, measurement methodologies, instrumentation setups for experimentations are described based on the publications they are referenced to in each section.

In more details, I will describe the sample preparation methodologies and steps for the investigations carried out in my research works. These include the sample preparation steps that I carried out for investigation of functionalized 2D and carbon-based interfaces and their interactions with the viral inhibitors in addition to the SFM and Raman spectroscopy characteristics of Triazine – carbon-based structures. Methods and descriptions mentioned in this chapter are based on the descriptions in publications [32,97,130–133].

3.1. Preparation of "Graft to" Functionalized Graphene Interfaces

This section describes the sample preparation for the experiments in relation to the characterization of the TRGO sheets functionalized with Triazine and post functionalized with hyperbranched polyglycerols according to the methods described in the publication by Gholami *et al*. and Faghani & Gholami *et al*. Furthermore it includes experimental preparation for observation of Viral particles and their interactions using scanning probe microscopy as described by the publication of Gholami *et al.*[32] . Similar experimental sample preparations for characterization of the TRGO sheets and their functionalization was also carried out as described in Faghani & Gholami *et al.*[97].

Samples were prepared by spin-casting of the TRGO suspensions from chloroform and the functionalized TRGO suspensions from deionized water onto highly ordered pyrolytic graphite (HOPG - grade ZYA, Advanced Ceramics). Spin casting process allows for an initial adsorption of the nano particles at the interfaces of the interest and removal of the solvent by the subsequent centrifugal force of spin coater sample rotation.

For this, the suspensions were applied onto a freshly cleaved HOPG surface for 1 minute for aqueous solutions and for a few seconds for chloroform solution, then spun off at 40 revolutions per second (rps).[32,97] To investigate virus interaction with TRGOs, a 10 µL droplet of 0.25 mg mL^{-1} VSV dispersed in phosphate buffer (PBS, Fisher Scientific) was deposited over the HOPG surface coated with the functionalized

TRGO sheets (as described previously) and incubated for 5, 10, 30, and 50 minutes, after which the droplet was spun off at 40 rps.[32]

To achieve expanded ability of data analysis, two scanning force microscopes were used, namely Nanowizard III (JPK GmbH) and Multimode 8, Nanoscope V (Bruker Corporation). Multimode 8 was operated with an E-scanner, that is a Piezo scanner capable of 100x100 μm scan area, in tapping mode at a typical rate of 5 min per image and in PeakForce-QNM mode at a typical rate of 10–15 min per image at 512 x 512 Pixels image resolution. Additonally, the JPK Nanowizard instrument was operated in QI mode at a typical rate of 10–17 min per image at 128 x 128 Pixels image resolution.

It is important to note that, the contact, i.e., zero force, point was extracted from the analysis of extent curves in QI mode of JPK Nanowizard and it was assigned to be the topographical height of the sample with minimal indentation deformation. Extracted zero force contact points for every force spectrum were used to create topography mapping images. Silicon tips on silicon nitride cantilevers with a tetrahedral base were used as the SFM probes and with a typical resonance frequency of 70 kHz and a spring constant of 2 N m^{-1}.[32]

The SFM probe tips exhibited a typical apex radius of 7 nm with an upper limit of 10 nm and a tip cone half angle of 18°, as specified by the manufacturer (Olympus Corporation). Experiments were carried out under ambient conditions. Deflection sensitivity was calibrated by acquiring force–distance curves on a sapphire surface (Bruker Corporation). Cantilever spring constants were calibrated using the thermal noise method. Set points in the range from 0.300 to 1 nN were used. The SFM images were processed and analyzed with SPIP (Image Metrology A/S) and JPK image processing software.

3.2. Preparation of Functionalized Graphene and Viral Model Mixtures

Interactions between graphene sheets and VSV were further investigated by SFM in Tapping and QNM modes. In these experiments, a droplet of buffered VSV suspension was deposited onto a HOPG surface previously coated with the

functionalized 2D Nanosheets. The droplet over the interface was incubated for 5, 10, 30, and up to 50 minutes. This method of preparation allows for unbound VSV to be removed upon spinning the mounting stage with the sample interface on top. Tapping and QNM-QI mode SFM imaging thereafter revealed if there was any immobilization of the viral particles present at the sample interface. This methodology has been previously described in publication by Gholami *et al*.[32]

3.3. Preparation of "Graft from" Functionalized Graphene Interfaces

This section describes the sample preparation for the experiments in relation to the characterization of the TRGO sheets functionalized by ring opening polymerization of the polyglycerols (Graft from) methodology as described by the publication of Ziem *et al*.[92,130]

Functionalized TRGO suspensions were initially ultrasonicated for 1–2 h in deionized water before spin coating onto highly oriented pyrolytic graphite (grade ZYA, Advanced Ceramics) or freshly cleaved muscovite mica surface (Ratan Industries) at 40 rps. To evaluate the sheet size two SFMs had been used, a Nanowizard III (JPK GmbH) and a Multimode 8, Nanoscope V (Bruker Corporation). Multimode 8 was operated with an E-scanner in tapping mode at a typical rate of 5 min per image and an image resolution of 512 × 512 pixels.

The Nanowizard instrument was operated in quantitative imaging mode (QI) at a typical rate of 10–17 min per image and an image resolution of 128 × 128 pixels. To distinguish the accurate height, the contacts point with sample interface at zero force of setpoint based on the extent curves in QI mode were extracted and was assigned to be topography. For this, silicon tips on silicon nitride cantilevers with a tetrahedral base were used. The typical resonance frequency of 70 kHz and spring constant of 2 N m^{-1} is considered for the SFM probes used in the process. The tips exhibited a typical apex radius of 7 nm with an upper limit of 10 nm, having a tip cone half angle of 18°, as specified by the manufacturer (Olympus Corporation). Experiments were carried out under ambient conditions. Deflection sensitivity was calibrated by acquiring force–distance curves on a sapphire surface (Bruker Corporation). Cantilever spring constants were calibrated using the thermal noise method. [134] Set points in the range

of 1–5 nN were used. The tapping mode SFM images were then processed and analyzed with an open source software Gwyddion and SPIP (Image Metrology A/S) in addition to the JPK image processing software. Lastly, the topography images were line flattened with first order polynomial to remove the bow artefact induced by the scanning piezo movement within height data sets.[130,131]

3.4. Incubation of functionalized Graphene Sheets & herpesvirus particles in SFM

The functionalized thermally reduced graphene oxide (TRGO) sheets were spin casted from their deionized water dispersion onto the surface of a freshly cleaved highly oriented pyrolytic graphite (HOPG, ZYA, Momentive Performance) at a casting time of 10 minutes and speed of 40 rps for 2 minutes. Scanning force microscopy in tapping and quantitative modes were carried out on the prepared samples using a Nanowizard 3 (JPK, GmbH) instrument. The Nanowizard 3 instrument was operated in Quantitative Imaging mode (QI) at atypical rate of 10-17 min per image and an image resolution of 128x128 pixels.

Similar to the previous experimental procedures described here, the contact, i.e., zero force, point was extracted from the analysis of extent curves in QI mode of JPK Nanowizard and it was assigned to be the topographical height of the sample with minimal indentation deformation. Silicon tips on silicon nitride cantilevers with a tetrahedral base were used with a typical resonance frequency of 70 kHz and spring constant of 1.7 to 2 N/m (OLTESPA-R3).

Such SFM tips often exhibited a typical apex radius of 7 nm with an upper limit of 10 nm, having a tip cone half angle of 18 degrees, as specified by the manufacturer (Bruker Corporation).

To observe the possible interactions between the functionalized 2D sheets and viral particles, were carried out under ambient conditions. Deflection sensitivity was calibrated by acquiring force-distance curves on a sapphire surface (Bruker Corporation). Cantilever spring constants were calibrated using the thermal noise method.1 Set points in the range of 1 nN to 7 nN were used.

The TM-SFM images were processed and analyzed with SPIP (Image Metrology A/S) and JPK image processing software. Topography images were line flattened with first order polynomial. For reference experiments, a 20 µL droplet of phosphate buffer solution (PBS) was placed onto the HOPG surface accommodating the functionalized sheets and then, the SFM scanning was carried out in liquid (PBS buffer).[130]

Furthermore, experiments including both the functionalized TRGO and UV exposed (deactivated) herpes virions were carried out by first deposition of the sheets onto a freshly cleaved HOPG surface and then addition of 5 µL droplet of the herpesvirus in PBS buffer solution with 15 µL of excess PBS buffer to create a 20 µL droplet on the surface of the HOPG containing functionalized sheets. Afterwards, scanning force microscopy in quantitative imaging mode was carried out to investigate the interaction of the functionalized TRGO sheets with herpes virions.[130]

3.5. 2D Nanomaterials surface area and lateral dimensions

This section describes the procedure of lateral size determination for the functionalized TRGO sheets as described in the publication by Ziem *et al.*[130]

Surface and lateral dimensions of the functionalized 2D carbon-based Nanosheets were measured based on the height image data sets from scanning force microscopy measurements. To carry out such an analysis, SFM height images were first flattened using first and then second order polynomials to remove the bow effect of the piezo movement during measurements. This was done by using Gwyddion software and selecting pixels with height value smaller than that of the single layer 2D Nano sheet observed are at the interface of freshly cleaved mica or HOPG surface.

After creating the height threshold selection of the substrate and flattening those regions. The selection area was inverted to select the pixels with height values larger than 1nm. This allowed proper selection of all the pixels with height values demonstrating functionalized 2D Nanosheet over the substrates.

Surface area was calculated based on the number of pixels, the scale and resolution of the SFM data set. Gwyddion v2.5 was used to create the height threshold selection masks and additionally using Grain analysis option to calculate the statistics

of the sample interface. This methodology described here was published as part of my contributions into the Ziem *et al.* Publication.[130]

Martin Diameter of the functionalized 2D Nanomaterials were calculated by considering the length of the area bisector of the irregular 2D Nanosheets. Additionally, Maximum Feret's diameters were also calculated from the images. Feret's diameter is the maximum distance between two points on an irregular 2D Nanosheet.

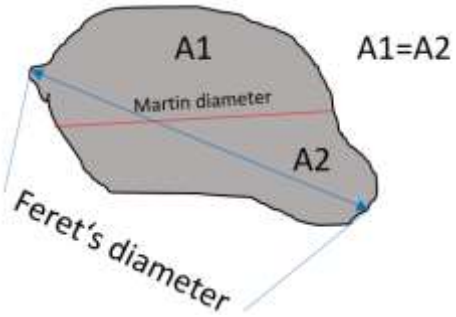

Figure 3.1, Martin diameter and Feret's diameter shown for an irregular projected area.

3.6. Preparation of Nanographene sheets at interface of Au (111)

This section describes the sample preparation for the experiments in relation to the characterization of the nano graphene (nG), nano graphene oxides (nGO) and nano graphene sheets functionalized by Triazine groups (nGTrz) as described within the publication of Guday *et al.*[132]

Samples were prepared by spin casting and spin coating from suspensions in deionized water for nano graphene oxide sheets and from chloroform dispersion in the case of nGTrz onto unmodified epitaxial Au (111) grown over mica (PHASIS, Swiss) and unmodified HOPG (grade ZYA, Advanced Ceramics). For spin casting, the samples were applied onto the Au (111) or HOPG surface for 60 seconds from solvent dispersions and then spun off at 50 rps for 60 seconds. For investigation of resistivity of the samples, a stainless steel (alloy 430) AFM/STM metal specimen disc, Ø12 mm was used to hold the substrates on top of the SFM scanner. Au (111) or HOPG substrates with or without coated samples were attached to the steel specimen disk using an isolative double-sided tape. A control resistor of 1 MΩ (or other values) was

attached onto the specimen disk and was simultaneously contacted with the Au (111) or HOPG Sample surface. Resistivity was measured between the back of the steel specimen disk and top of the Au (111) or HOPG using a multimeter and it was found to be in the range of the attached control resistor with 1% error. The SFM used in PFTUNA mode was a Multimode 8, Nanoscope V (Bruker Corporation). [132]

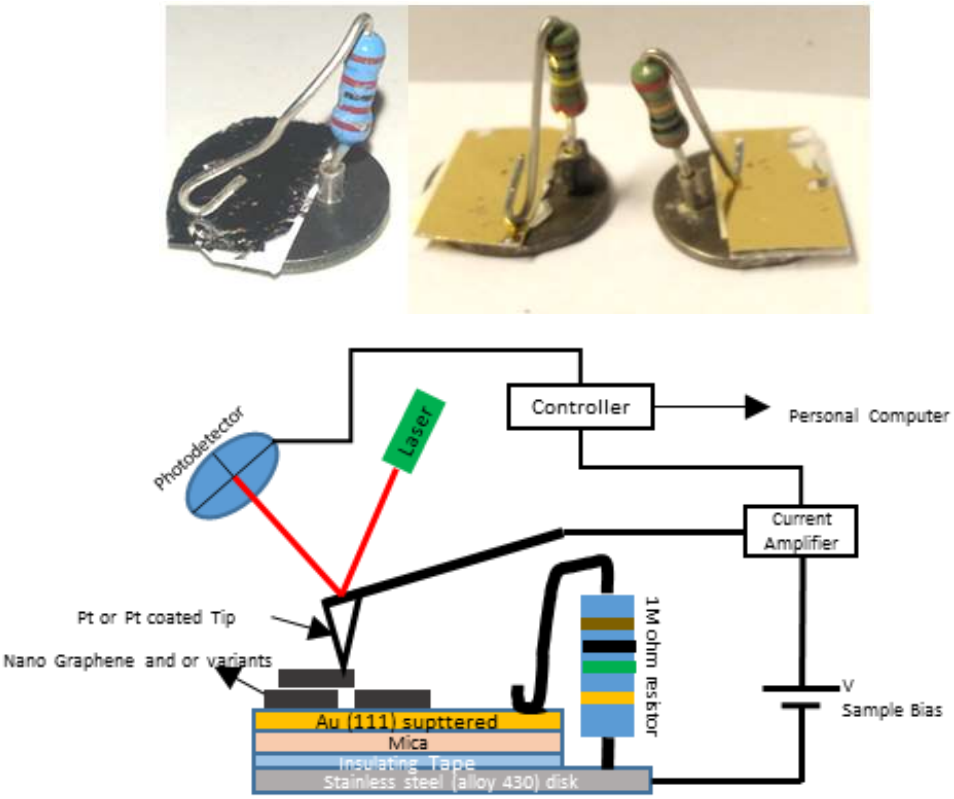

Figure 3.2, Sample setup with exchangeable control resistor in series. HOPG on the left and Au (111) on the right can be seen. nG, nGTrz and nGO were doposited on those substrates and measurements were carried out.

3.7. Scanning Force Microscope Imaging (SFM)

For observation of the 2DTSs structures, scanning force microscopy in Quantitative nanomechanical mapping (SFM-QNM) and ScanAsyst mode (SFM-ScanAsyst) were performed using a Multimode 8 with Nanoscope 4 controller. An E or J scanner with maximum scan size of 10 and 100 μm was used for scanning samples. For SFM-QNM measurements, both cantilevers with spring constants of 2 N/m (OLTESPA) and 0.4 N/m (ScanAsyst Air–HR) were used. The sensitivity of cantilevers was first calibrated by thermal tuning process. Then their spring constant was measured over Sapphire (Bruker) as a hard surface. The force applied to the samples by the tips was within the range of 100-2000 pN. Measurements were carried out in

512 in 512 pixels' resolution and speed of 6 - 15 minutes per image at room temperatures 25-27 ^{o}C and relative humidity 30 – 35%. SFM images were processed and analyzed with SPIP (Image Metrology A/S) software. Topography images were line flattened with first order polynomial.

3.8. SFM-QNM and SFM-QI Calibration Methodologies

Calibration process of the Scanning force microscopy for the quantitative nanomechanical mapping (QNM) and quantitative imaging modes (QI) are required for translation of the vertical deflection of cantilever into applied setpoint force during measurements. The calibration process commonly involves measurement of the sensitivity of the cantilever over a hard surface such as Sapphire or Muscovite Mica substrates. Depending on the sample to be measured softness, two methods of calibration could be carried out, Relative and absolute methods.

In "Relative calibration method", Cantilever bending sensitivity is measured at the interface of a stiff and undeformable interface. This is done in addition to "Thermal tuning" to obtain the spring constant of the cantilever and finally measuring elasticity of a known reference sample. For further accuracy of quantitative measurements finding out the SFM probe tip diameter is important that results in correct elasticity value for reference sample. Tip radius may change during the measurement of the reference sample and before measurement of the unknown sample.

In "Absolute calibration method", Thermal tuning of the of the cantilever is carried out initially to know the spring constant of it. In next step, using an SFM tip radius calibration sample that could be for example Gold nanoparticles of known diameter immobilized on a mica surface or sample with repetitive pattern of titanium micro pyramids. SFM tip broadening is calculated and diameter is found based on the observed measurements and the known sample particle diameters or the pyramid dimensions. Quantitative nanomechanical mapping of the unknown sample then could follow. In absolute calibration mode cantilever sensitivity measurement on hard substrate is carried out after measurement of the unknown sample and the experimental data are then adjusted to the later calibrated cantilever sensitivity. This is to avoid SFM tip deformation and diameter change before actual experiment.

3.9. Peak Force TUNA Measurements and Analysis

This section describes the sample measurements and analysis of the experiments in relation to the characterization of the nano graphene (nG), nano graphene oxides (nGO) and nano graphene sheets functionalized by Triazine groups (nGTrz) as described within the publication of Guday *et al.*[132]

In order to investigate the conductivity of the Nano graphene sheets, initially an overall scan of the sample topography at sample bias of zero volts and a setpoint force of 0.8 to 2 nN was carried out. The SFM tip was next contacted onto various nano graphene sheets in ramp mode for point measurements with different heights at setpoint forces of 15 to 300 nN while a sample bias was ramped. Local I – V curves were plotted for both Substrate and Nano Graphene or variants. Characterization of I – V data was preferred over the contact current images since the small normal forces (0.8 to 2nN) applied during the scanning was not enough to ensure a low noise contact current measurements on sample surface. Though our measurements were carried out in ambient conditions we could find highly reproducible I – V curves on both unmodified HOPG, air plasma modified HOPG and Nano graphene sheets (and Nano graphene oxides). We also found that the setpoint force applied by the tip can influence the contact current measured on nGs.

SFM-PFTUNA height images of the samples on a clean Au (111) surface show lateral dimensions between 50-200 nm for both nG and nGTrz, while nGO demonstrates smaller lateral sizes (30-100 nm). Furthermore, SFM-PFTUNA pull-off force images demonstrates contrast between the Au (111) and HOPG surface and locations at which the sheets are found. The pull-off force contrast is reproducibly lower on nG, nGTrz, and nGO in comparison to both Au (111) and HOPG substrates. However, it is possible to observe a reduction in the contrast values with time, attributed to tip contamination and degradation of the platinum coating in the case of conductive SFM tips. The contact current vs time (I-T) data demonstrates the maximum contact current at a constant bias between tip and sample. I-T measurements are carried out simultaneously during the force spectra measurements. Characterization of I-V and I-T data is simpler compared to contact current scanning images, as the small normal forces (0.8 to 2 nN) applied during the scanning and contact time

durations of (100 to 250 μs) are not sufficient to ensure low-noise contact current measurements on sample surface.

In addition, tip contamination during the scanning time with the small particles and resulting decrease in the overall conductivity of the tip, are found to be unavoidable. Our measurements are carried out in ambient conditions. However, we can find reproducible ohmic I-V curves on both Au (111), nG, nGTrz as well as nGO, due to the small sample bias and the control resistor connected in series with the sample. We also find that increasing setpoint force above 26 nN does not influence the contact current significantly, though the high forces increase the probability of the platinum coating wearing out and permanent conductivity loss of the tip.

The contact time needed to achieve maximum contact current between the tip and the sample differs for Au (111), nGTrz, nG, and nGO. In case of the nGTrz, the contact current vs time graph at constant bias demonstrates a flat plateau at a maximum current reached within the contact time. In contrast, for nG and nGO this flat plateau of current vs time is accompanied with a sudden rise in current just before reduction of the setpoint force between tip and subsequent separation of the tip from sample. The resistivity of the nanographene sheets are calculated per equation below:

$$R_t = R_{ns} + R_s + R_c \qquad \textit{Equation 20}$$

Where total resistivity (R_t) is the sum of substrate resistivity (R_s), resistivity of the connected control resistor (R_c), and the resistivity of the contacted nanosheet (R_{ns}). The slopes of the I-V curves from samples measured on clean Au (111) substrates are the inverse total resistivity ($1/R_t$) of those surfaces.

3.10. Photodynamic experiments of 2D Triazine Structures

The UV-Vis absorption spectroscopy measurements were performed for investigating the singlet oxygen release capability in case of the product of the

polymerization of the Triazine molecules in planar configuration known as 2D Triazine sheets (2DTSs). For this, initially, 2DTSs were dispersed in ethanol. A solution of 1,3 diphenylisobenzofuran (DPBF) (3.7×10^{-7} mol, 100 µg) was then prepared using ethanol (1 mL).

Synthesized 2DTSs as dispersed (100 µg/mL) in EtOH were exposed to 10 minutes of ultrasonication. Then, 900 µl of prepared DPBF solution in EtOH was mixed with 100 µl of 2DTSs from EtOH dispersion in a Quartz UV-Vis cell (HELLMA GmbH, Quarz Glass SUPRASIL 114-QS) with a path length of 10 mm.

Reference samples were prepared in Quartz cell containing only EtOH. Absorption spectra were measured with a double-beam UV–Vis spectrometer Shimadzu UV-2101PC. Samples were then exposed to a laser irradiation, while being stirred within the cuvette. A diode infrared laser with 808 nm wavelength and a power density of 0.5 W/cm2 was used. Interval times of laser exposures were as follow, 5, 10, 15, 20, 25, 30, 35, 40, 45, and 50 minutes. A UV-Vis absorption spectrum of 2DTSs was then measured in EtOH Figure 4.33.

3.11. Raman spectroscopy and Raman Mapping of 2D Triazine Structures

The description here is mainly the common sample and experimental preparations carried out for the Raman spectroscopy within this research. It is important to note that the following is based on the described experimental methods in the Faghani & Gholami *et al*. Publication.[133]

Samples were prepared by drop casting the ethanol dispersion of 2DTSs onto mica or Si wafer with SiO2 layer. Hundreds of 2DTSs sheets were measured using either mapping or individual points using a 100X objective NA = 0.9 (Mitutoyo, Olympus) at 532, 638, and 785 nm, with an Xplora one (Horiba) Raman spectrometer with $\sim$1.7cm^{-1} spectral resolution and power well lower than $\sim$ 1 mW. A grating of 1800 grooves/mm was used in the setup.

The instrument was calibrated using a Si spectral peak of a Si wafer in addition to the calibration against Neon lamp spectral lines. This was done to improve the spatial accuracy of the collected data for the range of the Raman bands of Carbon-

based structures. It is important to care specially to assure that the accumulation times and laser power used, improve the signal to noise ratio but do not adversely affect the carbon-based structures or 2DTSs sheets, i.e., preventing from thermally induced effects.[135] For Raman Mapping process, the 2DTSs dispersion from various solvents were deposited by drop casting onto the a TEM grid with . Often an area of 20 x 20 μm of the TEM grid was selected and the Raman mapping was carried out.

Chapter 4

4. Results

This chapter presents sets of results describing observations related to the thesis title. It is important to note that the discussion on the meaning and interpretations of these results is presented in the next chapter, "Discussion." Here, under the subheadings 4.1.1 to 4.2.2, are the results of experimental research conducted over several years, addressing various research questions. Results include information on the structure and topography of "Graft to" [32,97] and "Graft from" [130,131] functionalization methods for TRGO, "Graft to" interfacial interactions with viral particles, and "Graft from" functionalized 2D sheets' size dependency of interfacial viral interactions[130]. Additionally, the effect of functionalization in "Graft to" on the preservation of conjugation of carbon-based 2D sheets[132] was addressed. Furthermore, "Triazine" as a molecule capable of in-plane trimerization and further polymerization was investigated via scanning force microscopy and Raman spectroscopy. The results described here are also detailed in the publication by Faghani & Gholami *et al*. [133] The results presented in this chapter are based on the demonstrated outcomes in the referenced publications in each case.

4.1. Topography and interfacial activity of 2D carbon-based Structures

The rationale behind the experimental results described in this subsection is based on questions regarding the structural characteristics of controlled multivalent functionalized 2D graphene sheets. The key inquiries include whether covalent functionalization is successful and stable, if post-functionalization with hyperbranched polyglycerols (hPG) is possible and its topographical features dependency with the extend of post functionalization with hPG (low vs high content) and whether the functionalized interfaces can immobilize viral particles of VSV, what the average lateral sizes and typical topographical features of the "Graft from" functionalized sheets are. Answering these questions is essential for developing a topographical understanding of the novel methodology utilized in the functionalized 2D materials in both cases of "Graft to" and "Graft from" methods. The results are then presented in the order of

experimental progression as described in the previous chapter and based on the publications reference here after.

4.1.1. Topographical and Nanomechanical characteristics of the “Graft to” functionalized 2D carbon-based Nanosheets

The topography and structure of the functionalized TRGO sheets were systematically investigated using Scanning Force Microscopy (SFM) in Quantitative Nanomechanical Mapping mode (SFM-QNM) (2.13.3) and occasionally with Tapping mode. Employing these experimental methodologies, I determined the height at zero force and pull-off force (adhesion) of the TRGO-Trz structures using SFM-QNM and compared that information with post-functionalized TRGO after the covalent attachment of hyperbranched polyglycerols (hPG) onto the TRGO-Trz. This investigation was carried out comparatively for higher contents of hPG attached to Trz functional sites, based on two classifications of "hPGlow" and "hPGhigh."

Furthermore, the topography of post-functionalization with sulfated and non-sulfated hPG sites were investigated. Functionalized 2D sheets, as deposited onto freshly cleaved HOPG or mica surface in combination with viral envelopes, were also examined. Vesicular stomatitis virus (VSV) was chosen as a model system for biological interaction studies and the inhibitory potential of these 2D carbon-based materials. The results overall demonstrate that graphene sheets with a high density of sulfate groups efficiently bind to VSV particles, while their analogs with hydroxyl groups did not show significant affinity toward VSV at a comparable concentration level. This section's results and descriptions are published [32], and the written parts here are in accordance with that publication.

Figure 4.1 shows a high-resolution Tapping mode SFM height image of the TRGO sheets as deposited onto freshly cleaved mica interface in ambient conditions. Brighter regions correspond to higher topographical height and the cross-sectional line demonstrate the profile of the sample topography. Height profile crossing between single layer and double layer region shows a typical interlayer distance of ~0.6 nm for TRGO single layer in ambient conditions with 45% rH. TRGO is observed as plateaus with different steps and occasional wrinkles and folds.

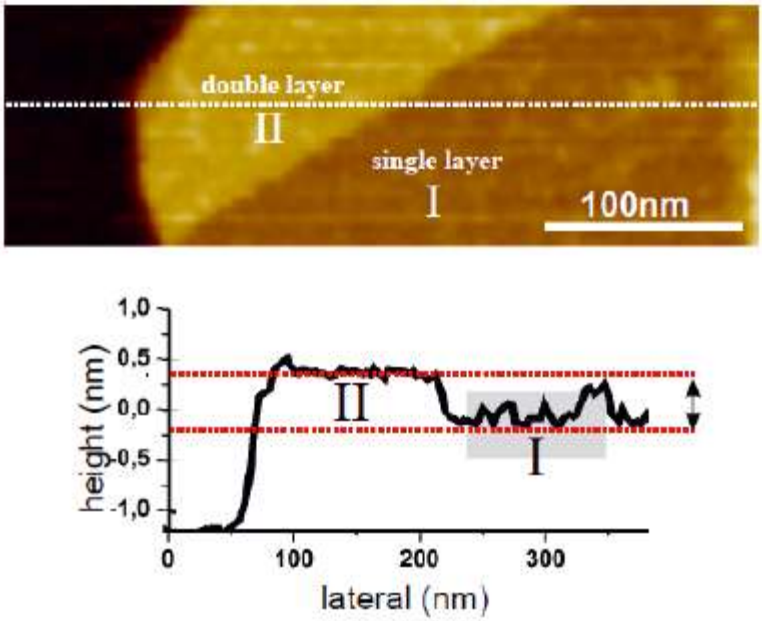

Figure 4.1, SFM-Tapping mode height image of TRGO deposited onto the freshly cleaved mica. Step height of single layer TRGO corresponds to 0.6 nm.

SFM-QNM height images of TRGO-Trz (Figure 4.2) deposited onto HOPG substrates show sheets with various heights in the range of 4–10 nm. These sheets exhibited occasional terrace steps with the smallest step height of 2.2 ± 0.5 nm with the error here and in the following being the standard deviation. [32] The TRGO thickness in this study was found to be 0.6 nm (Figure 4.1).

In further steps of post functionalized TRGO-Trz, naming is based on the mass contribution of the hPG content to the TRGO sheets, namely TRGO-hPGhigh and TRGO-hPGlow as also described in the chapter 2.

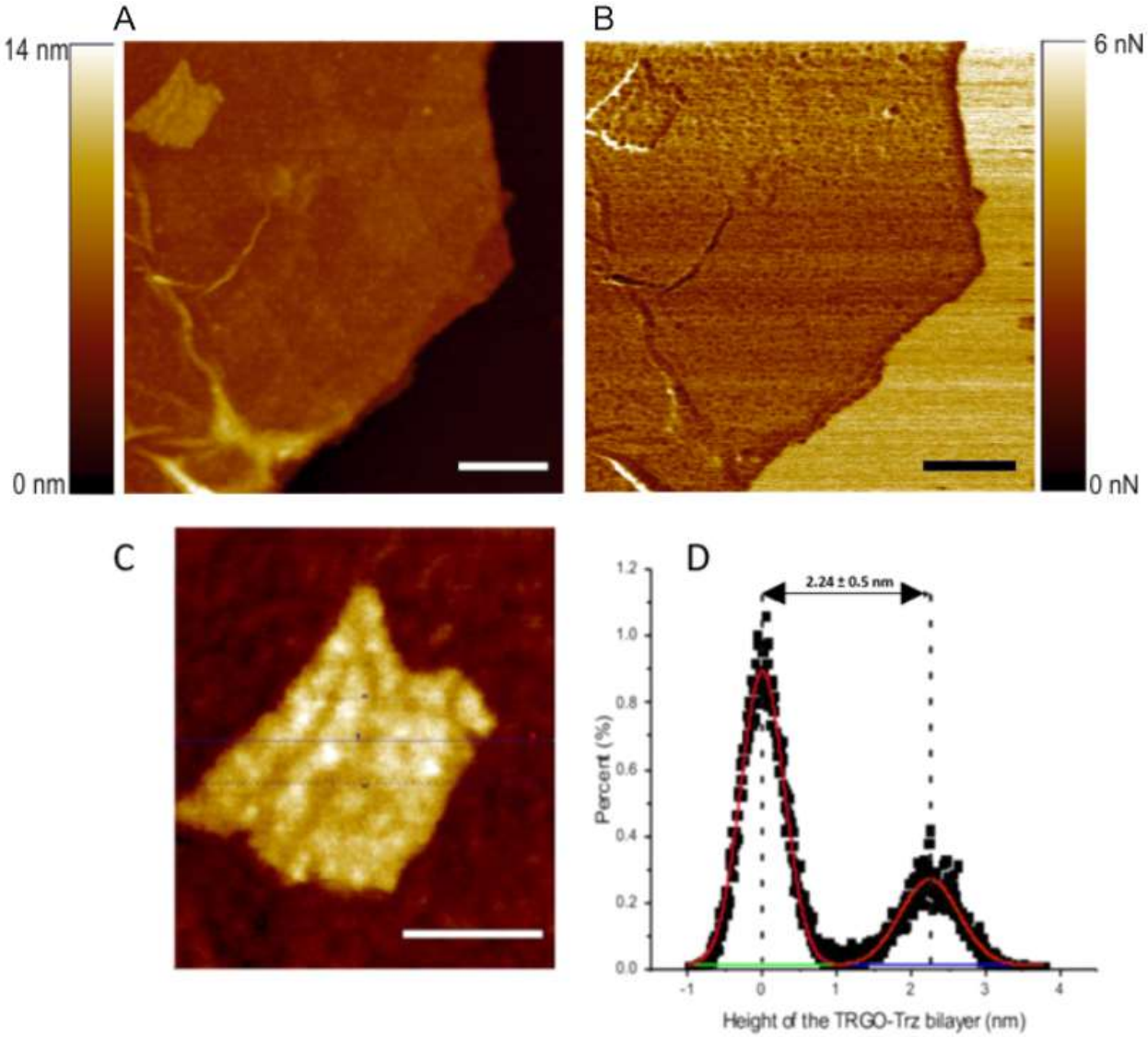

Figure 4.2, A) SFM-QNM height image of TRGO-Trz few layers at zero force height at HOPG interface. B) SFM-QNM Pull off force image of (A). Scale bar is 100 nm for (A and B). C) close up height image of the TRGO-Trz bilayer, scale bar is 50 nm. D) Height histogram of the bilayer TRGO-Trz. Adapted from reference [32].

TRGO-Trz sheets are later post functionalized by the “Graft to” methodology again to include hyperbranched polyglycerols of molecular weight of 6300 Daltons. These structures are then named as TRGO-Trz-hPG which then contain mainly –OH groups at the hyperbranched polyglycerols interface. The topography of such post functionalized 2D carbon-based sheet is shown in Figure 4.3.

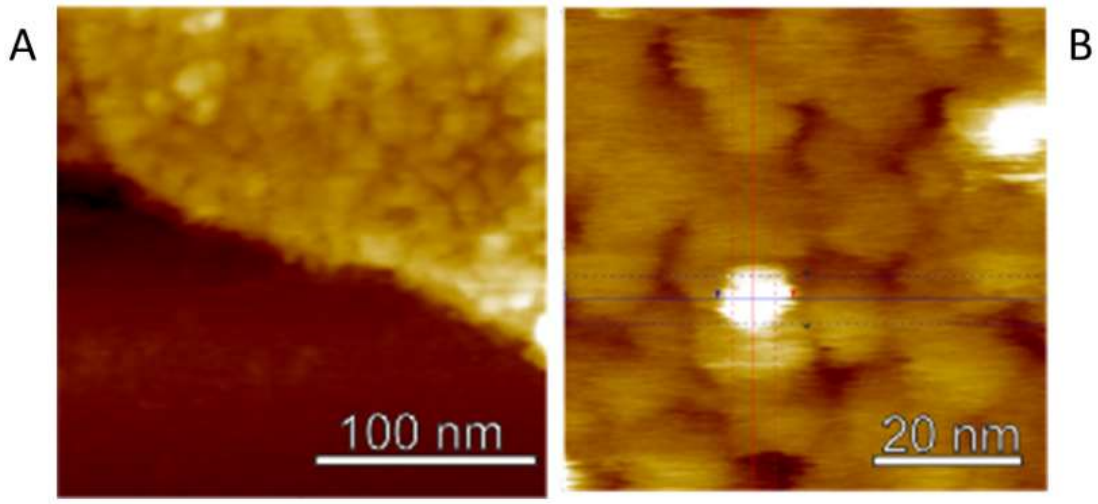

Figure 4.3, A) Typical High resolution SFM Tapping mode height image of the TRGO-Trz-hPG as deposited onto the freshly cleaved mica surface (Darker region in A). B) A typical close up view of the hyperbranched spherical polyglycerols attached covalently onto the TRGO-Trz interface.

SFM-QNM height images of TRGO-Trz-hPGlow (Figure 4.4A) revealed sheets of variable thickness with the height of the thinnest sheets being 8 ± 1 nm at the thickest sections. The surfaces of TRGO-Trz-hPGlow exhibit occasional depressions with depths of ~ 2.5 – 5 nm (Figure 4.4). SFM imaging of TRGO-Trz-hPGhigh (Figure 4.8Figure 4.5) displays sheets with a height of 8 ± 0.8 nm without detectable depressions but with wrinkles commonly observed also on non-functionalized TRGO-Trz and or TRGO or GO and even Graphene.

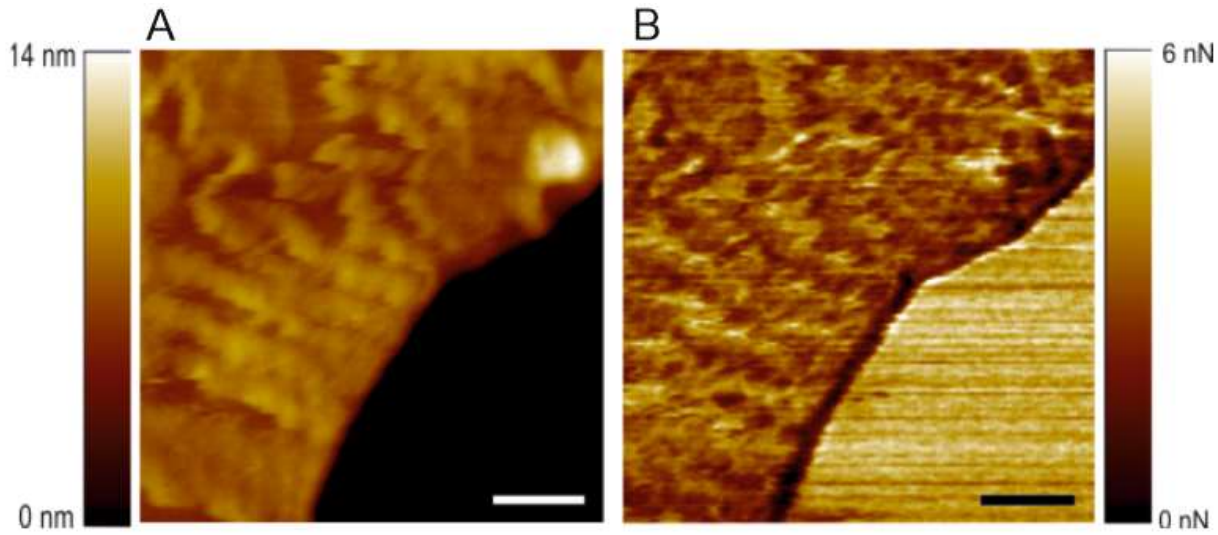

Figure 4.4, SFM-QNM height image of TRGO-Trz-hPGlow at (A) zero force. B) SFM-QNM pull-off force image of (A). Scale bars are 100 nm for all images. Adapted from reference [32].

SFM-QNM pull-off force (adhesion) images shows different contrast responses and provide information to differentiate between the interfaces independent of height variations (Figure 4.4b).

TRGO-hPGhigh sheets deposited onto the HOPG surface exhibited a homogeneous pull off force contrast different from the substrate specially for the wrinkles (Figure 4.5B). TRGO-Trz-hPGlow, however, showed less homogeneous height and Pull off force contrasts and it was possible to observe regions of higher height than the HOPG substrate but with similar pull off force contrast to HOPG surface (Figure 4.4)

The pull-off force contrast behavior turned out to be reproducible for fresh SFM tips. Contrast levels occasionally decayed with time as seen in the pull-off force images and some scan lines This artefact is attributed to tip contamination during scanning by free matter at the sample interface. This temporary contamination of the tip was observed to disappear within the surface scan time occasionally.

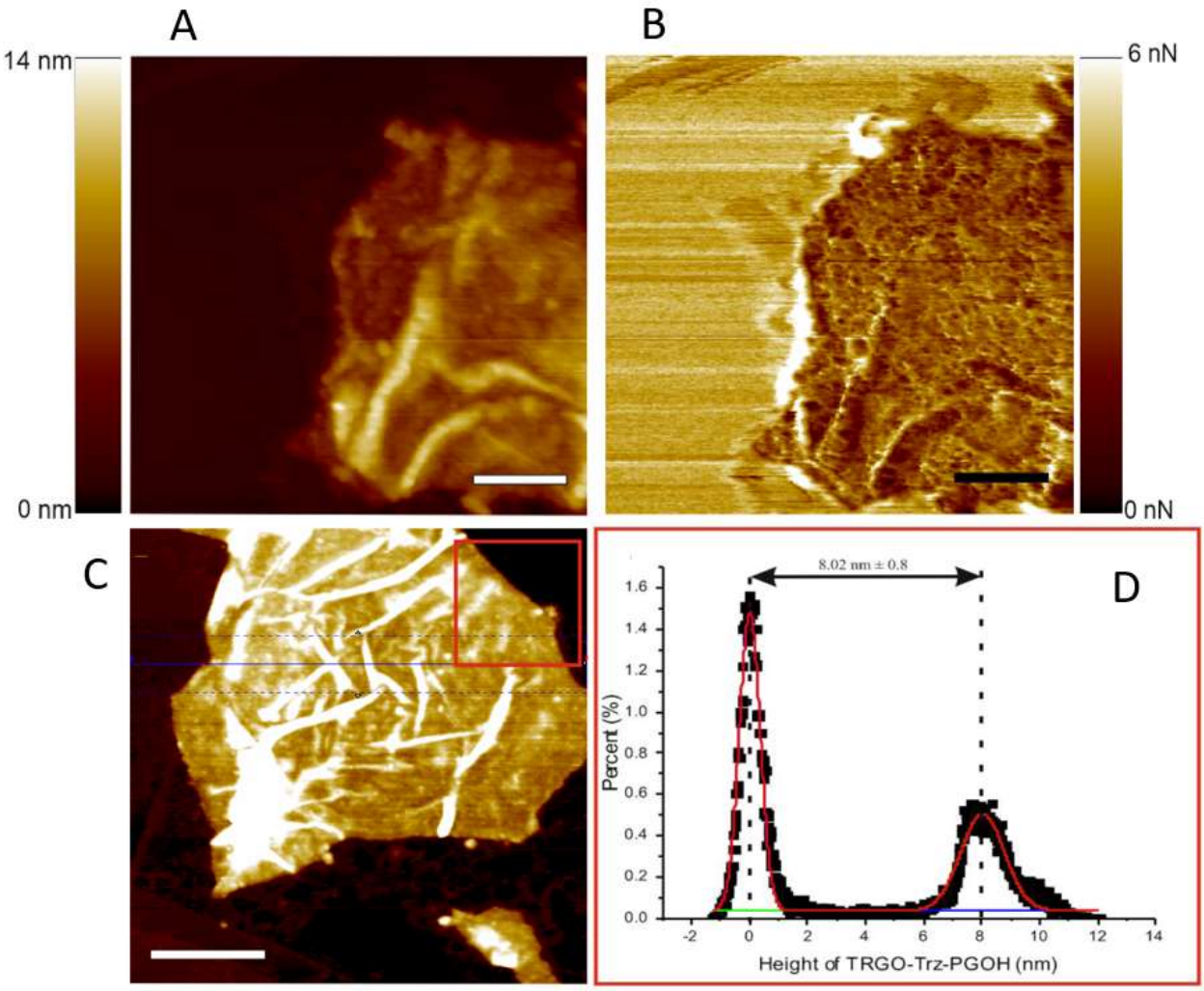

Figure 4.5, A) SFM-QNM height at zero force of TRGO-Trz-hPGhighand B) pull-off force images of TRGO-Trz-hPGhigh. C) Single layer TRGO-Trz-hPGhigh. D) Thickness Histogram. Scale bars are 100 nm for all images. Adapted from reference [32].

SFM-QNM also provides the deformation mapping of the sample interfaces. As it can be seen in Figure 4.6, pull off force or tip-sample adhesion force data demonstrates a lower adhesion force in circular regions tightly packed within the area of the functionalized TRGO surface. Those circular regions with lower pull off force also demonstrate a higher relative deformation. Additionally, Figure 4.6 demonstrates different high and low variants of TRGO-Trz-hPG. The density of observed deformable circular regions with relatively lower pull off forces varies between TRGO-Trz-hPGhigh and TRGO-Trz-hPGlow variant. Furthermore Figure 4.7 and Figure 4.8 demonstrate a quantitative data set of deformation and pull off force of the hPG units distributed over

TRGO-Trz interfaces. Mostly less deforming regions correspond with higher topographical structure and higher pull off force with the SFM tip.

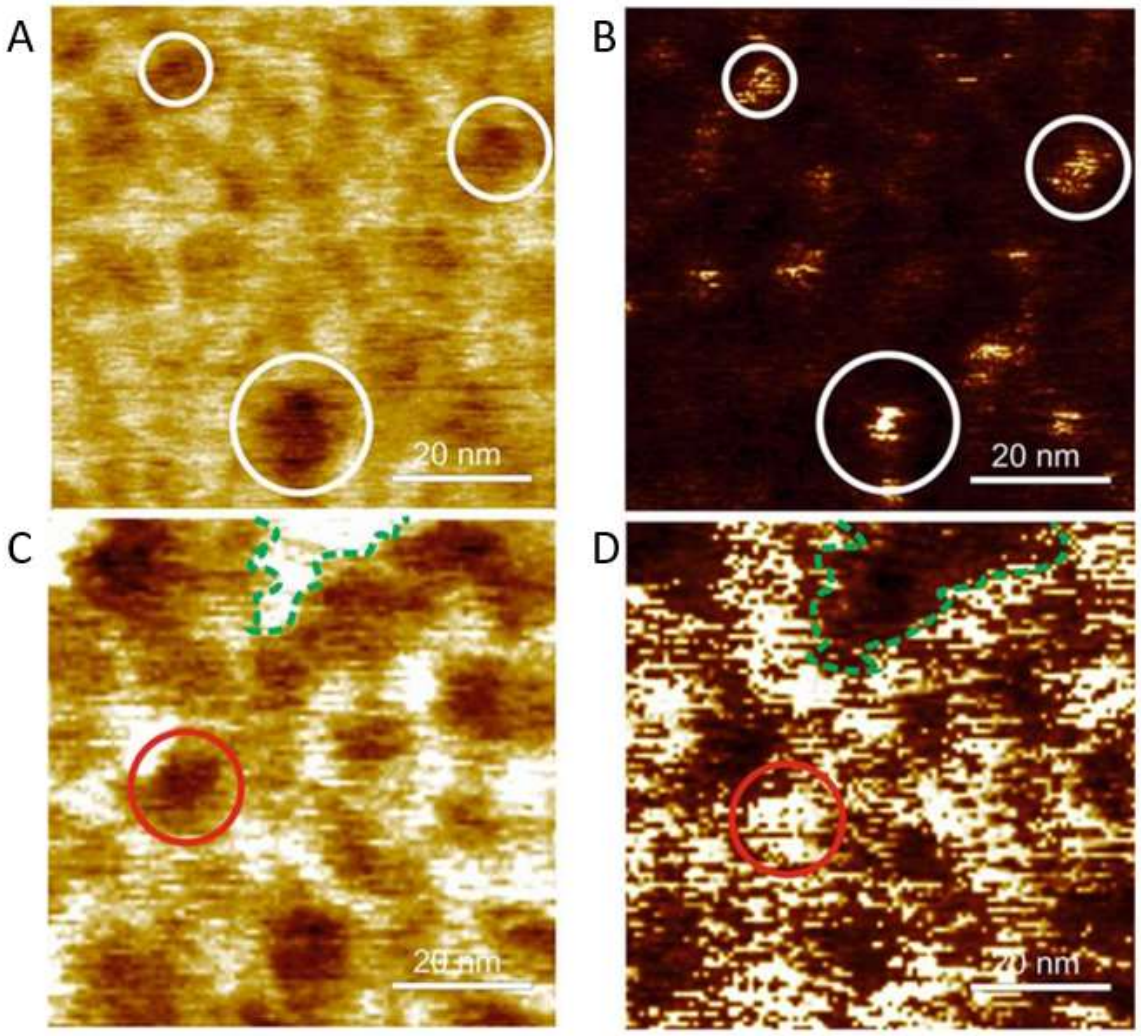

Figure 4.6, Deformation and pull off force images of TRGO-Trz-hPGlow A) SFM-QNM pull off force image of TRGO-Trz-hPGlow . B) Deformation image of the TRGO-Trz-hPGlow from the same area as the (A), white circles show hyperbrach polyglycerol (hPG) locations in (A, B). C) SFM-QNM pull off force image of TRGO-Trz-hPGhigh. D) Deformation image ofthe TRGO-Trz-hPGhigh from the same area as the (C), red circle shows hyperbrach polyglycerol hPG location in (C and D), green dotted line shows the proximity with higher adhesion in (C) and lowest deformation in (D) low deformation is attributed to the higher TRGO hardness in compare to hPG. Scale for A, B, C and D is 20 nm. Adapted from reference [97].

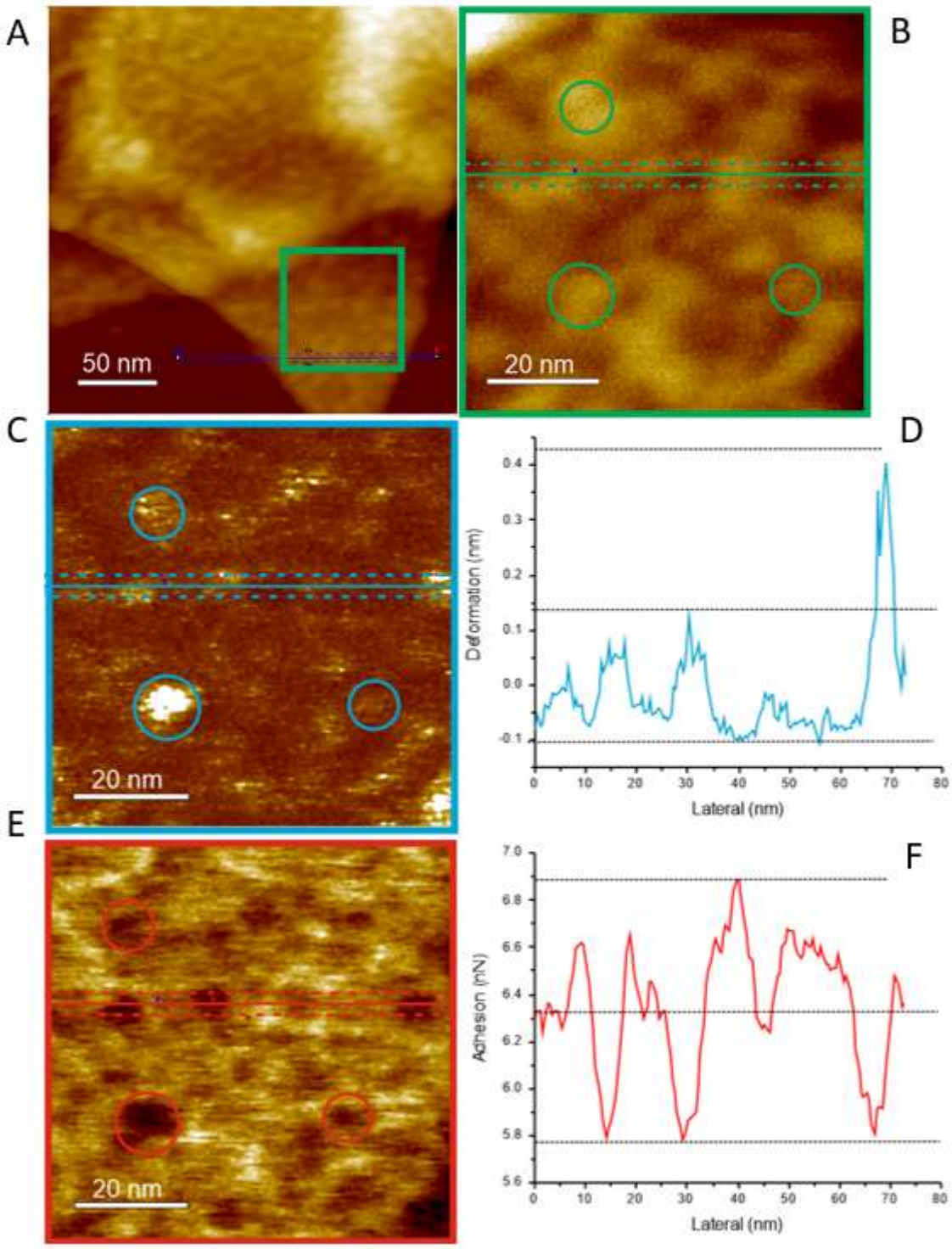

Figure 4.7, A) SFM-QNM height image of the TRGO-Trz-hPGlow. B) inset area from (A). C) Deformation data corresponding to inset data in (B). D) Deformation data from the line cross section in (C). E) Pull off force data corresponding to inset data in (B). F) Pull off force data from the line cross section in (E).

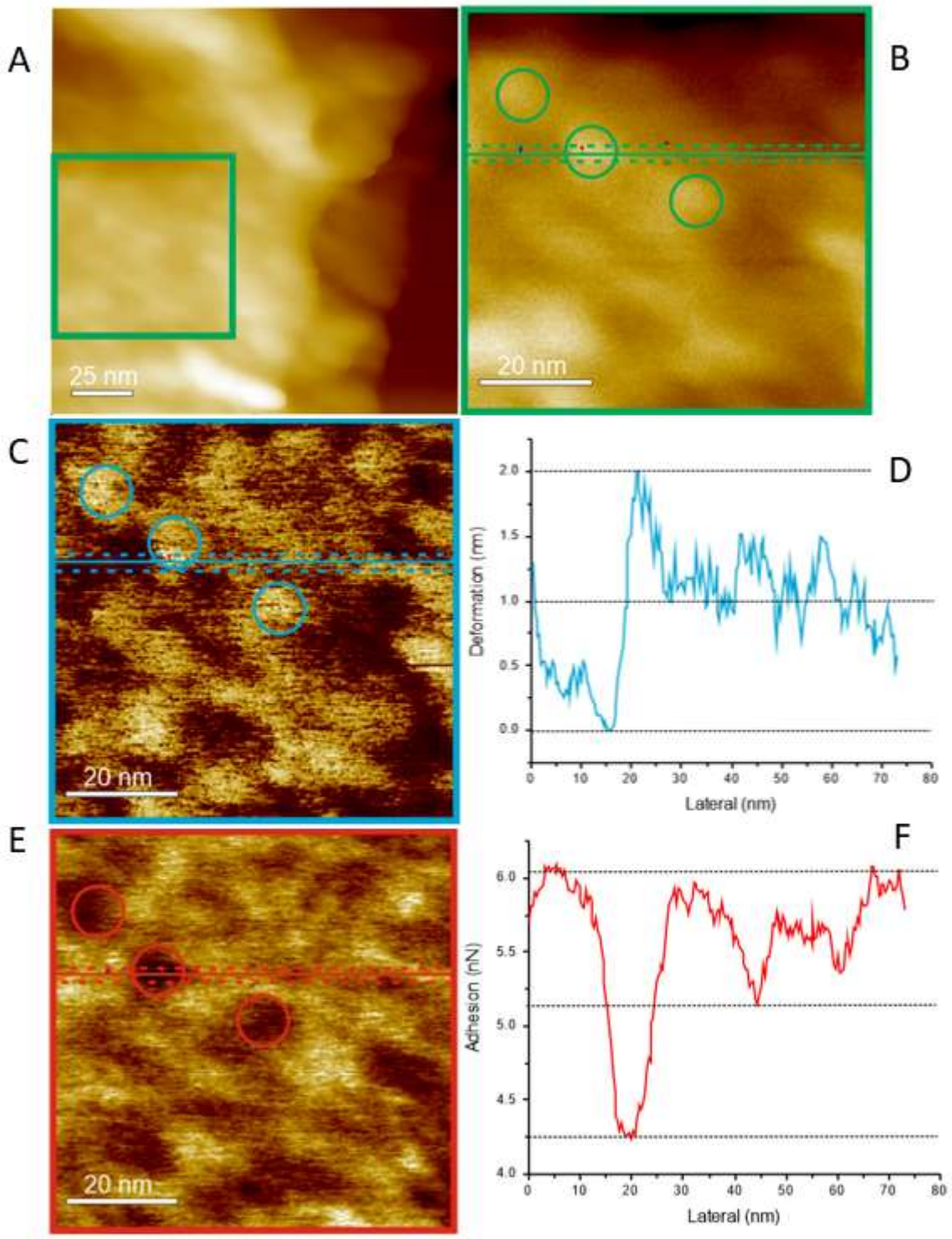

Figure 4.8, A) SFM-QNM height image of the TRGO-Trz-hPGhigh. B) inset area from (A). C) Deformation data corresponding to inset data in (B). D) Deformation data from the line cross section in (C). E) Pull off force data corresponding to inset data in (B). F) Pull off force data from the line cross section in (E).

Figure 4.9, demonstrates the topographical difference between the two species of TRGO-Trz-hPG with low and High hPG contents after the sulfation process. As it can be seen, the topography of the TRGO-Trz-hPG low or high variant is not drastically changed by the post functionalization sulfation process in compare to original TRGO-Trz-hPG variants. Height and Pull off force data from SFM-QNM shows occasional depressions and inconsistencies of coverage for low hPG content TRGO-Trz-hPG variants. The depressions observed are topographically similar to the observation that was made in Figure 4.4.

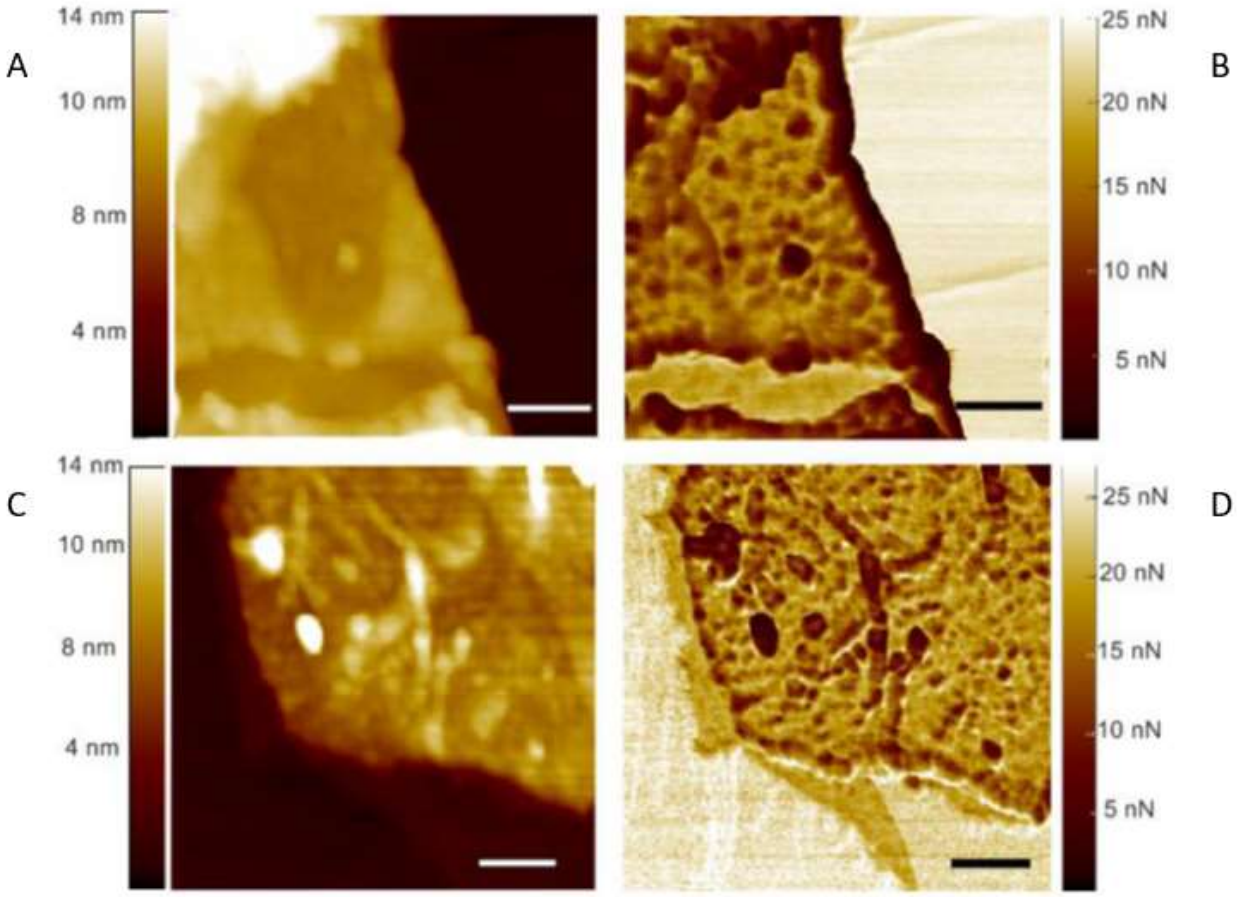

Figure 4.9, Sulfated version with low polymer content A) SFM-QNM height image at zero force of TRGO-Trz-hPGS Low, B) TRGO-Trz-hPGSLow Pull off force image of same area as (A). C) SFM-QNM height image at zero force of TRGO-Trz-hPGShigh. C) SFM-QNM Pull off force image of same area as (C). Scale bar in all images are 100 nm. Substrate is freshly cleaved HOPG interface. Adapted from reference [32].

Figure 4.10, demonstrates a typical topography and height distribution of a TRGO-Trz-hPGShigh sheet that is a high hPG content with sulfation post modifications. A typical height value 7.9 ± 0.7 nm. This value demonstrates a very

close value to that of original TRGO-Trz-hPGhigh without any sulfation. As it can be observed, similarity of homogenous coverage of the TRGO-Trz interface with hPG units exist for both variants of non-sulfated and sulfated hPG.

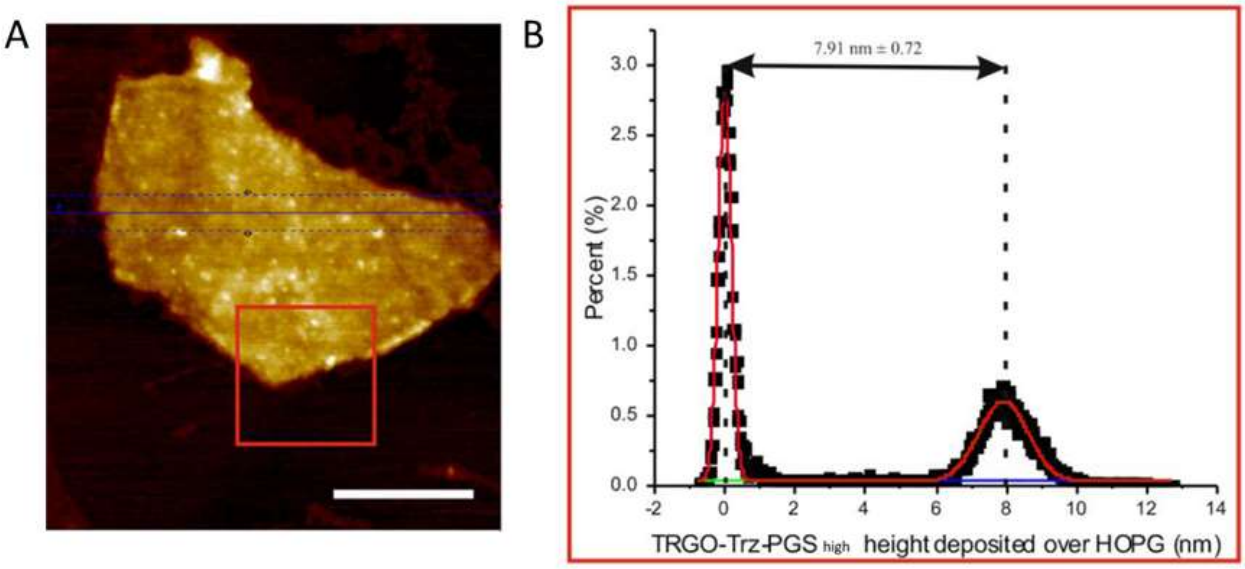

Figure 4.10, Thickness of sulfated high polymer content TRGO-Trz-hPGShigh. A) SFM-QNM height image at zero force of TRGO-Trz-hPGS high that is a sulfated variant as deposited onto freshly cleaved HOPG surface. Scale bar is 250 nm. B) Height histogram of (A) fitted with Gaussian functions shown in red. The difference between mean values of the two Gaussian functions is assigned the height of TRGO-Trz-hPGS high. Adapted from reference [32]

4.1.2. Interfacial activity and viral inhibition of the “Graft to” Functionalized 2D carbon-based Nanosheets

Further to investigate the existence of any multivalent interaction between the TRGO-Trz-hPG with model viral particles of VSV, SFM and Cryo-TEM instrumentations were utilized. The VSV particles were initially prepared by the virologists by exposure to UV light. As a consequence deactivation of the DNA and

RNA content within the viral envelope takes place.[136] In this process, viral envelope remains intact while the viral particle becomes harmless.

Later VSV were incubated at the interface of functionalized 2D TRGO sheets previously deposited onto inert freshly cleaved HOPG surface (explained in section 3.1). After incubation of VSV and functionalized TRGO sheets at predefined durations, the excess viral particle solution was spun off from the sample interface and SFM measurement were carried out in ambient conditions with 35-45% rH. Figure 4.11, demonstrates a typical VSV particle observed using SFM-QNM. The average length of VSV particles on TRGO-Trz-hPGShigh surfaces was 134 ± 29 nm (mean +/− standard deviation).[32] The length of the longest VSV particles on TRGO-Trz-hPGShigh was roughly 180 nm with a height of 20 ± 3 nm and a width of 60 ± 5 nm. The latter values were again in agreement with our cryo-TEM (Figure 4.11 D) and other data that revealed a length of 196 ± 8 and a diameter of 70 nm for VSV, respectively. [80]

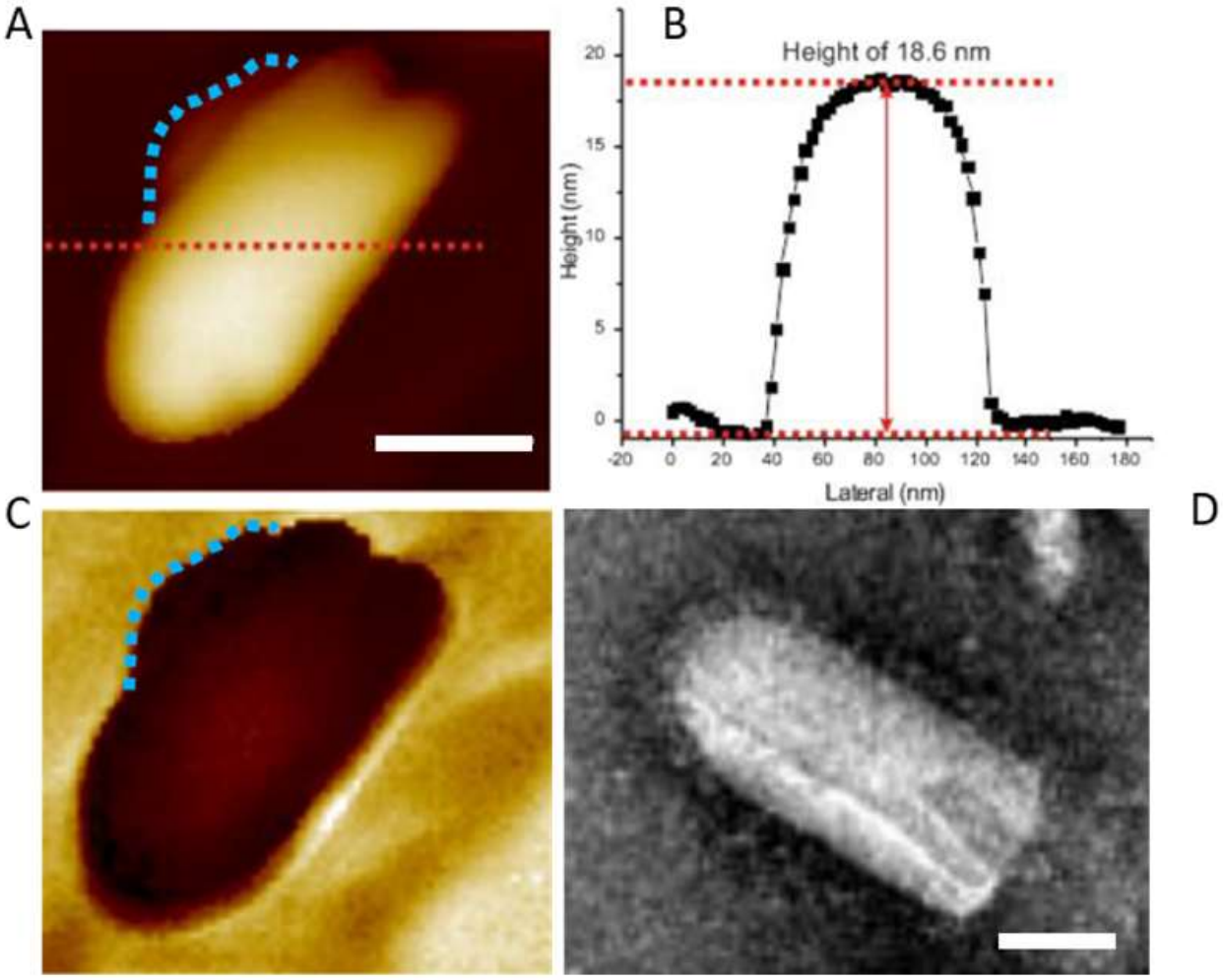

Figure 4.11, SFM observation of VSV viral particle. A) SFM-QNM height image of VSV found over TRGO-Trz-hPGhigh, Scale bar is 50 nm. The red dotted line shows the line profile

shown in the (B) blue dotted line in (A and C), which shows the edge of a deformed section of the virus's outer membrane. B) The cross section reveals VSV height of 18.6 nm and width of 58-60 nm. C) Pull off force image acquired simultaneously with (A). D) Negative stain TEM (1% PTA, pH 7.4) image of VSV. Scale bar is 50 nm. Adapted from reference [32]

Figure 4.12 & Figure 4.13, demonstrates SFM Tapping mode height images of the sulfated and non-sulfated variants of TRGO-TRZ-hPGhigh deposited onto after incubation with VSV viral particles. As it can be seen, the sulfated version of the functionalized TRGO demonstrates particles with length more than 100 nm or around 65 nm (red dotted) being immobilized onto it while none observed over HOPG surface and non-sulfated TRGO-Trz-hPGhigh.

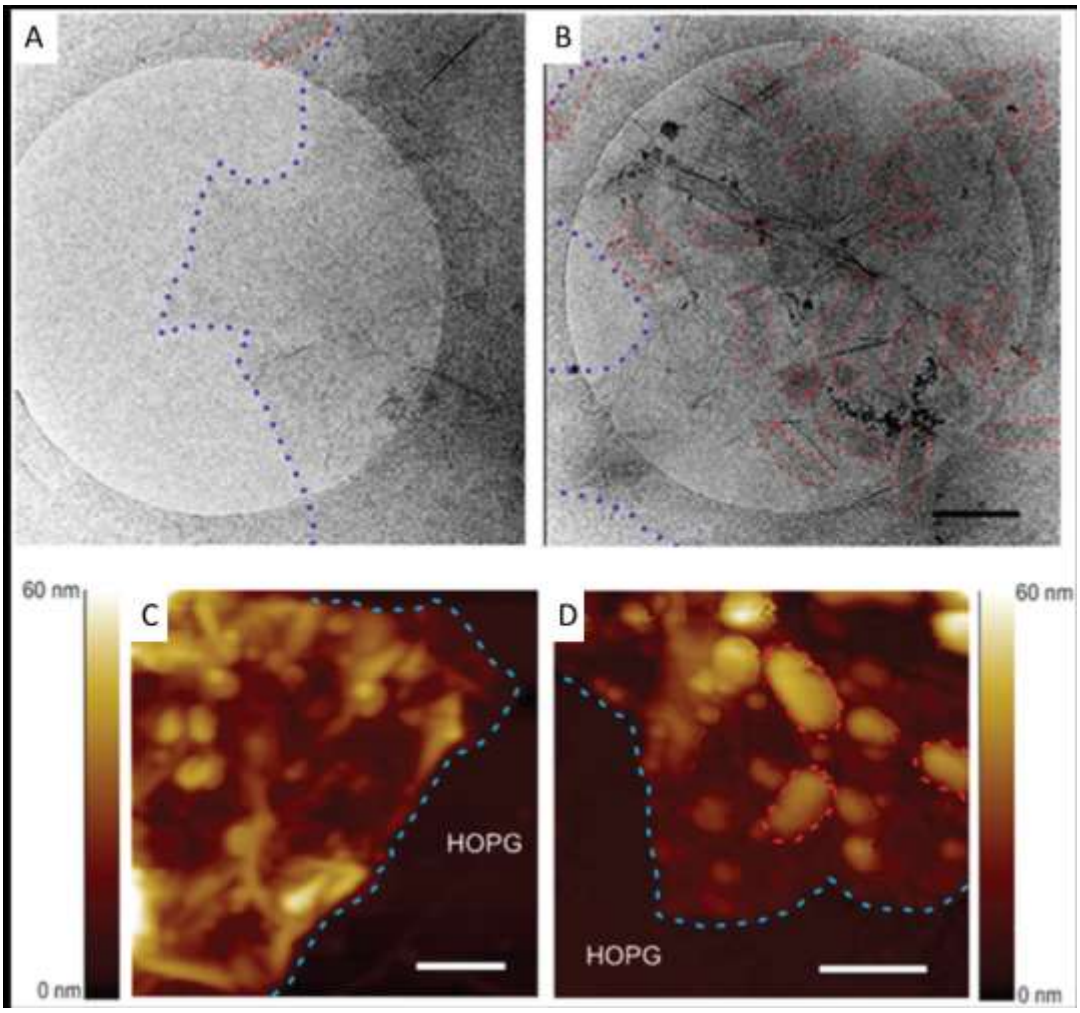

Figure 4.12, Cryo-TEM & SFM images of A) TRGO-PGhigh and B) TRGO-PGShigh, each incubated with VSV. Tapping mode SFM height images of C) TRGO-PGhigh and (D) TRGO-PGShigh, each incubated with VSV. Virus particles are outlined by red dashed contours; edges of the graphene sheets are marked by blue dashed contours. The scale bar is 200 nm in all images. Adapted from reference [32].

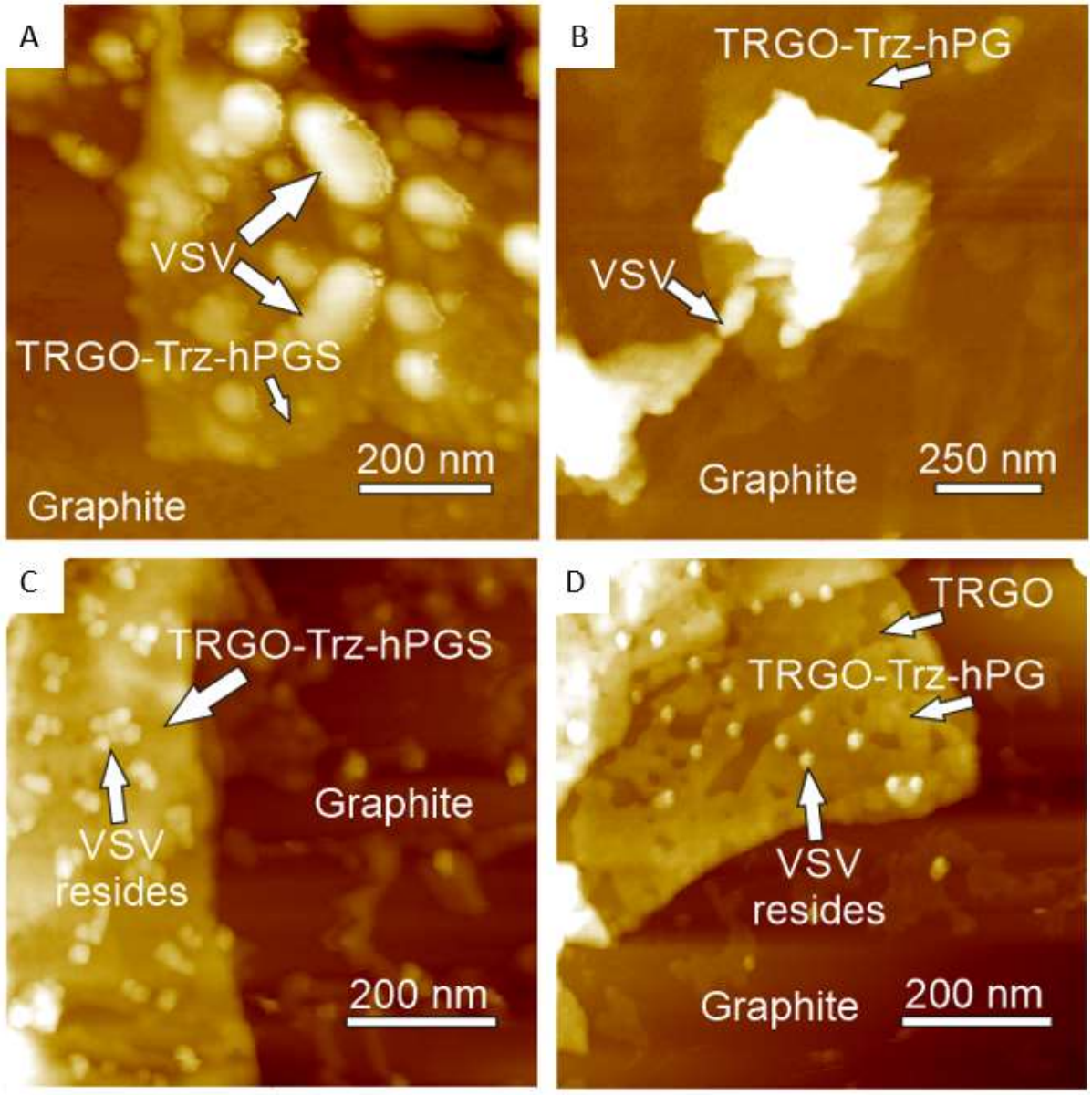

Figure 4.13, Interaction of VSV with low and high hPG content 2D sheets. A) SFM height image of high polymer content and sulfated functionalized 2D sheet anchoring VSV intact and pieces. B) SFM height image of high polymer content and Non-sulfated functionalized 2D sheet anchoring VSV intact and pieces. C) SFM height image of low polymer content and sulfated functionalized 2D sheet anchoring VSV pieces. D) SFM height image of low polymer content and Non-sulfated functionalized 2D sheet anchoring VSV pieces.

Figure 4.14, shows dependence of surface density of VSV pieces attached to sheets on the incubation time. As it can be observed, the two variants of sulphated and non-sulfated versions of hPG demonstrated different extent of immobilization of the viral particles and pieces. Here, the immobilization of the viral particle from its free state

within the solvent is considered to be associated with the viral inhibition of those functionalized interfaces. The surface density was estimated by counting VSV pieces found in SFM-QNM height images within area of 400 x 400 nm. Surface density of VSV was reproducibly higher on TRGO-Trz-hPGS sheets compared to TRGO-Trz-hPG.

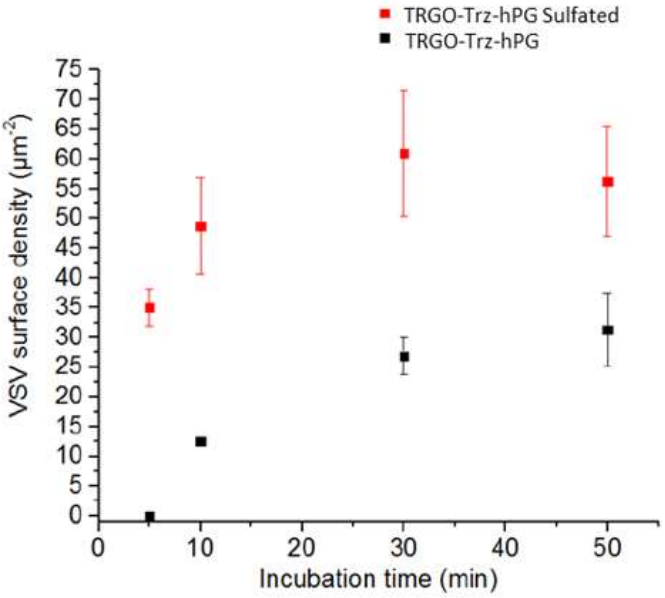

Figure 4.14, Dependence of the densities of VSV pieces attached to TRGO-Trz-hPGS (red squares) and TRGO-Trz-hPG (black squares) upon incubation time. The errors bars are standard deviations. Adapted from reference [32].

Figure 4.15, shows a histogram of the length of long axes of "Vesicular stomatitis virus" or VSV particles counted and found to be immobilized over the 2D functionalized TRGO sheets with high density of sulfated hyperbranched polyglycerols post functionalization that are known as "TRGO-Trz-hPGShigh". The long axes are shorter than the length of the virus in solution (200 nm according to Cryo-TEM), and the distribution is broad. Gaussian fitting is used to demonstrate the normal distribution values of each population distribution for the dimensions of the viral particles found immobilized on the functionalized TRGO-Trz 2D sheets. As found and described in the publication by Gholami *et al*, the distribution of long axes can be well-fitted by three Gaussians, describing three populations of the virus particles found immobilized at the interface of the functionalized 2D sheets. The longest particles found were measuring around 140 nm. Considering tip broadening estimated at 8.44 nm within these experimental results, the real length of the longer particles is estimated to be around 132 nm.[32] The three found populations of the viral particles imply that the viral envelope

may have been broken down during the sample preparation or already within the virus-buffer solution. shorter particles are likely VSV pieces as well, as they have also been observed via Cryo-TEM measurements.

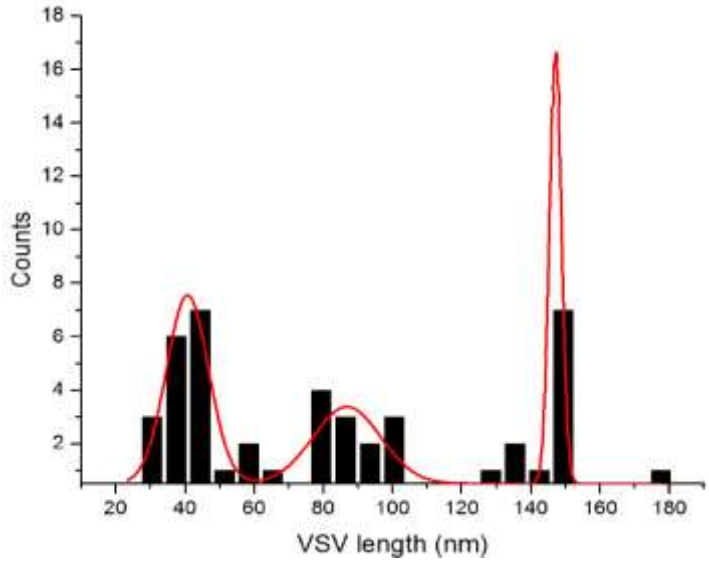

Figure 4.15, Histogram of lengths of the long axes of VSV anchored onto TRGO-Trz-hPGS as imaged by SFM- QNM. The red line is the fit of the histogram with three Gaussian functions. Adapted from reference [32].

Figure 4.16, demonstrates the time-dependent structural variation between VSV particles attached to TRGO-Trz-hPGhigh and TRGO-Trz-hPGShigh. The figure illustrates the effect of sulfation of the functionalized 2D sheets on the integrity of the VSV particles attached to them. By evaluating consecutively recorded SFM-QNM datasets of VSV particles found over TRGO-Trz-hPGhigh, it was possible to observe subsequent deterioration of the virus structure (Figure 4.16A, B). Surveying regions of the sample not yet scanned by the SFM probe showed that VSV particles in those areas remained unaffected (Figure 4.16C, D).

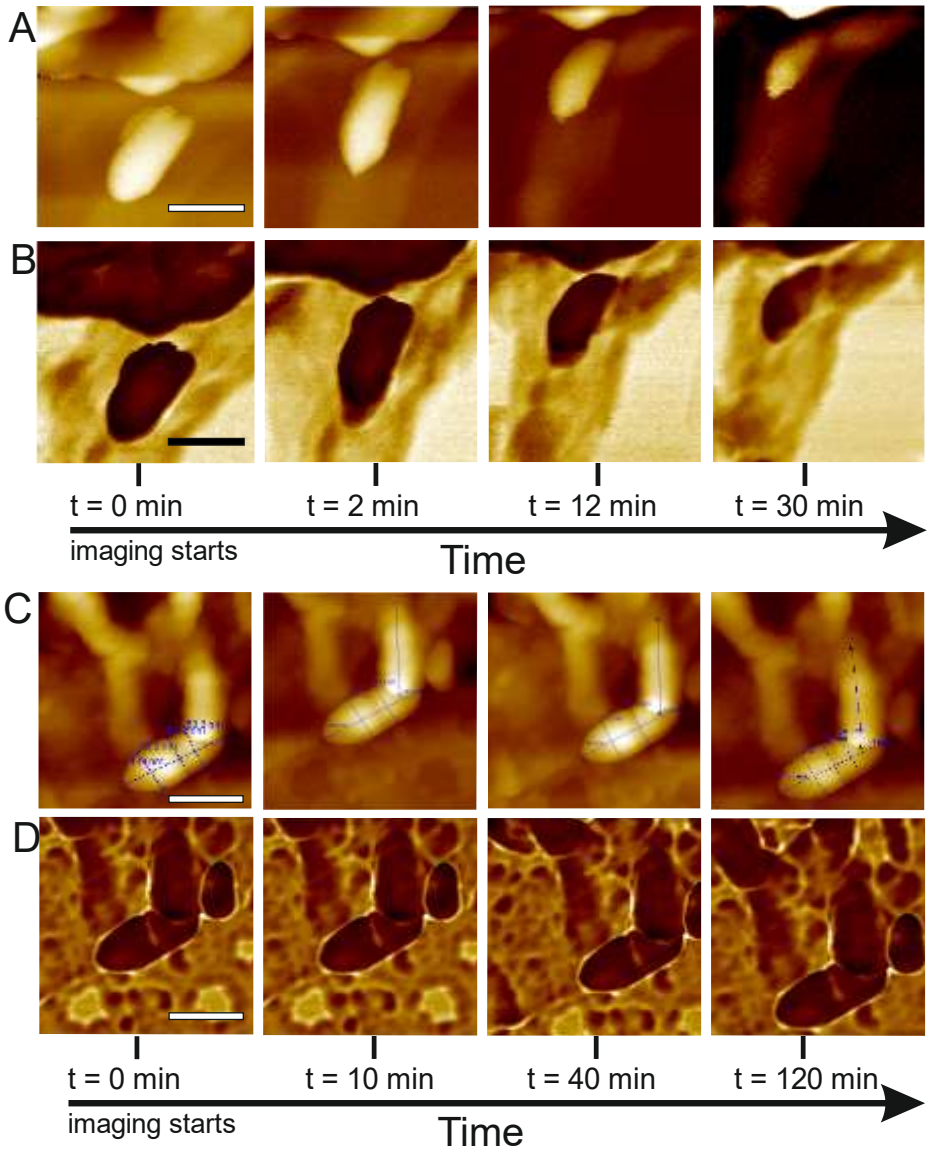

Figure 4.16, Structural changes of VSV over functionalized 2D sheets. SFM-QNM height images of VSV trapped over TRGO-Trz-hPGhigh with B) the corresponding pull-off force images. C) SFM-QNM height images of VSV trapped on TRGO-Trz-hPGShigh sheets with D) the corresponding pull-off force images. In rows (B) and (D), darker regions demonstrate that the pull off forces between the tip and the VSV were lower. Brightest regions in the pull-off force images correspond to the HOPG. All scale bars correspond to 100 nm. Adapted from reference [32].

4.1.3. Size dependency of interfacial activity for “Graft from” Functionalized 2D Nanosheets for Inhibition of viral Particles

[2+1] nitrene cycloaddition reaction “Graft to” method of functionalization of TRGO perpendicular to its basal plane has been explored in the previous subsection 4.1.1. Here I will demonstrate characterization results of the “Graft from” synthesis approach. This section is in accordance with the collaborative publication of Ziem & Gholami *et al* [130,131].

The "graft to" method enhances the solubility of thermally reduced graphene oxide and provides a suitable 2D surface for multivalent ligand presentation. In this case, dendritic polyglycerols (dPG) were polymerized at the hydroxyl-containing functional sites of TRGO Nanosheets. Later, polysulfation of these dendritic polyglycerols was used to mimic the heparan sulfate-containing surface of cells and to compete with the natural binding sites of viruses. This goal is similar to previously demonstrated results, with the main difference being the structural variation in the method of functionalization, based on ring-opening polymerization rather than the utilization of Triazine molecules.

Considering the limitations of ring-opening polymerizations, the density and controlled functionalization are only possible based on the percentage of remaining functional groups after the thermal reduction of graphene oxide. The percentage of conversion of those oxygen-containing groups by the polymerization reaction affects the final product. In correlation with the degree of sulfation and the grafted polymer density, the interaction efficiency of these systems can vary.[131] This thesis investigates the functionalization topography to answer the question of whether the "graft from" functionalization has been successfully done and is covalent. Additionally, the results of this studies were published [92,130] and written parts here are in accordance with those publications.

Figure 4.17, shows the Typical SFM topography of the Functionalized TRGO via “Graft from” methodology at the freshly cleaved mica interface in ambient conditions (35 - 45% rH). Tapping mode SFM height images were used for quick revelation of the topography, and SFM –QNM was used for further studies. The nomenclature used for the “Graft from” synthesized functionalized TRGO is based on the nanomaterial name followed by the dendritic polyglycerol’s acronym “TRGO – dPG” for unsulfated and “TRGO – dPGS” for sulfated derivatives.

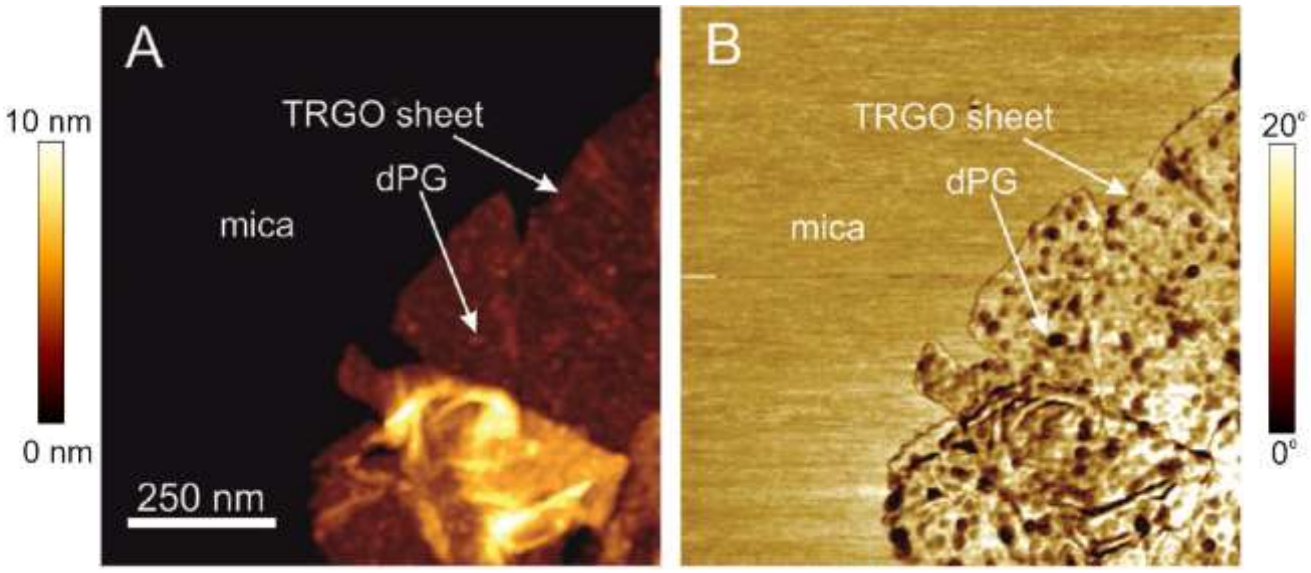

Figure 4.17, A) Typical SFM Tapping mode height image of the TRGO-dPG deposited onto freshly cleaved mica surface from water dispersion. B) SFM Tapping Mode Phase image of the same area as in (A). Adapted from reference [131]

In Figure 4.17A, the 2D TRGO sheets can be seen as plateaus with higher false color brightness over the freshly cleaved mica interface. Additionally, there exist spherical objects with bump-like higher topography, which also demonstrate a lower oscillation phase variation with the SFM probe tip in Tapping mode. This lower phase of oscillation compared to other regions of the scanned interface of the sample would mean variation of chemical structure. Those spherical objects are only present at the interface of the functionalized TRGO sheets and cannot be seen or found over freshly cleaved mica.

Figure 4.18 demonstrates the typical thickness distribution and histogram of the TRGO-dPG Nanosheets with their Gaussian distribution or normal distributions, as deposited from the water dispersion onto the freshly cleaved mica interface at ambient conditions (30-45% rH). The distributions of the height in Figure 4.18A clearly demonstrate two populations of pixel heights for Mica substrate and 2D functionalized sheets deposited onto it. Additionally, the lateral dimensions of the functionalized 2D TRGO-dPG sheets were measured based on the SFM tapping mode height images. It was observed that the lateral dimensions of the 2D Nanosheets could be classified into three groups of small (300-400 nm), medium (500-600 nm), and large (800-900 nm) based on their longest axis length and the normal distributions found after fitting the

lateral size data with Gaussian fits. Even after the sulfation process, lateral dimensions of the sheets remained with similar variations. Table 4.1 demonstrates the lateral dimension classification of sulfated TRGO-dPG sheets based on the normal distribution of the most frequent sizes found.

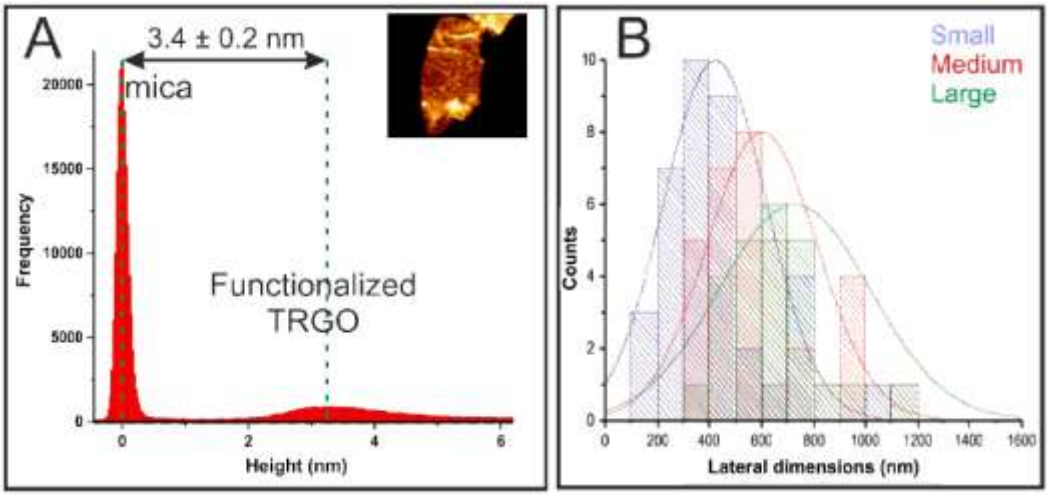

Figure 4.18, A) Histogram analysis of the height of a typical single layer TRGO-dPG sheet shown as inset when deposited from solution onto a freshly cleaved mica surface fitted with two Gaussian functions shown in red. B) Histogram analysis of the lateral dimensions of the TRGO-dPG sheets of three main variations of small, medium and large. Individual data sets are fitted with a Gaussian function shown in purple, red and green, based on the Feret's diameter of the irregularly shaped 2D sheets of TRGO-dPG. Adapted from reference [130]

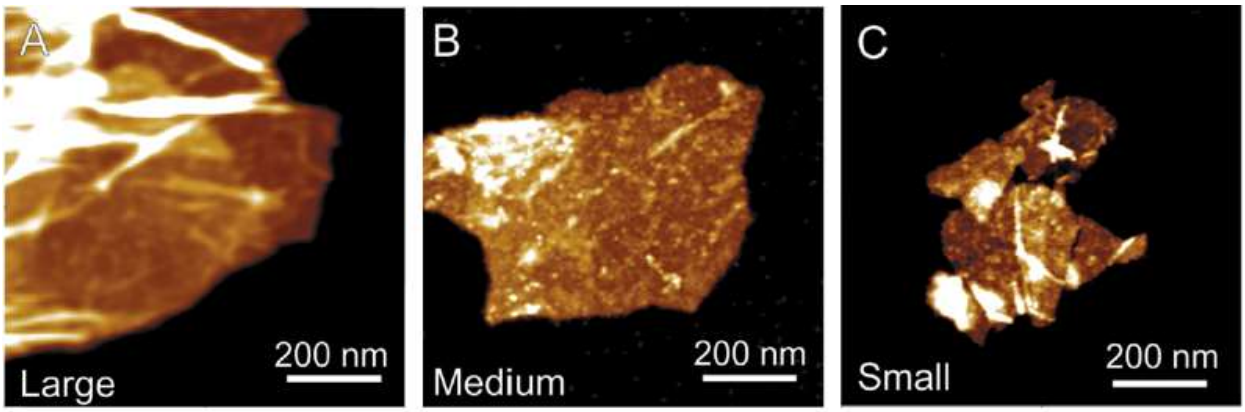

Figure 4.19, Typical lateral size variations of TRGO-dPG sheets deposited onto the freshly cleaved mica surface: (A–C) SFM-Tapping mode height images (typical height 3.5–4.0 nm as seen in Figure 4.18) of the different TRGO-dPGS sheet sizes showing the polyglycerol functionalization as spherical objects attached to the TRGO sheet. Adapted from reference[130]

Table 4.1, Table of the mean diameters and surface area of the surveyed TRGO-dPGS sheets (the total number of counted sheets were 97). Adapted from reference [130]

Mean Sheet diameter (nm)	Mean Surface area (μm^2)	Sheet type
800 - 900	0.780 ± 0.28	Large
500 - 600	0.385 ± 0.08	Medium
300 - 400	0.107 ± 0.10	Small

In Figure 4.19, the typical SFM height image and lateral variations depicted for both TRGO-dPG and TRGO-dPGS variants. This provides insight into the surface morphology and characteristics of these functionalized graphene oxide sheets. Moving to Figure 4.20, it showcases the typical state of the small and medium-sized functionalized TRGO at the HOPG & PBS buffer solid-liquid interface. This allows for an understanding of how the functionalized TRGO interacts with the buffer solution and the underlying substrate. Figure 4.21, focuses on the state of the TRGO- dPGS (sulfated variant) at the HOPG & PBS buffer interface, both with and without the presence of the Herpes viral particles. As it can be seen, large aggregates are formed as the TRGO-dPGS (the sulfated version) is in presence of Viral particles at the HOPG interface in buffer solution.

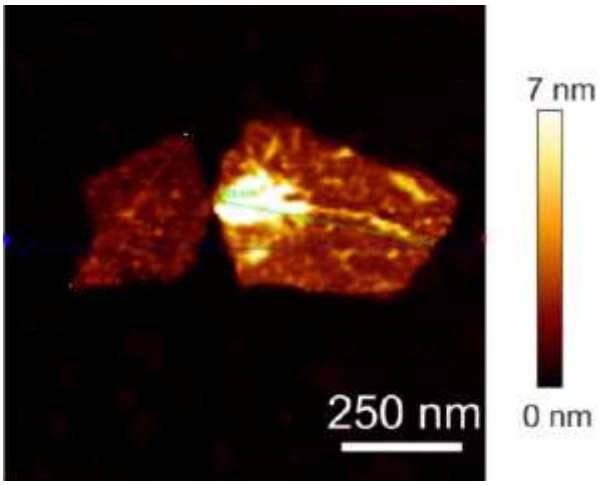

Figure 4.20, SFM-QNM mode height image of the functionalized TRGO sheet at the HOPG & PBS buffer solution interface (liquid, solid interface). Surface, as imaged in PBS buffer droplet in solid-liquid interface. Adapted from reference [130].

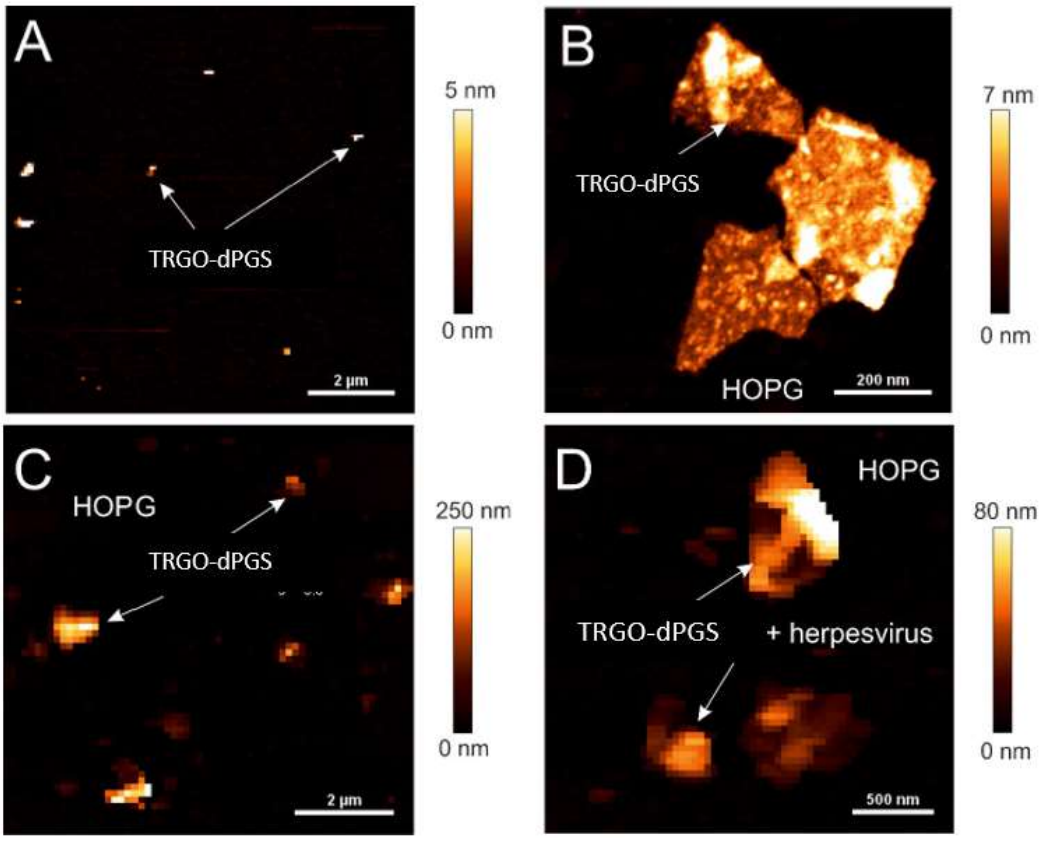

Figure 4.21, Aggregate formation in mixture of TRGO-dPGS and Herpesvirus in buffer (A) Large scan area (88 µm^2) of functionalized TRGO sheets deposited onto the HOPG surface from water dispersion (Measurement in ambient). (B) Close up of the functionalized TRGO sheets of small size with their typical heights with open but wrinkled morphology containing sulfated spherical hyperbranched polyglycerols (dPG). (C) Large scan area (100 µm^2) of the

functionalized TRGO sheets forming large aggregates (sacks) around the virions in a 20 µL PBS buffer solution (Measurement in liquid). (D) Typical geometries and heights of the aggregates (sacks) of functionalized TRGO sheets containing virion. Adapted from reference [130].

In Figure 4.22, the geometrical distributions of the functionalized TRGO-dPGS after incubation with Herpes viral particles are illustrated. This includes the diameter, area, and material volume calculated from typical SFM-QNM height images of the 2D nanosheets and viral particle mixtures at the HOPG & PBS buffer solid-liquid interface. Gaussian fitting of each dataset provides insight into the normal distribution of these data, highlighting the most frequent values for the diameter, area, and volume of the formed aggregates of functionalized sheets after interaction with viral particles.

Observations reveal an average diameter of approximately 500 nm, larger than that of a single Herpes virus particle. Similarly, the volume of the particles was found to be approximately 1.7e7 nm^3 on average, significantly increased compared to the 2D mostly flat functionalized sheets at the interface of the substrate. These values were obtained using height-based pixel selection within the SFM-QNM height datasets with a threshold of height up to 20 nm.[130]

Moreover, according to the Figure 4.23, the larger aggregates formed after incubating TRGO-dPGS and Herpes viral particles at the solid-liquid interface of HOPG and PBS buffer are softer than HOPG substrate. The slope of the Force-distance curve that often describes the stiffness value within SFM-QNM data, demonstrate at least 20 nm deformation at 7nN setpoint forces. This deformation cannot be observed when TRGO- dPGS is present at the HOPG & PBS buffer interface without any viral particle in the mixture.

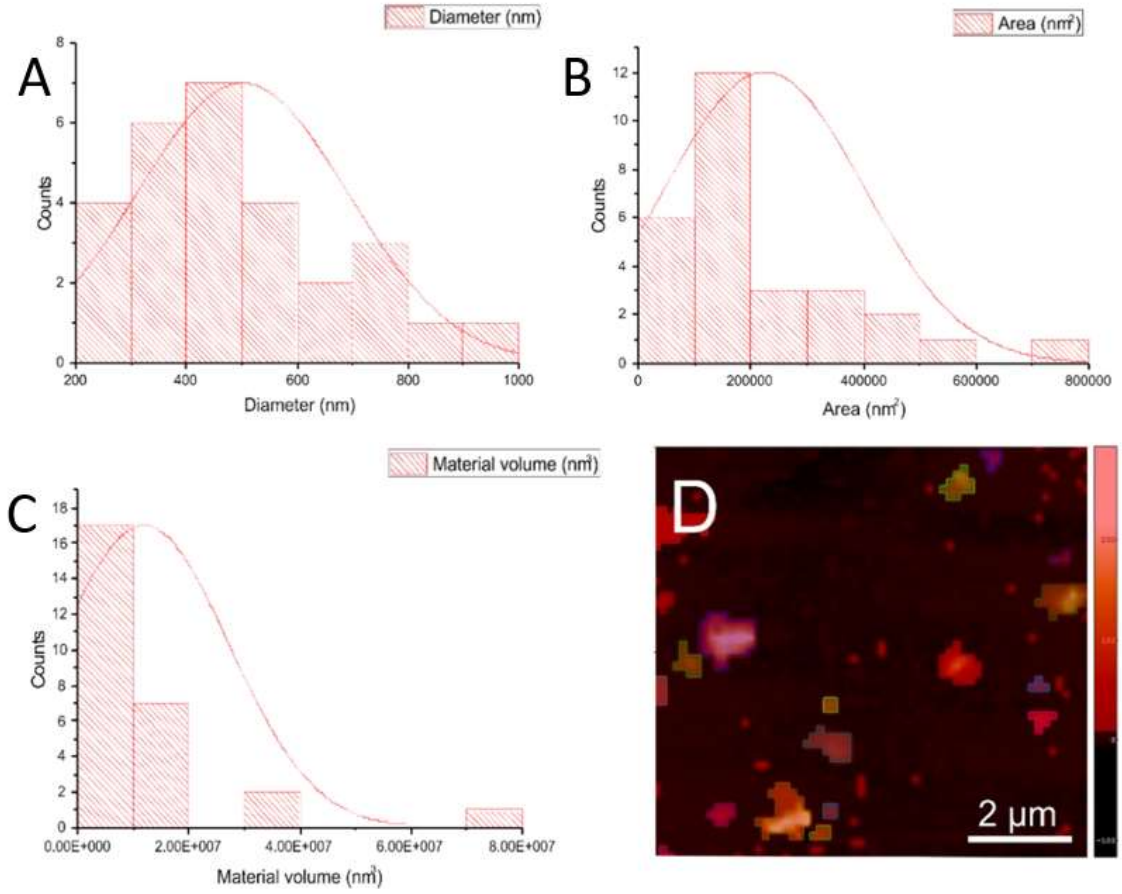

Figure 4.22, (A) Histogram of distribution of the diameter of aggregates attributed to the sacks of virion. (B) Histogram of distribution of the area of aggregates attributed to the sacks of virion. (C) Histogram of distribution of the volume of aggregates attributed to the sacks of virion. (D) An example of the height-based pixel filtration of the SFM-QNM height images used to calculate the diameter, area and material volume. Adapted from reference [130].

The number of aggregates of TRGO-dPGS with Herpesvirus content, (sacks of virions) formed in an area of 100 µm^2 at the HOPG & PBS buffer solid-liquid interface directly depends on the concentration of the 2D functionalized TRGO in the solution dispersion.

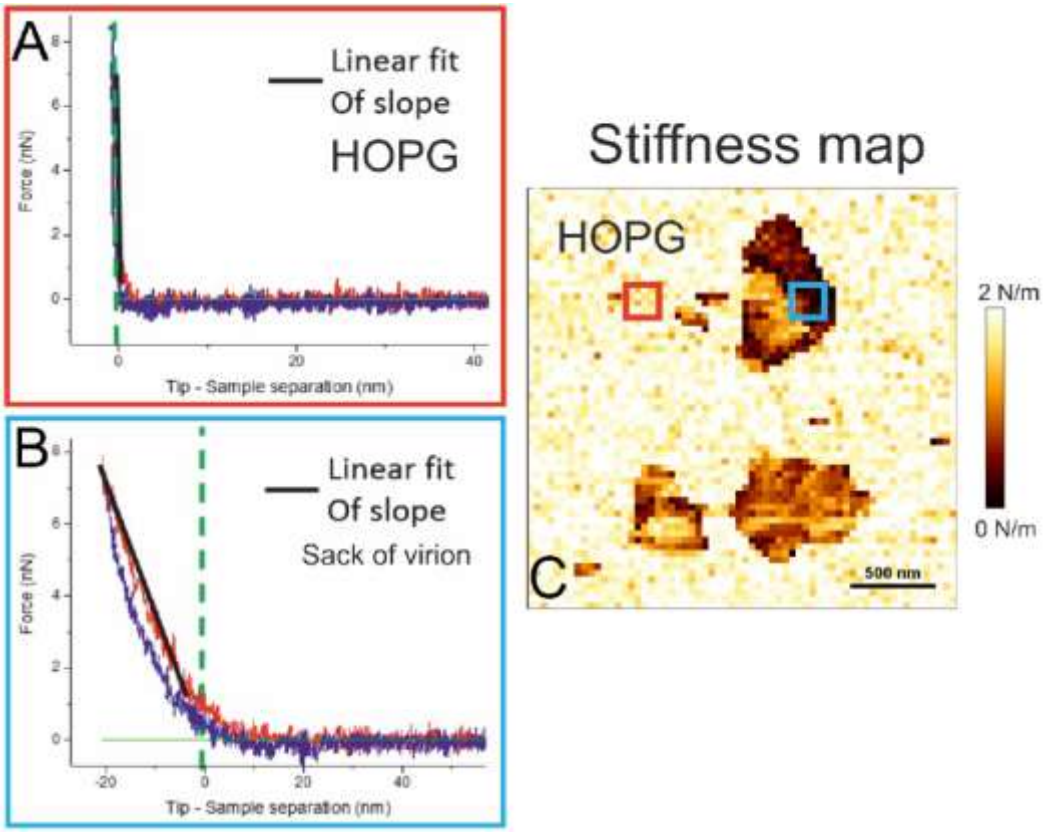

Figure 4.23, (A) The force spectra extracted from quantitative imaging of the 2D Nanosheets and herpesvirus mixture in liquid (PBS) (red square in C) over HOPG shows a very steep slope of extend and retract curves which is fitted with a line. (B) The force spectra extracted from quantitative imaging of the sample in liquid (PBS) over the sack of virion (blue square in C). (C) Stiffness map plotted based on the value of Extend curve slope extracted from every pixel of the SFM-QNM imaging mode. Adapted from reference [130]

4.2. Electronic & structural characterization of "Graft to" Functionalized 2D carbon-based Nanosheets & Triazine based 2D Structures

4.2.1. Electronic and structural characterization of “Graft to” Functionalized 2D carbon-based Nanosheets

As part of the characterization of the functionalized 2D carbon-based nanosheets, it is crucial to understand the effect of the "Graft to" [2+1] nitrene cycloaddition reaction as a versatile multivalent functionalization method on the graphene platforms. The main question addressed in this results series is: What is the extent of the conjugated structure modification of the graphene by the "Graft to" functionalization method? To answer this question, both scanning force microscopy in Tunneling current measurement SFM-PFTUNA and Raman spectroscopy were utilized to investigate the resistivity of the triazine-functionalized 2D graphene nanosheets and their possible doping effects.

The resistivity of graphene nanosheets was compared to their variants, nanographene triazine, and nanographene oxide sheets, based on their contact current measurements at similar bias voltages and similar substrates. These experiments were conducted under ambient conditions at 25°C and 30-45% relative humidity. The results of this study are published, and the written parts here are in accordance with that publication. [132]

Figure 4.24, demonstrates the typical SFM-PFTUNA height images of the Nanographene as deposited onto the fresh Au (111) epitaxial layer over mica.[132] SFM height images demonstrates gold substrate as mainly islands and terraces with line gaps separating them only partially. Nano graphene oxide sheets tend to be immobilized over the Au (111) interface and also close to the island partial gaps over the substrate. Nanographene Triazine sheets were often found randomly located over the gold substrate and often demonstrated few layers and terraces. Often multiple points over the 2D Nanosheets were examined by SFM-PFTUNA in ramp mode, were cantilever was placed onto the 2D Nanosheets or substrate with predefined setpoint force of 2 to maximum 26 nN and then bias voltage applied and I-V curves or I-time curves were measured.

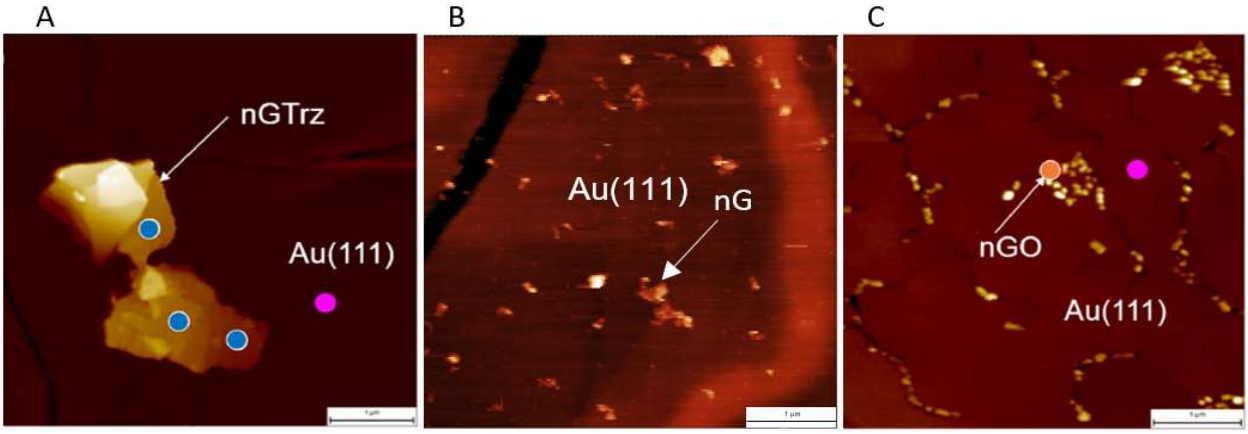

Figure 4.24, SFM-PFTUNA height images of nGTrz and nGO at Gold interface. (A) Large nGTrz sheets deposited onto Au (111) substrate by spin coating from chloroform dispersion. (B) SFM-PFTUNA height image of the nG deposited onto Au (111) from water dispersion. C) SFM-PFTUNA height image of the nGO deposited onto Au (111) from water dispersion. Scale bars in both images is 1μm. Adapted from reference [132].

The SFM-PFTUNA "approach and retract mode – Ramp mode" investigation onto the nGTrz, nG, and nGO was conducted under similar experimental conditions. Specifically, Au (111) was used as the substrate with ambient humidity maintained at 35-45% relative humidity. Similar setpoint forces and substrate resistivities were controlled by ensuring substrate similarities and utilizing the same reference resistor in series.

Figure 4.25A, depicts the Tunneling Current through the sample interface measured over a time scale of 15 milliseconds (I-T curve) during the tip-sample interaction. The data is segmented into three regions: Approach (Blue), Contact (Gray), and Retract (Red) shown in Figure 4.25A, These regions describe the position of the tip relative to the sample during the measurements. The current increases as the tip approaches the sample, reaching a maximum value at the setpoint force. During the "Contact" region, the tip remains in contact with the sample, maintaining a continuous flow of charges. Finally, the current decreases as the tip is retracted from the sample interface. The experiment was repeated for more than 10 samples of each material using different tip-sample bias values.

Figure 4.25B, demonstrate the Current vs Sample Bias (millivolts) or I-V curve for the 2D Nanographene variants. It is important to note the observed ohmic contact

shape of the I-V curve data at the Bias range of ±60 mV for nGTrz, nG and nGO. It was observed after Au (111) I-V curve data slope, the nGTrz demonstrated the second highest slope of an I-V curve and nG and nGO in all experiments at similar conditions. nG demonstrated the third highest slope within the data visualization of the I-V curves and nG showed the smallest slope of I-V curve data.

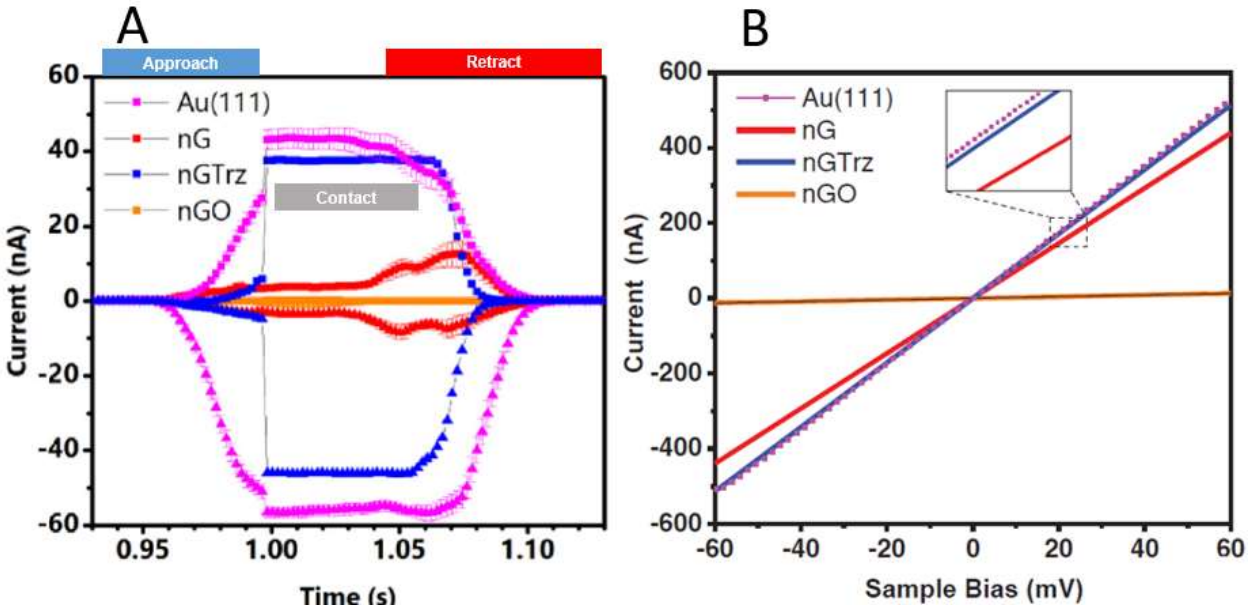

Figure 4.25, Current vs Time and Current vs Bias for nGTrz, nG and nGO. A) Contact current over time at constant bias of 60 mV (squares) and -60 mV (triangles) on Au (111) substrate, for nG, nGTrz, and nGO, with standard error values. The setpoint force was 26 nN. B) Averaged current–voltage (I–V) measurements of Au (111) substrate, nG, nGTrz, and nGO over gold substrate with 110 kΩ resistor in series, at 26 nN contact force. Detail inset to better see differences between Au (111), nG, and nGTrz. Adapted from reference [132].

The Raman spectra (Figure 4.26A) of the graphite powder (starting material), nG, and nGTrz deposited from solution dispersion onto an oxidized layer of a silicon wafer in ambient show only slight variations. Notably, differences between nG, graphite powder, and nGTrz were observed mainly within the region around 1610-1620 cm^{-1}, often associated with the D' peak positions of graphene. [127,137] All 2D carbon-based structures demonstrated a band within the 1320 – 1380 cm^{-1} wavenumbers, a small D peak and a G peak at a position of 1589 cm^{-1} according to the observations within Guday & Gholami *et al*.[132]. Various data presentations were created based on the Raman spectra peak positions observed for "Graphite powder", nG and nGTrz Nanosheets and shown in following figures.

To compare the observations of the spectroscopy information, the ratio of the intensity of the D peak vs G peak (ID/IG) was plotted against the Full Width at Half Maximum (FWHM) of 2D (Γ2D) in (Figure 4.26B). A clear differentiation of the data for nG and nGTrz was observed based on the FWHM of the 2D peaks. Additionally, the ratio of (I_D/I_G) vs position of G peak (ωG) and the position of 2D peak (ω2D) vs the ωG were plotted for the nG and nGTrz Nanosheets. With linear fitting, the slope of the (ω2D) vs (ωG) for nG was 1.19 ± 0.17, while for nGTrz, the slope value was 0.58 ± 0.09. nG presents a 2D peak near 2700 cm^{-1} with a FWHM of 25.8 ± 0.7 cm^{-1}. Specifically measuring the Raman spectra of nG Nanosheets with higher concentration over substrate and multilayers demonstrated a 2D peak FWHM of 65.0 ± 1.1 cm^{-1}. These are according to the observations as published in Guday & Gholami *et al*.[132]

nG demonstrated an (I_D/I_G) ratio of 1.75 ± 0.12 and nGTrz that of 1.04 ± 0.07 which is significantly lower (Figure 4.26C). Moreover, as part of a collaborative research activity and as reported in the publication by Guday & Gholami *et al*.[132], Raman intensities were calculated in regions of interest for atomistic models of nG, nGTrz and def-nGTrz containing stone-wales defective structures. For these, phonon frequencies were determined by calculating the Hessian matrix using finite differences as implemented in Vienna Ab initio Simulation Package, as also described in the publication by Guday & Gholami *et al*.[132] Furthermore, The Raman intensities were simulated by calculating the macroscopic dielectric tensor, as shown in spectra (Figure 4.26A) generated for the nGTrz model system as well as the nG and defective nGTrz systems. As demonstrated, simulated Raman intensities compare quite well to the primary peaks from experimental results. The D, G, and D′ bands of the experimentally measured nGTrz spectrum can be assigned to peaks in the simulated spectra arising from the cumulative calculated spectra.

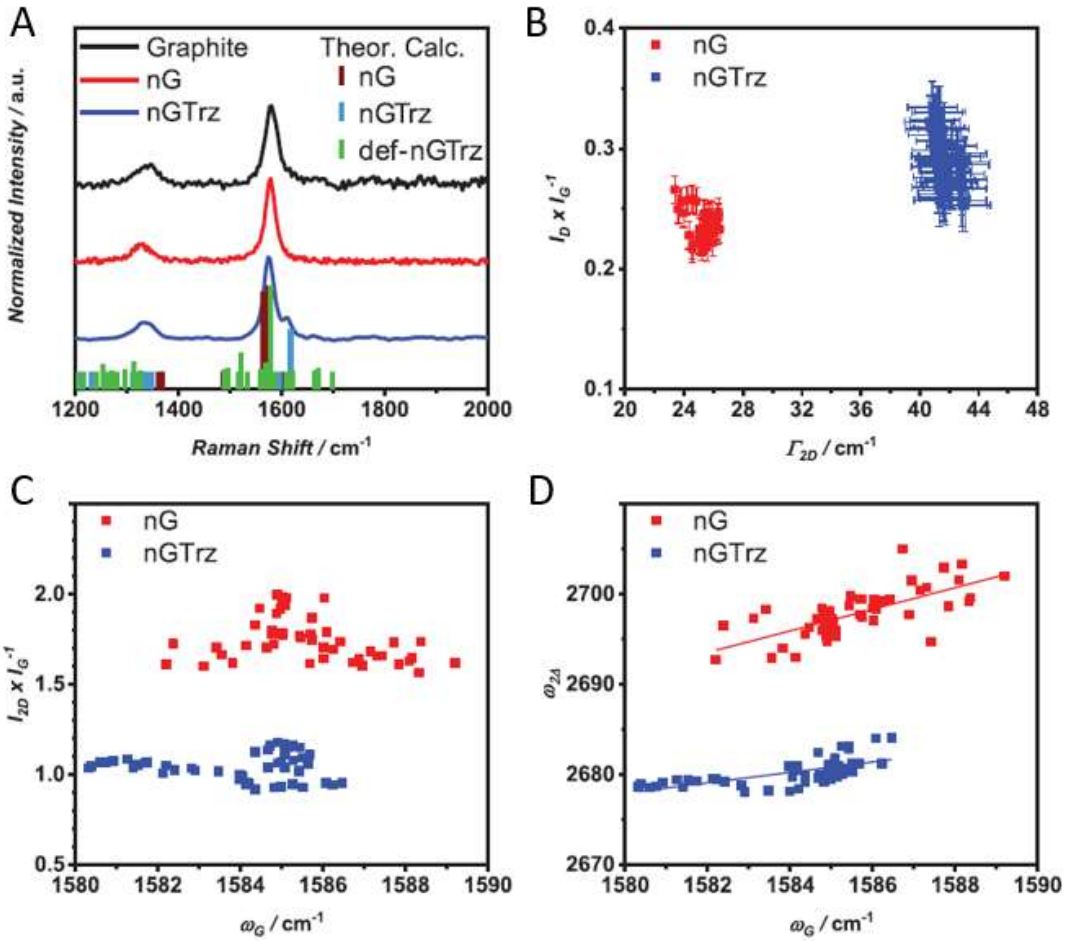

Figure 4.26, Raman spectra and analysis comparison of the nGTrz and nG. A) Raman spectra of graphite starting material, nG, and nGTrz along with theoretically calculated peaks arising from nG, nGTrz, and Stone–Wales defective nGTrz (def-nGTrz). Raman intensities are calculated in regions of interest, with phonon frequencies determined by calculating the Hessian matrix using finite differences as implemented in Vienna Ab initio Simulation Package. Raman intensities were simulated by calculating the macroscopic dielectric tensor. B) I_D/I_G versus the FWHM of the 2D (Γ_{2D}) band for nG and nGTrz. C) I_{2D}/I_G versus G band wavenumber (ω) for nG and nGTrz. D) ω_{2D} versus ω_G for nG and nGTrz. Adapted from reference [132]

4.2.2. Triazine and carbon-based two-dimensional materials

In this section of the thesis, the focus is on the physical characterization of a metal-assisted and solvent-mediated reaction between calcium carbide and cyanuric chloride to synthesize two-dimensional Triazine structures (2DTSs). The main

objectives are to investigate whether the [2+1] cycloaddition reaction of cyanuric chloride and/or Triazine as a monomer could result in 2D structures and to determine the crystalline or disordered nature of these structures. Scanning Force Microscopy (SFM) in quantitative imaging mode was employed to examine the two-dimensionality of the 2DTSs, while Raman spectroscopy and mapping were used to assess the extent of their ordered structure. The results of this study have been previously published [133] and are described here in accordance with that publication.

Measurements using SFM-QNM of the 2DTSs deposited onto freshly cleaved muscovite mica revealed layered structures with lateral sizes ranging from 2 to 3 μm and thicknesses ranging from 100 to 350 nm. These layers and terraces included smaller layers with self-overlapping regions (folds) and exhibited an inhomogeneous distribution of mobile and small interconnected particles above the larger flakes. The root mean square (RMS) roughness was measured to be 1 nm. This information is further illustrated in Figure 4.27 and Figure 4.28 and was published in the work of Faghani & Gholami *et al* [133].

Figure 4.28 is mainly consist of two height images (A, C) and two height profiles (B and D). The height image (A) demonstrate the typical topographical interface of the 2D Triazine structures found at the interface of Mica substrate with thickness of tens to hundreds of nanometers (height profile B). The height image (C) demonstrates the typical topographical variation of the 2D Triazine structures in more details. Therefore, height image in Figure 4.28C is indeed a zoom in from the height image in (A) demonstrating smaller structures with folds and wrinkles and with height variations found to be as small as 5 nm (height profile D).

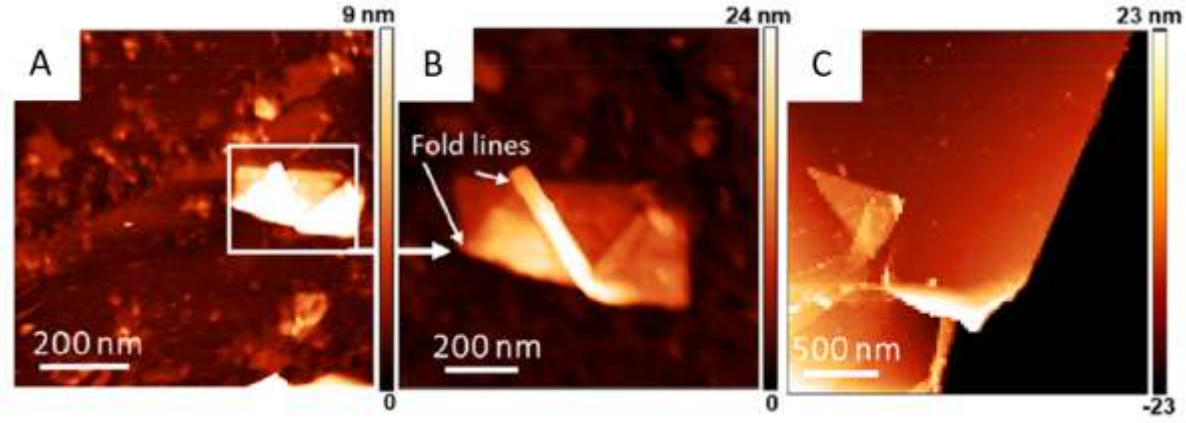

Figure 4.27, SFM height images of 2D Triazine structure. A) SFM-QNM height image of the product of the reaction under anhydrous conditions with plateaus and terraces. B) Close-up

image of a sheet obtained under anhydrous conditions with back folding. A planar layer topography is evident from the height image. C) SFM-QNM height images of a large plateau of graphitic material. Adapted from reference [133]

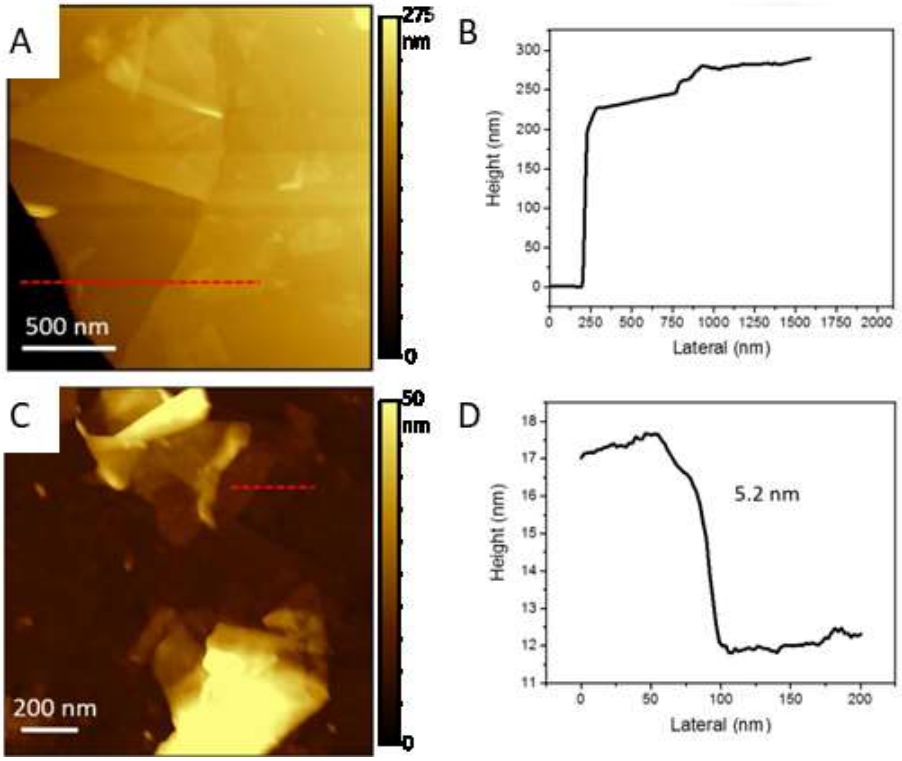

Figure 4.28, Height profiles of 2D Triazine structures. A) SFM-QNM height image product of reaction obtained under anhydrous conditions B) the line height profile shown in (A). C) a close up SFM-QNM height images of different areas over a typical plateau as sown in (A). D) line height profile shown in (C). Adapted from reference [133]

Figure 4.29, Demonstrate the topography of the smaller 2D sheets found via SFM-QNM from deposition of the 2DTSs dispersion from Ethanol or chloroform onto freshly cleaved Mica. Figure 4.29, shows the typically found thinnest structures. Mainly these Nanosheets are found to have a typical height of 0.5 nm based on the statistical height distribution in Figure 4.29 D. Lateral sizes between 100 to 250 nm were commonly observed for those Nanosheets. Measurement were carried out in ambient environment. Ethanol and Chloroform solvents used for dispersion without 2DTSs did not show such structures on freshly cleaved mica.

Figure 4.30A and B, demonstrate the SFM-QNM height image of the structures produced as a result of the reaction of Triazine and calcium carbide in presence of EDTA that is specifically used to interact with the metal ions and specifically Ca ions

present within the synthesis reactions. Furthermore, Figure 4.30C and D, show the product of the reaction of Triazine and calcium carbide in presence of sodium carbonate.

As it can be seen in the Figure 4.30, typical product of synthesis in the aforementioned experimental as measured by SFM-QNM are structures devoid of any smooth interface, terraces and any wrinkling or folding. Additionally, the object varied in their lateral dimensions and height widely, varying from few hundreds of nanometers to micrometers in height. For this observations, SFM-QNM samples were prepared exactly in the same procedure used to create the structures observed in Figure 4.27 by deposition of material from solvent dispersions onto mica interface in ambient.

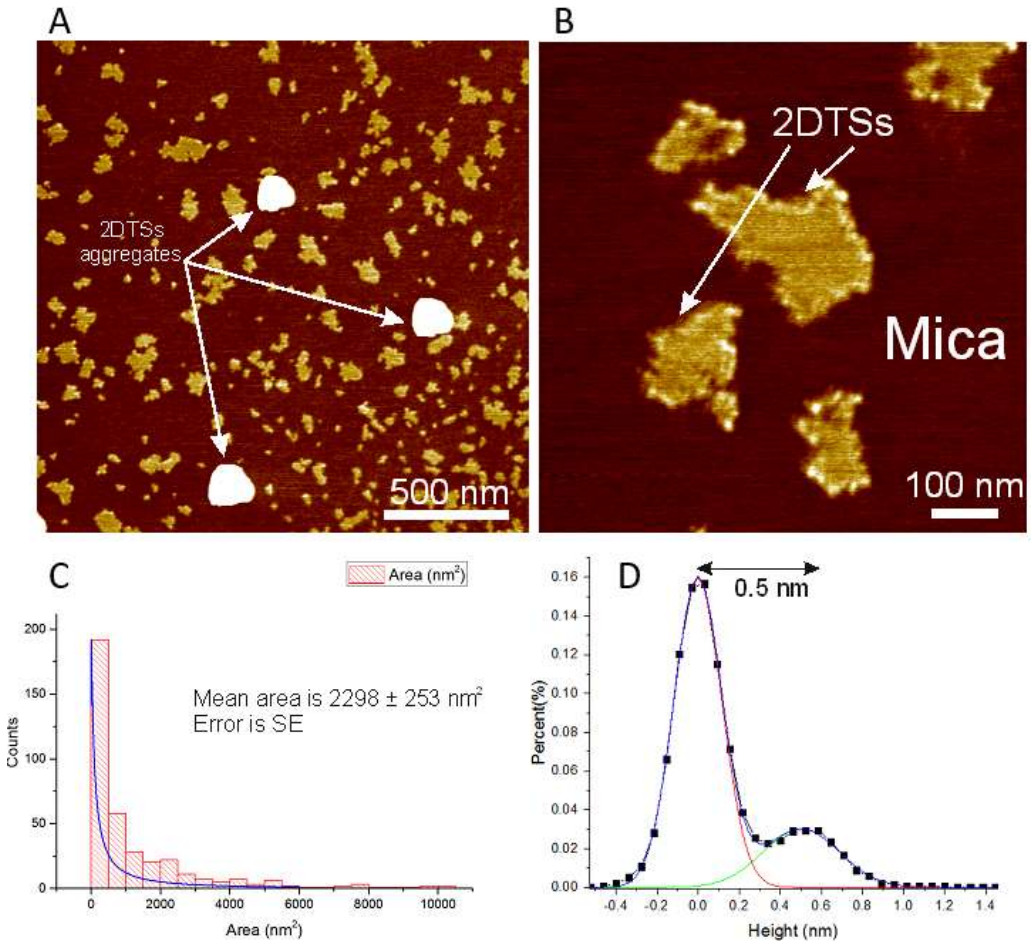

Figure 4.29, SFM-QNM topography of thin 2D structures from 2DTSs. A) SFM-QNM height image of the thin sheets found in 2DTSs dispersions on freshly cleaved mica interface. B) Close up of laterally small and thin sheets of 2DTSs observed. C) Distribution of 2D area of the sheets from (A). D) Height histogram of the thickness of the thin sheets.

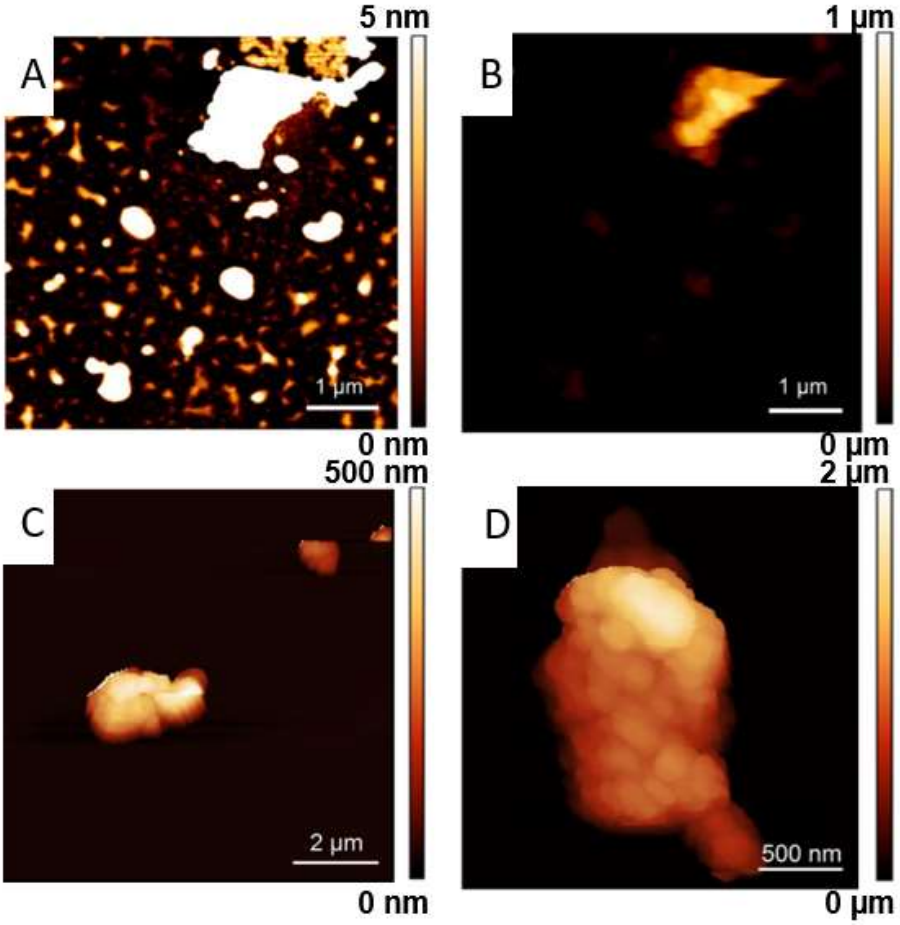

Figure 4.30, SFM-QNM height image of Triazine based structure without Ca assist. A) SFM height images of product of Triazine and Calcium carbide reaction in presence of EDTA. B) same as (A) with higher height contrast. C) SFM height images of product of Triazine and Calcium carbide reaction in presence of Sodium carbonate. D) similar sample to (C) but larger particle. Adapted from Reference [133]

Mainly two types of Raman spectra were observed for 2DTSs, both types demonstrated qualitative similarities with the often-observed Raman spectra for graphite and that of a carbon-based disordered structure reminiscent of Graphene oxide when exposed to the 532 wavelength of laser. Later experiments allowed separation of those two main Raman spectra based on the synthesis routes of them. Raman spectra of the product of Triazine and calcium carbide at 25 ºC and in presence of water, product of the same reaction but at 120 ºC and in Non-dry DMF solvent and lastly product of the Triazine & Calcium carbide reaction at 120 ºC in anhydrous DMF. The Raman spectra were named 2DTSs (Figure 4.32) and Graphitic material (GM) (Figure 4.31), where 2DTSs, Raman spectra was observed only from the reaction product in anhydrous conditions and GM Raman spectra was observed only for reaction product in presence of water.

Furthermore, reaction product of the Non-dry synthesis in DMF resulted in observation of mixture of particles demonstrating both the 2DTSs and GM spectra properties.

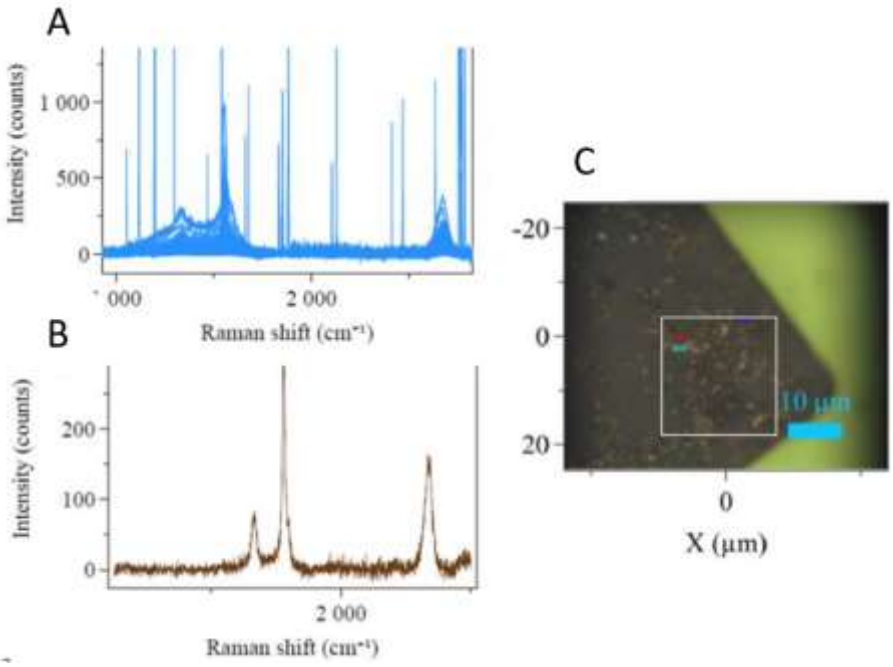

Figure 4.31, Raman-mapping spectra cluster of 2D Triazine material in the white square region shown in (C). (A) A typical Raman spectrum of particles found in the mapping region. (B) Optical microscope image of the Raman-mapped region of particles synthesized with water content (GM) as deposited onto TEM grid. Adapted from reference [133]

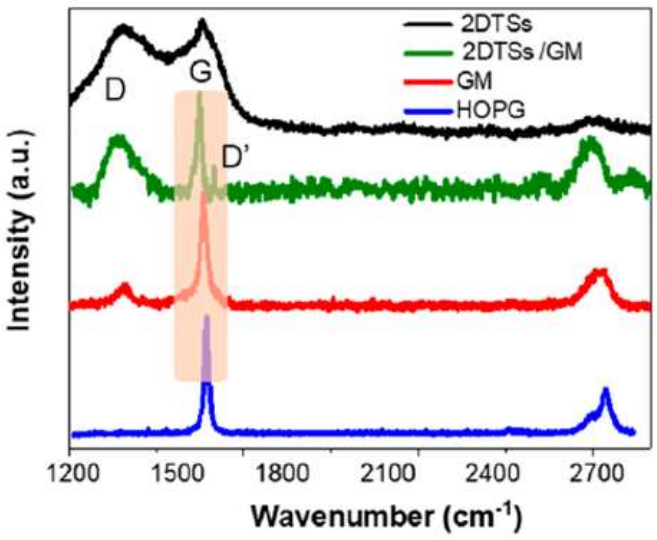

Figure 4.32, Raman spectra overlay comparison of 2D Triazine mixtures with GM And the G and D' peak frequency regions of the 2DTSs, GM, and highly oriented pyrolytic graphite (HOPG).

The photochemical properties of 2DTSs were investigated by different methods. 2DTSs showed a maximum UV absorption at 235−276 nm as seen on the Figure 4.33A. Using 1,3- diphenylisobenzofuran (DPBF) as a specific singlet oxygen scavenger, singlet oxygen production of the 2DTSs structures were investigated, Figure 4.33B. The singlet oxygen production of the 2DTSs were then measured by observation of how the DPBF absorbance changed with time of exposure of the solution of 2DTSs and DPBF in ethanol to 638 nm Laser beam. The rate of singlet oxygen release was then measured by plotting the natural log ratio of:

$$-\ln\left([DPBF]_t\right) / \left([DPBF]_0\right)$$

That is ratio of measured concentration of DPBF at time (t) and to initial concentration of DPBF in the mixture which is directly dependent on the absorbance change of DPBF in presence of singlet oxygen release in the solution. The slop of the plot against time in minutes gives the rate of release of singlet oxygen in the solution at different exposure times. These values were then compared quantitatively to the singlet oxygen release of Methylthioninium chloride also known as “Methylene Blue” reference measured in similar experimental settings.

It was observed for the mixture of the 2DTSs, DPBF and ethanol that the absorbance of DPBF decreased as the irradiation time to the exciting laser wavelength increased.

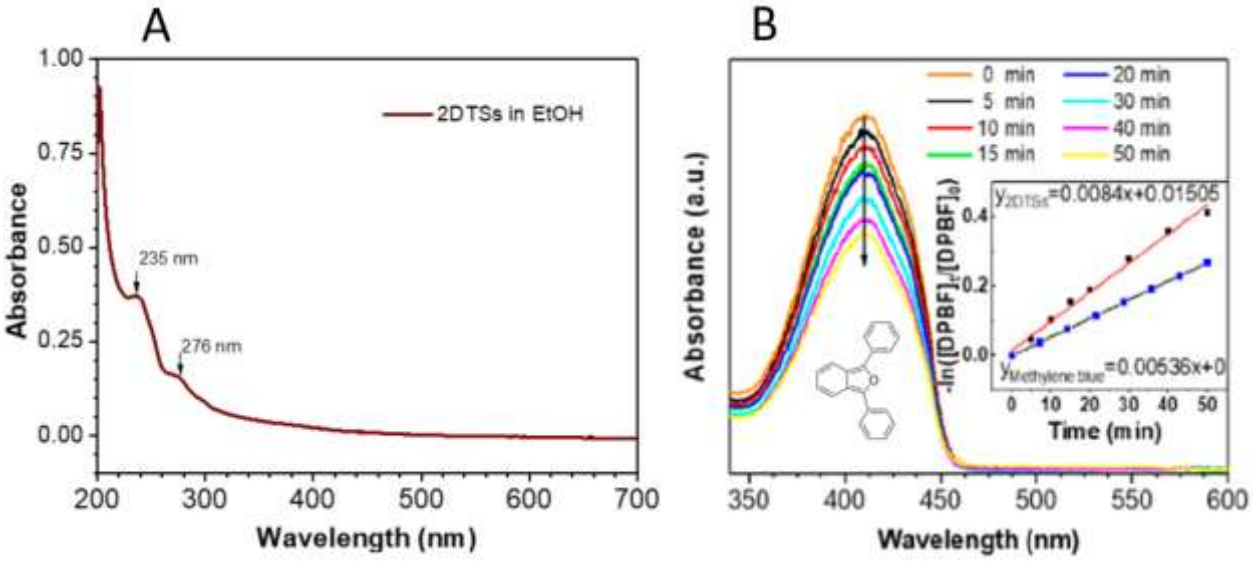

Figure 4.33, UV-Vis spectrum and Singlet oxygen release of 2D Triazine structures. A) UV-Vis spectrum. B) DPBF & 2D Triazine mixture absorbance change in Ethanol. Adapted from reference[133].

Chapter 5

5. Discussion

In this chapter, the results as described in chapter 4 are further discussed in more details. Discussion subsections 5.1 & 5.2 includes, topographical and interfacial interactivity of the 2D functionalized carbon-based sheets mainly based on the “Graft to” functionalization as it is highly relevant to the controlled functionalization using triazine molecules as the initial multivalent structural modification of the 2D carbon-based sheets of TRGO and their post-functionalization. These discussions are based on the discussions of the experimental results as published in Gholami *et al.*[32] & Faghani & Gholami *et al.*[97]

Subsection 5.3, discusses the lateral size dependency of the viral interactions for the “graft from” method of functionalization based on the described results in 4.1.3 and Experimental & methods 3.3 & 3.4 and as described in the publications by Ziem & Gholami *et al*.[130,131] The discussion in this chapter also provides a comparison point of view with the “graft to” method of functionalization and its characteristics.

In subsection 5.4, the results described in 4.2.1 are further discussed in accordance to the publication by Guy *et al*.[132] These mainly include the discussion on the evidence regarding the resistivity measurement of current through Graphene, Graphene -Triazine and in comparison thereof with Graphene oxide. The discussion further describes the intactness of the π-conjugation of graphene after covalent functionalization with Triazine. Discussion further describes the possible reason for the lower resistivity of Graphene-Triazine in compare to Graphene through Raman spectroscopy experimental result discussion.

Lastly, in subsection 5.5, results described in 4.2.2 will be discussed in more details based on the publication of Faghani & Gholami *et al.*[133]. This subsection discusses the possibility of utilization of the Triazine not only as an out of plane multivalent functionalization agent for 2D carbon-based sheets but also as an in plane 2D monomer. As observed in the results chapter, SFM methods in combination with far field Raman spectroscopy of the new synthetic structures based on Triazine and Carbon can both inform topographically and atomically regarding the two dimensional and possible atomic scale crystallinities of those novel materials, respectively.

5.1. Topography and interfacial activity of 2D carbon-based Structures

The topography and structure of the functionalized TRGO sheets were investigated systematically using Scanning force microscopy in quantitative nanomechanical mapping mode (SFM-QNM). Stepwise increase in the thickness of the functionalized TRGO demonstrates the covalent attachment of the external molecules onto it. This is more precisely observable in case of increase in the interlayer distance of the functionalized sheets laying over each other. Since the interlayer distance measures is from one functionalized sheet to another, the height measurement artifacts present in the SFM-Tapping mode do not apply due to similarity of material layers measured. Nevertheless, the quantitative nanomechanical mapping allow measurement of the height and topography of functionalized 2D sheets accurately with omission of their height reduction due to deformation. Therefore, the quantitative nanomechanical mapping and quantitative imaging modes of SFM in which the applied set point force can be controlled accurately and height measurement is not triggered by chemical differences of the sample are the most accurate and suitable methods of data collection for these multivalent 2D carbon-based Nanosheets.

Thermally reduced graphene oxide as the initial platform of multivalent functionalization is itself a variation of Graphene oxide (GO). It is known that GO contains various randomly distributed oxygen containing functional groups within its basal plane. TRGO on the other hand has been produced by exposure of the GO to high temperature reduction process under inert atmosphere. Although most of the oxygen containing functional groups of GO are reduced and removed during this Thermal reduction process, the –OH functional groups remain at the TRGO interface. This renders TRGO a more hydrophilic interface than a pure graphene sheet. Presence of those –OH groups also adds to the overall thickness of the TRGO, increasing the thickness from observed value for graphene 0.3 nm [2,138] to 0.6 nm as observed in this study, Figure 4.1. Since, the thickness of TRGO sheets was previously reported to be in the range of 0.5–1.3 nm, [139,140] we attributed the thicker sheets and terraces observed experimentally in this research to the multi- and single layers of TRGO-Trz, respectively.

Covalent bonding of the Triazine (Trz) groups to the basal plane of TRGO sheets using [2+1] nitrene cycloaddition reactions is the initial step for “Graft to”

methodology. This process creates the (TRGO – Trz) sheets. The density of the Triazine groups covalently at the interface of the TRGO is controllable by the amount of the (Trz) used during the synthesis, reaction time and number of the repeated reaction runs. Initially after functionalization of TRGO with Trz groups the Nitrogen content was estimated using elemental analysis (Appendix Table 11.1). This was an estimate, on the number of the conjugated Triazine groups to TRGO. The degree of functionalization is then written as:

$$DF = \frac{Number\ of\ Triazine\ groups\ (N\ wt.\%)}{Number\ of\ carbon\ atoms\ of\ Graphene(C\ wt.\%)} \times 100$$

Considering elemental analysis results, the DF of TRGO-Trz is around 1.7% for the synthesis carried out at 70 ˚C. That is one Triazine group per ~59 carbon atoms.

Although, other methods of investigation such as; Infrared spectroscopy (IR), X-ray photoelectron spectroscopy (XPS) and Thermogravimetric analysis (TGA) can demonstrate the effect of Triazine presence along with the TRGO characteristics, only Scanning force microscopy can demonstrate the direct observation of the covalent attachment of Triazine onto the TRGO 2D sheets interface. The SFM observation can therefore, rule out the presence of the Triazine as a free molecule in mixture with TRGO sheets.

As a result of a homogenous functionalization, TRGO-Trz variant now demonstrate a higher topographical height in compare to the unmodified TRGO as seen in Figure 4.2. Typically, thinnest observed layer of TRGO-Trz was found to be 2.2 nm as also described in the publication by Gholami et al.[32] This demonstrate the attachment of a thickening layer onto the typically known TRGO sheets which is, a homogenously distributed molecular layer containing chlorines, covalently attached perpendicular (out of plane) to the basal plane of graphene, that is stable and unmodified after continues SFM scans.

Successful covalent attachment of Triazine to TRGO created a multivalent 2D Carbon-based structures that could be altered chemically similar to a dichloro-triazine. This implies that, later replacement of the chlorine atoms with nucleophilic hyperbranched polyglycerols containing –(NH_2) are possible and each chlorine replacement could be controlled using reaction temperature control. The first chlorine of TRGO-Trz can undergo nucleophilic reaction at room temperature, producing the

TRGO-Trz-hPGlow variant in which polymer content per Triazine is only one hyperbranched polyglycerols.

Furthermore, later reaction of the TRGO-Trz-hPGlow with further hPG with –(NH_2) end groups at 100 ^oC, creates the higher polymer coverage variant of TRGO-Trz-hPGhigh. Therefore, topographical observation of difference between low polymer content and high polymer content TRGO-Trz 2D sheet demonstrate the successful covalent control on the density of multivalency on those 2D nanomaterials. Both low and high hPG coverage TRGO- Trz were characterized as the novel graphene-based interfaces with hyperbranched polymer coverage, Figure 4.4 and Figure 4.5, respectively. SFM-QNM and SFM-QI were used to understand the interfaces based on their nanomechanical variations and make sure that polymer coverage is covalent and not just an adsorbate onto the TRGO-Trz. Figure 4.4, shows the typical TRGO-Trz-hPGlow with its incomplete polymer coverage over the TRGO-Trz areas. Elevations and depressions observed in case of the 2D sheets with low hPG content are attributed to the areas of the TRGO that are not functionalized by the polyglycerols mainly due to lack of high polymer content during reaction. These hPG less regions within TRGO-Trz-hPGlow sheets also demonstrated a pull off force contrast that was similar to that of the HOPG substrate, Figure 4.4B. In contrast, the high polymer content TRGO-Trz-hPGhigh demonstrate a fully covered interface of TRGO-Trz with easily deformable spherical objects relative to the TRGO covering its interface, Figure 4.8.

The SFM-QNM data verifies the hypothesis that the hPG coverage and attachment is controllable in those functionalized 2D Nanosheets. Figure 4.3, demonstrates a high resolution SFM height image of the high polymer content variant (TRGO-Trz-hPGhigh) sheet with its edge as deposited over freshly cleaved mica. As it can be seen, high density of spherical objects with diameters varying between 5-10 nm are observed. Figure 4.3, demonstrates the hPG dense coverage that are extended even to the edges of the TRGO-Trz-hPGhigh, creating a homogenous structure. This correlates well with the pull-off force mapping of the functionalized sheets Figure 4.5B, showing a homogenous contrast of the repetitive spherical objects at the TRGO-Trz-hPGhigh interface in compare to the HOPG substrate in the experiment.

Based on the topographical observations using Scanning force microscopy, it is possible to model and thought about the topography of the TRGO-Trz-hPG sheets

similar to topography of a low- or high-density jungle over a plateau of land. This comparison is demonstrative of a new stable conformation of hybrid 2D flexible nanomaterials that are functional depending on type of the Grafted molecules or in terms of example here, “Trees”. Similarly, the effect of packing density of hyperbranches on their spherical structures and roughness of the observed functionalized 2D sheet are similar to observation of the high density packing of trees in a jungle.

Functionalized 2D Sheets TRGO-Trz-hPG were later post functionalized with a sulfation process that exchanges the end groups of the hPG from (OH) to the (SO4). This effectively changes the surface charges of the hPG to a highly negative value and creates the TRGO-Trz-hPGS structures. Similar to the precursors, the sulfated versions were created for both low and high hPG content sheets. Figure 4.10, demonstrates a typical TRGO-Trz-hPGS as deposited onto a freshly cleaved HOPG surface. As it can be seen, the structure topography is unchanged relative to the non-sulfated high polymer content precursor and the height variation between the two variants is very small.

5.2. “Graft to” functionalized 2D Nanosheets & Viral Interactions

One grave issue for a systematic study of such nanoscale multivalent structures, is the full recognition of the interacting surfaces and in particular their functionalities. [80,93,141] In the case of the TRGO-Trz-hPG and its sulfated variant TRGO-Trz-hPGS, the homogeneity of the polymer coverage remains similar after sulfation, yet the surface charges change greatly. This renders those systems more potent for possible electrostatic interactions that as well could be non-specific. This brings up the next stage of utilizing these functional active interfaces for interaction studies with the viral model, in this case VSV.

The SFM-QNM data and Cryo-TEM images provided insight into the binding capacity of TRGO-PGShigh with the VSV viral enveloped models. Tapping and QI mode SFM imaging thereafter revealed that virions adhered to the surface of TRGO-PGShigh and to a much lower extent to TRGO-PGhigh see Figure 4.14.This was also confirmed by the Cryo-TEM images of Individual sheets of roughly 1 μm × 1 μm size that could bind to about 20 virions in case of the sulfated variant. In control

experiments, where VSV buffer solution was applied onto freshly cleaved HOPG or onto graphite coated with TRGO-Trz, no virions were observed.

Since a few virions could also be found at the surface of TRGO-Trz-hPGhigh, an evaluation of the consecutively recorded SFM-QNM & SFM-QI images of VSV on TRGO-Trz-hPGhigh sample areas revealed subsequent deterioration of the virus structure see Figure 4.16A &B. Surveying larger areas, which had not been repeatedly scanned before, revealed no deterioration of VSV. Thus, repeated scanning caused subsequent disintegration of the virions. Remarkably, topography of VSV particles attached to the surface of TRGO-Trz-hPGShigh did not change after sequential scanning with time.

The observed difference in the structural integrity of the VSV particles found over sulfated and non-sulfated functionalized 2D sheets had to be assigned to the type of functionalities involved, namely effect of sulfation rather than topographical differences which are mostly insignificant for TRGO-Trz-hPGhigh and its sulfated version, TRGO-Trz-hPGShigh. The interaction property of the sulfated variant of functionalized 2D sheets is attributed to the electrostatic interactions between the negatively charged multivalently sulfated surface of TRGO-Trz-hPGShigh and positive available charges at the tightly packed glycoprotein on the VSV envelope. [142,143] Furthermore, not only for the process of virus binding but also for stability against mechanical stress induced by the normal and shear forces applied by the scanning force microscopy. Both the amount of virion attached to the surface of functionalized TRGO sheets and their sizes were investigated.

Furthermore, In Vitro assays found that TRGO-Trz-hPGShigh showed potent binding towards VSV at low concentrations, while higher concentrations were required for TRGO-Trz-hPGhigh to interact significantly with VSV. It was further understood that the performance of TRGO derivatives in a cellular environment by assessing their side effects such as unspecific cell binding, cytotoxicity, and hemolytic activity. They found that TRGO-PGShigh did not show agglutination character, accounting for no unspecific binding to cell membranes up to 200 μg mL−1 concentrations. They also observed that polyglycerol coverage substantially reduced the hemolytic activity of TRGO-Trz precursor.

Based on the work done by Group of Prof. Andreas Hermann and Dr. Daniel Lauster, cell viability assay with Baby Hamster Kidney (BHK) cells were carried out. Experiments did not show any cytotoxicity upon incubating cells for 24 h with different TRGO-Trz-hPG & TRGO-Trz-hPGS variants up to concentrations of 200 µg mL−1. Therefore, it was concluded that the hyperbranched polyglycerol coating of TRGO-Trz reduces undesired side effects in a cellular environment, providing TRGO variants features for the further development of an antiviral material with high viral absorbance character.

5.3. Size dependency of interfacial activity for functionalized 2D carbon-based Nanosheets

In this part of the studies, different lateral sizes of 2D Nanosheets were functionalized with dendritic polygylcerols through a “Graft from” polymerization process to form new Multivalent interfaces capable of viral inhibiting after post-modification (polysulfation). Polysulfation of 2D Nanosheets introduces a mimic of the heparan sulfates present at the mammalian cell surface [144,145]. As observed in the previous discussion, sulfation of the multivalent functionalized 2D Nanosheets is expected to have electrostatic interactions with the glycoprotein or the envelop protein of some viral particles and reasoned to be able to compete with the binding sites of orthopoxvirus, herpes simplex virus type 1 (HSV-1) and equine herpesvirus type 1 (EHV-1). These viruses all cause major global health issues. This section of the thesis, discusses the topographical characteristics of the “Graft from” functionalization method for 2D carbon-based Nanosheets. Additionally, effect of lateral size of the functionalized 2D Nanosheets on the interaction efficiency & inhibitory efficiency of the virus model particles are discussed. The combined system of sulfated functionalized 2D Nanosheets and virus particles demonstrated formation of soft and 3D aggregates of similar height to the viral particles of EHV-1. Implying interaction of functionalized 2D sheets of 200-300 nm lateral sizes with viral particles through electrostatic interactions and geometrical entrapment (wrapping of virus) and consequent viral inhibition. Therefore, the size of the 2D nanomaterials in addition to their degree of sulfation was found to be the key to efficient viral inhibition through entrapment. The most efficient inhibiting functionalized 2D sheets were on average ∼300 nm in lateral

sizes and had a degree of sulfation of ~10%. Further, discussions on this study are published[130,131].

According to the SFM-QNM height images, it was noticeable that the height of the TRGO-dPGS sheets were less than that of the TRGO-Trz-hPG and its sulfated variant measured in section 4.1.1. Furthermore, the typical height image in Figure 4.19, shows topographically higher plateaus with folding and wrinkling within the TRGO-dPG structure, demonstrating its flexibility and versatility. Moreover, Analysis of the tapping mode scanning force microscopy (SFM-TM) height images revealed a mean sheet size of 0.79 ± 0.24 μm^2 and demonstrated that the polymers were equally distributed on the TRGO sheets Figure 4.17.

The dimensions of the dendritic polyglycerol grafted TRGO sheets were determined using tapping and quantitative mode scanning force microscopy, as shown in Figure 4.19. The longest axis of the sheets was measured from height profiles and used to group them into three size categories: small (300-400 nm), medium (500-600 nm), and large (800-900 nm). To determine the surface area of the sheets, height-dependent area measurements were conducted. However, this method was limited to individual sheets and did not account for overlapping sheets on the mica surface. Additionally, functionalized nanodiamonds (ND-dPGS) were used as a comparative 3D Nanomaterial to 2D functionalized carbon-based sheets. The average size of those nanodiamonds were determined by dynamic light scattering (DLS).[131]

To investigate the potential of the different synthesized functionalized 2D carbon-based sheets to inhibit virus infection, viruses (HSV-1 & EHV-1) were incubated with the those 2D multivalent Nanosheets and then added mixture to the cells. After few hours of exposure of cells to the mixture (8-12 hours) flow cytometry was used to find out the percent infection. This was carried out by group of Prof. Osterrieder and Dr. Walid Azab. The results demonstrated that not only sulfation content but also lateral sizes of the functionalized 2D Nanosheets, affected the viral inhibition efficiencies.

In vitro assays show then that the smaller is the TRGO-dPGS Nanosheets, the stronger is their effect in inhibition of the viral infection of cells. The TRGO-dPGS derivatives in small sizes demonstrated a greater inhibition of both viruses in comparison to the medium-sized and large-sized TRGO-dPGS or even the positive

control, acyclovir. Notably, the effect was more prominent for HSV-1 as compared to EHV-1. As anticipated, the virus infection rates remained unchanged in the presence of pristine TRGO or nonsulfated TRGO-dPG. The infection rates were comparable to those observed in the absence of any nanomaterials.

Consistent outcomes were noted for Nanodiamonds, as only sulfated ND-dPGS demonstrated the potential to inhibit both viruses, namely HSV-1 and EHV-1. On the contrary, non-sulfated ND-dPG did not manifest any effect. The size and potency of the nanodiamonds inhibition was found to be similar to that of small-sized TRGO-dPGS. [130]

Figure 4.21 to Figure 4.23, illustrate the formation of aggregates between small TRGO- dPGS and Herpesvirus particle envelopes in a PBS buffer solution as observed through SFM-QNM & SFM-QI. Force distance curves collected over the aggregates show greater deformation with setpoint forces ranging from 500pN to 2nN. Conversely, force distance curves collected over HOPG substrates near the aggregates demonstrate minimal deformation. These results suggest that the SFM tip is interacting with large, soft aggregates measuring 80-100 nm in height, likely containing soft matter. The observed deformations cannot be explained by the dPG units over TRGO, thus the aggregates are attributed to functionalized 2D Nanosheets interacting with Herpesvirus particles in solution. This corrolates well with the in vitro assays demonstrating the interaction of the virus and small TRGO-dPGS sheets and viral particles to be inhibiting infection of cell as they are mostly geometrically entrapped by multivalent functionalized 2D sheets and cannot undergo cell entry.

Based on analysis of physical and biological data, two significant factors affecting inhibitory efficiency can be identified:

The sulfation and the lateral size of the 2D Nanosheets. The correlation between sulfation content and inhibitory efficiency can be attributed to a stronger Multivalent effect resulting from higher density of negatively charged sulfate groups, allowing for stronger interactions with viral envelope proteins. As for 2D Nanosheets lateral size, much higher inhibition was observed for smaller sheets, this is attributed to be due to the required bending energy for the smaller functionalized TRGO sheet being less than that of laterally larger sheets. Membrane bending is fundamental in the endocytosis process and the presence of membrane proteins can alter the curvature of the

membrane.[146–149] However, this remodeling process requires significant energy that exceeds the binding energy gained by monovalent or limited multivalent interactions. By applying this knowledge to new Multivalent functionalized 2D Nanosheets, it is concluded that the observed size effect in viral inhibition was consistent with Reynwar et al.[150] theory that multiple binding is the essential aspect for remodeling large geometries such as cellular membranes and laterally larger Functionalized 2D carbon-based Nanosheets.

5.4. Electronic & structural characterization of 2D carbon-based Nanosheets

Scanning force microscopy in quantitative nanomechanical mapping and tunneling current (SFM-PFTUNA) was used to characterize the electronic properties of the functionalized graphene by the “[2+1] nitrene cycloaddition” functionalization method.

Experiments were carried out with the hypothesis that triazine functionalization may disrupt the free charge transport in plane of the graphene structure due to the covalent bonding disruption of the π-conjugation within the graphitic carbon rings. Therefore, measurement of the current flow through the functionalized 2D graphene sheets is indeed a property that will be affected by the covalent functionalization and a comparative study using SFM in Tunnelling and contact current (SFM-PFTUNA) measurement between Graphene, Graphene-triazine and Graphene oxide sheets would clearly and directly allow clarification of the hypothesis.

Nanographene (nG) and its functionalized variants, Nanographene-Triazine (nGTrz) and Nano graphene oxide (nGO) were experimented on and compared. In this part of the study, main discussion follows the resistivity or conductivity of the nG, nGTrz and nGO 2D carbon-based nanosheets as deposited from solvent dispersions onto an Au (111) epitaxially grown over mica substrate. Additionally, Raman spectroscopy of those Nanographene variants were carried out to understand the effect of Nitrogen content and on the disorder and doping of the 2D graphitic structures. These structures demonstrated a typical lateral dimensions between 100 to 1000 nm and that allows classification of them as 2D Nanosheets. [151]

In this study nG was produced by incubating graphite powder at 40 °C in a sodium hypochlorite solution for seven days with later purification.[132] This is considered the difference in the source of the precursor 2D carbon-based material for Triazine functionalization in compare to the TRGO material used in previous sections. According to the elemental analysis carried out by the Guday *et al*. The graphene structure produced through this method is atomically Based on the SFM-QNM height images of these structures as deposited over freshly cleaved mica, the average lateral size of the nG was found to be 68 ± 21 nm and for Triazine added variant (nGTrz) lateral sizes ranging from 74 ± 26 nm to 900 ± 100 were observed. nG demonstrated a height value of 0.58 ± 0.07 nm which was close to the observed value of height for TRGO 0.6 nm. Average thickness of nG and TRGO as 2D carbon-based Nanosheets is higher than a mechanically exfoliated Graphene layer of thickness ~0.3 nm. This implies presence of oxygen containing functional groups within the basal plane of nG similar to TRGO.

SFM-PFTUNA often provide quantified information yet it suffers from possible physicochemical modifications of the sample due to high Tunneling currents. The effect of Joule heating of the tip at high sample bias voltages at the contact area with the sample is an example of a limiting parameters in the mapping measurements. As well, the contact area of the tip, contact time between tip and sample also can reduce the maximum current measured during mapping. Additionally, variation of the sample resistivity due to inconsistencies of the conductive tape in sample preparations and thickness of the conductive substrate are complicating factors. To avoid these complexities in the experiments, a simple yet useful sample preparation was established. A replaceable control resistor is connected in series with the sample surface. This arrangement allows observation of the variation of the resistivity of the nG sheets from the overall resistivity measurable between the tip and conductive substrate and other possible influences such as ambient humidity (ambient at ≈30–45% relative humidity) and atmosphere. It is important to note that the experimental setup is, as a result, less sensitive to the tip area of contact due to the presence of the control resistor in series with the unknown sample here nG, nGO and nGTrz but the trend in resistivity variation between nG and nGTrz sheets was observed to remain unaffected.

Nanographene oxide (nGO) was produced based on a modified Hummer's oxidation method[152] and was used as a reference sample in comparison to the nG and nGTrz samples. It is known that the graphene oxide is an insulating structure due to its sp3 segments within its basal plane. Other properties of the nGO have also been well characterized in literature. [5,153,154] The nGO sheets are 43 ± 27 nm in diameter and 2.61 ± 0.84 nm in height with minimum heights of about 1 nm as measured using SFM-TM.

I–V curves of nGTrz as measured by SFM-PFTUNA demonstrate a slope of data that is useful to calculate the additional resistivity in series with the control resistor used in the experiment. Based on the I–V curve slopes (Figure 4.25B), nGTrz demonstrates a resistivity of 125 ± 50 kΩ. In comparison, resistivity of nG was found to be 345 ± 120 kΩ, and that of nGO to be significantly higher at ≈200 MΩ. The variations of resistivity within each sample correspond to their thickness, which can be observed after deposition onto Au (111) substrate interface from dispersions.

Contact current versus time (Figure 4.25A) and I–V plots show that nGO behaves as an insulating layer with higher resistivity over the Au (111) interface. This correlates with the known structural characteristics of the graphene oxide. However, Comparison between contact current versus time data of nGTrz, nG, and nGO on the Au (111) substrate presents the same trend in resistivity at constant bias (Figure 4.25A), where nGTrz demonstrates lower resistance (higher maximum currents during tip – sample contact) compared to nG and with nGO displaying the highest resistivity.

In Current vs time graphs of the nG, it is possible to observe variations of current during contact time as the tunneling current increases before retraction of the tip from its interface. I attribute this to the electrochemical changes of the sample to a lower resistivity state under the setpoint force and tunneling currents applied. However, nGTrz sheets demonstrated stability of the nGTrz sheets. Therefore, nGTrz demonstrated a stable low resistivity in compare to unstable higher resistivity of nG when subject to tunneling current of ± 60 mV sample Bias and other experimental conditions. nGTrz demonstrated a reproducible low resistivity over Gold substrates.

Moreover, Raman spectroscopy in its statistical investigation was carried out under my supervision and with suggestions within this study to address the possible doping of the nGTrz in compare to nG precursor. nG and nGTrz Raman spectra demonstrate

small variations in the defect content of the sheets. This can be due to the similarity between the lateral sizes of the nG and nGTrz Nanosheets that were exposed to the light beam during the Raman spectroscopy. Graphite powder had median diameter of 7-10 microns and nG with much smaller lateral dimensions shows only a small increase in I_D/I_G ratio as compared to the graphite starting material. I_D/I_G increased for Graphite powder from 0.19 ± 0.04 to 0.23 ± 0.01 for nG, this signifies the low number of sp^3 carbon atoms in nG structures. After functionalization of nG, nGTrz shows only a slight increase of I_D/I_G ratio to 0.29 ± 0.02, also implying that the hybridization of sp^2 the nGTrz is not significantly different from nG.

Defect estimation based on Raman spectroscopy in carbon-based 2D structures is well-established to be understood with the relation between I_D/I_G ratio for those structures. These can be used to approximate the average distance between structural inconsistencies as well as the defect density[155,156] but without any consideration for the edge effects of 2D Nanosheets. Although, the smaller size of the 2D carbon-based Nanosheets used here can create a non-representative or deviating results but the trend of data value of I_D/I_G for both nG and nGTrz is clear to show low or no defects being introduced by the functionalization of nG with Triazine.

The 2D peak of nG can be used to determine the number of graphene layers in flakes, with monolayer graphene exhibiting a FWHM of approximately 24 cm^{-1} under ambient, humid conditions.[137] However, the position and width of the peak depend on various factors such as substrate, experimental and environmental parameters, and nanometer-range strain or defects.[129,137,157] Multilayer graphene generates a weaker and broader peak, composed of four overlapping signals for bilayer and six signals for trilayer graphene, each with a FWHM of 24 cm^{-1}. For bilayer and trilayer graphene, the resulting 2D bands have a FWHM of over 40 cm^{-1} and over 60 cm^{-1}, respectively. Although four-layers graphenes follows this general trend, distinguishing between layers becomes increasingly difficult for thicker structures. [119,120,158]

nG displays a 2D peak near 2700 cm^{-1} with a FWHM of 25.8 ± 0.7 cm^{-1}, which is too narrow to arise from multilayer graphene. Less extensive purification of nG can increase the yield by including a mixed fraction of few-layer nG, which presents an FWHM of 65.0 ± 1.1 cm^{-1}, suggesting the presence of bi- and trilayer graphene.

The peak area ratio of the 2D and G bands can be used to quantitatively describe graphene materials. nG has an I_{2D}/IG ratio of 1.75 ± 0.12 (Figure 4.26), which agrees closely with reported values on the order of 2 for pristine graphene measured under ambient conditions. In contrast, the I_{2D}/I_G ratio of nGTrz is significantly lower (1.04 ± 0.07), indicating a doped graphene material (Figure 4.26C).[159,160] Furthermore, plotting the position of the 2D band against the position of the G band and assigning a linear fit shows that the distribution for nG follows a slope of 1.19 ± 0.17, while modified nGTrz falls along a slope of 0.58 ± 0.09. It has been previously reported that the slope will shift higher due to mechanical strain, approaching about 2.2, while doping decreases the slope toward 0.6.[128] Thus, upon modification, nGTrz behaves as a doped graphene material. Doping effects can be observed when a heteroatom is conjugated with the π-conjugated system of graphene, as has been reported with carbon nanotubes. [161]

Based on the experimental results of SFM-PFTUNA & statistical Raman spectroscopy, nGTrz, behaves similar to a doped graphene layer. This is achieved by conjugating a heteroatom with the π-conjugated system of graphene, which is possible when the nitrogen-containing three-membered rings of nGTrz are in an open form. Therefore, the covalent functionalization of nGTrz does not impair the π-system's conjugated nature, and the involved carbon atoms retain their sp^2 character. These findings are supported by computational results and previous reports on carbon nanotubes (Figure 5.1).

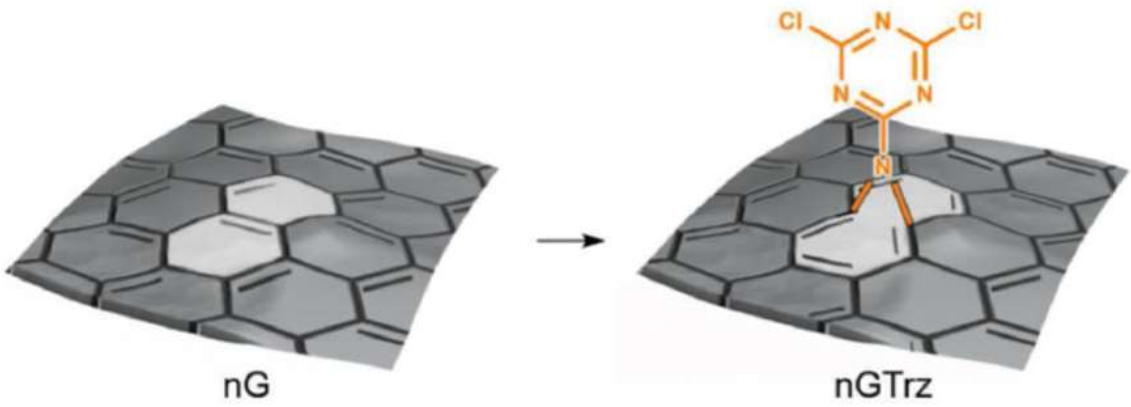

Figure 5.1, The carbon atoms in the cycloaddition reaction site are sp2 hybridized after functionalization, maintaining the aromaticity of the system. Adopted from reference [132]

5.5. Triazine and carbon-based two-Dimensional Materials

Scanning force microscopy was initially used to address the question, what is the conformation of the Triazine (Carbon-Nitrogen) based structures in a metal assisted and solvent mediated synthesis. Although the Triazine based structures has been subject to many studies on their physicochemical properties previously [162–166]. Reactions for synthesis of Triazine based structures often take place at very high temperatures and this leads to partial carbonization and undefined structures, lack of a band gap or other useful optoelectronics.[167] Therefore, in this section of the thesis, results of a new strategy of synthesis for Triazine structures are investigated and characterized. This novel synthesis method is based on reaction of the Triazine and calcium carbide in anhydrous dimethylformamide (DMF) at relatively low temperature of 120 ºC. Additionally, to understand the role of water, reaction of Triazine and Calcium carbide was carried out also in presence of water at room temperature and another reaction in Non-dry DMF at 120 ºC.

Scanning force microscopy in quantitative imaging and quantitative nanomechanical mapping were used to observe and characterize the product of the reaction product of Triazine and calcium carbide. Figure 4.27, demonstrates the SFM - QNM height images of the product of the reaction of Triazine with Calcium carbide under anhydrous reaction conditions at 120 ºC. As it can be seen, the topography of the 2DTSs structure demonstrate plateaus and Terraces with occasional wrinkles and blackfolds. This observation of topography implies the covalent and self-avoiding nature of those structures [7,45] which may be simulated on a macroscale using a sheet of A4 paper (Figure 5.3) for 2DTSs observed in Figure 4.27 B. This does not only demonstrate high flexibility in the 2DTSs structures but also is a direct consequence of the strong covalent bonding in a 2D network. This characteristic of the observed 2DTSs also is in contrast with the self-assembled 2D structures based on lipid bilayers & membranes, as those structures can self-penetrate and reconfigure back to a single layer rather than remaining stable in a folded state. [133]

The folding possibility is mainly due to the gain in energy of the system by bending and remaining stable. This is often achieved by energy gain through van der Waals interlayer forces as also seen within layers of a crystal. The folding may often

be triggered by the process if drying during surface deposition of the 2D Nanosheets.[45]

Laterally smaller and thinner 2D structures could also be found present at interface of the plateaus and terraces (Figure 4.27 A & Figure 4.29), with lateral dimensions not larger than 200 nm and thickness of 0.5 nm. Since the thickness of the observed 2DTSs layers as deposited onto the mica interface were often between 5 and 10 nm, we believe that we did not observe a single-layer exfoliation of the layered structures in most cases and the laterally smaller 2D structures are pieces separated from the larger plateaus during ultrasonication processes carried out before sample deposition on the mica substrates.

To prove the role of Calcium within the synthesis reaction, monovalent metal such as sodium present in sodium carbonate was added to the reaction medium. The reaction between Triazine and calcium carbide was performed in DMF and in the presence of EDTA chelating agent or sodium carbonate, no 2D structure was achieved as it can be seen in the Figure 4.30. This is due to the production of sodium carbonate and the absence of any driving force to conjugate monomers in a sheet like manner. Therefore, the 2D nature of 2DTSs structures are assigned to the influenced growth in two dimensions due to presence of Calcium.

Above mentioned observation of the SFM was further corroborated by the computational modelling based on Density Functional Theory (DFT) in the GPAW program[168–170]. These analysis was carried out by the group of Prof. Beate Paulus. In that theoretical work, Coordination of one or two calcium ions with nitrogen atoms of the triazine rings in an intermediate compound shown in Figure 5.2 was simulated and any rotation around the C1−C2 and C3−C4 bonds caused 0.05 and 1.6 eV barrier energy, respectively (Figure 5.2B). Those energy barriers are the main forces acting on growing triazine-benzene structures in 2D. It has been discussed in the literature that, calcium ions are able to form complexes with nitrogen-containing ligands.[171,172] this is while interactions between these ligands and calcium ions are not as strong as those of oxygen-containing ligands,[173,174] they are able to induce enough rigidity for the two-dimensional coupling of monomers.[168–170] The weakness of the interactions, on the other hand, enables the metal ions to be removed completely from the final product if needed.

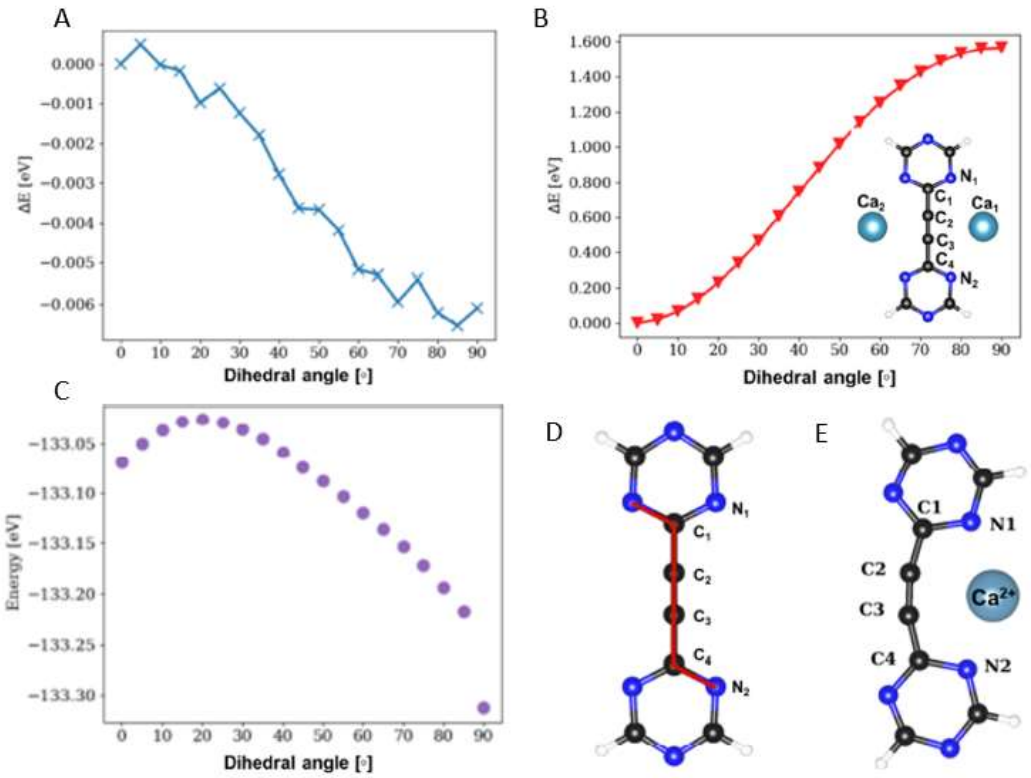

Figure 5.2, Simulated structure of the model compound coordinated with two calcium ions. A) DFT energy difference ΔE = E - E [dihedral angle = 0°] of the system against the dihedral angle with 5° each step for the free model structure shown in (D). B) the total energy of the system with different dihedral angles with a step size of 5°. C) DFT energy difference of the system with one coordinated $Ca2^{+}$ atom. D) considered dihedral angle is marked with red line. Calculations were performed on the PBE/dzp level of accuracy. E) considered dihedral angle. Adapted from reference [133]

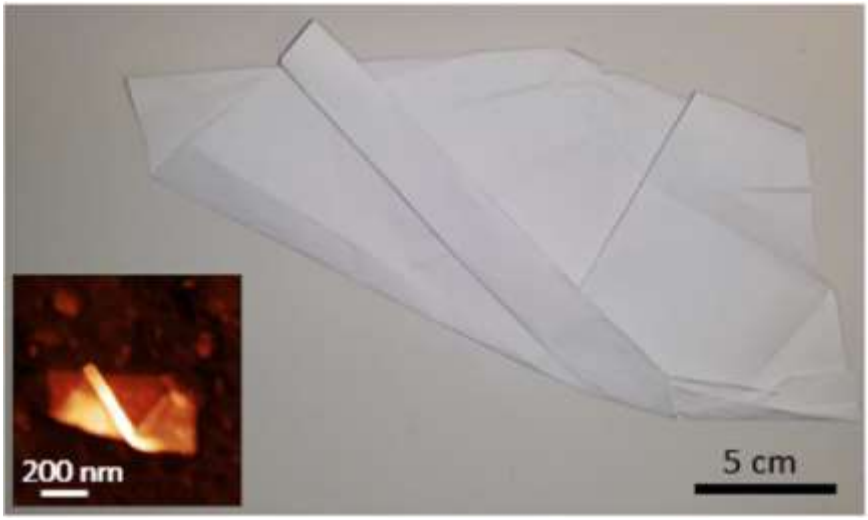

Figure 5.3, Macroscale model of a folded and wrinkled 2DTSs as seen in the inset SFM-QNM height image of the 2DTSs Nanosheet. Adapted from reference [133].

In order to further understand the structure of the 2DTSs, characterization of the synthesized materials through investigation of their polymorphism and crystallinity was carried out. Raman spectra were individually evaluated and mapped for 2DTSs products (Figure 4.32 and Figure 4.31).

The G peaks of 2DTSs and GM were detected at 1562 and 1582 cm^{-1}, respectively. In the case of 2DTSs, broadening of Raman peaks ranging from 1320−1360 cm^{-1} was noted, with a center at 1345 cm^{-1}. The peaks ranging from 1550−1620 cm^{-1}, with a noticeable peak at 1562−1565 cm^{-1}, were also observed. The vibrational frequencies of C=N and C=C are analogous within the 1000−2000 cm^{-1} range, as previously reported by Ferrari et al.[175] The C=N vibrational frequencies are very similar to the C=C frequencies within the 1000−2000 cm^{-1} range and this has been also observed and modelled previously within the literature.[176] Consequently, the peaks observed in the Raman spectra of 2DTSs were assigned to a structure containing nitrogen atoms, as substantiated by the elemental analysis. Furthermore, the G peak position in the Raman spectra shifted with the nitrogen content of the product when visible laser light was used. For instance, a G peak at 1560−1565 cm^{-1} was detected for a product with 20−30% nitrogen content, consistent with literature data.[121] This downshift in comparison to the G peak of HOPG was ascribed to the difference between the GM composition and HOPG.[175]

The correlation between this shift and the nitrogen content of the materials is further evidence of the preparation of 2DTSs under anhydrous conditions. 2DTSs/GM mixtures exhibited Raman bands at ∼1332 and ∼1564 cm^{-1}, along with an occasional weak and broad band at ∼1610−1620 cm^{-1}, in addition to a broad band centered at ∼2700 cm^{-1} (Figure 4.32). The Raman bands at ∼1345 and ∼1620 cm^{-1}, corresponding to the D peak, were assigned to the domain boundaries or nucleation sites within the structure. Conversely, the D′ peak observed occasionally at ∼1620 cm^{-1} suggested doping by a heteroatom, suggesting nitrogen atoms of triazine in the structure of 2DTSs (Figure 4.32). Notably, no band at ∼2100 cm^{-1} was detected in the spectrum of 2DTSs, providing further evidence of the trimerization of triple bonds, in agreement with Infrared spectroscopy and NMR spectra [177,178].

2DTSs demonstrated a maximum UV absorption at 235−276 nm corresponding to n → π* transitions. Due to their large π-conjugated system, 2DTSs were able to produce singlet oxygen under irradiation with a near-infrared (NIR) laser (808 nm) as well as 638 nm wavelength of laser. 2DTSs released singlet oxygen with a higher production rate, in comparison to methylene blue [179,180] as observed by the absorbance change of DPBF, in a similar solvent. This characteristic is useful for various applications ranging from photodynamic therapy to photocatalyst.

Chapter 6

6. Summary and Outlook

In summary, this thesis demonstrates the development of new structures based on carbon 2D Nanomaterials, namely Graphene modified covalently with multivalent functional groups on the bases of Triazine and Polyglycerols. I addressed the physical characteristics of the well-defined and tailored multivalent active interfaces mimicking extracellular matrix of the cell. Using controlled functionalization of graphene sheets, in both “Graft to” and “Graft from”, interfaces capable of binding with viral particles for viral inhibitions were created and their topography and covalently modified structures were investigated. Moreover, the SFM in quantitative nanomechanical mapping, SFM-PFTUNA and Raman spectroscopy were demonstrated to be the suitable characterization methodologies of topography, electronics, structural order and the interactions of the multivalent functionalized 2D carbon-based nanomaterials with biologically relevant interfaces.

“Graft to” methodology based on the [2+1] nitrene cycloaddition reactions is a relatively mild method for the controlled covalent functionalization of TRGO. This method also further allows controlled & stepwise attachment of similar of different molecules to the Triazine structure. Functionalized graphene sheets can be transformed into defined 2D surfaces by stepwise post-modification in high yields. The advantage of this method is the construction of bifunctional carbon nanomaterials with controlled ligand densities, which even allows the conjugation of sensitive bio(macro)molecules at room temperature.

Upon high density functionalization by a heparin sulfate post-functionalization, Graphene Nanosheets can be changed from inert surfaces to highly active interfaces for virus binding. A 2D material consisting of 6% graphene and 94% sulfated polyglycerol could trap 20 VSV virions as observed via scanning force microscopy and Cryo-transmission electron microscopy. These data highlight the versatility of graphene as a flexible material for promoting viral infection (TRGO-PGShigh). The in vitro assays showed potent binding of TRGO-PGShigh toward VSV at low μg mL^{-1} concentrations, in contrast to hundred times higher concentrations needed for TRGO-PGhigh to have a substantial interaction with VSV. Therefore, the sulfated variant (TRGO-Trz-hPGShigh), might be relevant for the improvement of vaccines or

supporting the delivery of gene therapeutic vectors and active interfaces of filtration of water.

“Graft from” covalent functionalization based on ROMP was demonstrated to be also capable of creating active interfaces upon sulfation post functionalization. The main difference was found to be the smaller overall thickness of the TRGO-dPGS in compare to the TRGO-Trz-hPGS structures which is attributed to lack of presence of Triazine structures and the variation of average molecular weight (diameter of dPG) for the dendritic polyglycerols grafted from TRGO functionalities in compare to pre-synthesized hyperbranched polyglycerols grafted to the TRGO-Trz. The structural differences also contain variance in the density of the multivalent functional sites. Moreover, the size of the TRGO-dPGS was found to be critical parameter in defining the efficiency of interaction with viral enveloped models as observed in *in vitro* assays and the Scanning force microscopy investigation of the TRGO-dPGS sheets combined with viral particles in buffer solution. It was observed that soft aggregates of the TRGO-dPGS were formed within the solution mixture that imply entrapment of the viral particles possibly by envelopment, since otherwise the similarly charged TRGO-dPGS Nanoshhets do not aggregate in solution. This envelopment process can be further studied using Cryo-TEM in future to understand the details of the interactions between the sulfated multivalent sites of 2D Nanosheets and the envelope proteins of the viral particles.

Furthermore, NanoGraphene (nG) sheets functionalized with Triazine via “Graft to” method showed doping effects as observed via SFM-PFTUNA in correlation with statistical Raman spectroscopy. nGTrz demonstrated that the cycloaddition reaction between the triazine functional group and graphene is a consequence of an opened [4.4.1] bicyclic structure. The doping effect of Triazine functionalization was then attributed to be by the nitrogen atoms acting as a dopant that is integrated into the π-conjugated system of nG. Thus, the observed doping effects necessitate the opening of the aziridine ring and restoration of extended aromaticity. Furthermore, this conjugated dopant introduces geometric irregularities or wrinkles that give nGTrz a crystalline structure while retaining the sp^2 characteristics of graphene. This is a unique combination of functionalization possibilities and while retaining electronic properties of 2D carbon-based structures like graphene. The intrinsic properties of the Nano Graphene sheets make them a great platform for the conductive ink materials and

printed electronics, while Graphene with Triazine functionalizations provide low resistance benefit in addition to capability of higher degrees of interface functionalities and larger design freedom. A range of applications including but not limited to thermal interface materials, coating for specialized sensor could be then considered.

At last, this work demonstrated with a mechanistic study using scanning force microscopy and Raman spectroscopy that it is possible to synthesize 2D crystalline and polycrystalline carbon-based structures containing Triazine groups. The metal assisted route to forcing growth of Triazine in 2D plane and without a template in a 3D reactor using calcium ions works. Moreover, it was revealed water content within the synthesis process has large effect on the reaction route, and in the presence of water, graphitic material was created. Due to its interesting physicochemical properties, straightforward synthesis, and cheap precursors, the presented two-dimensional nanomaterial is a promising candidate for a wide range of future applications, including photodynamic therapy methods as it can be used to create surfaces capable of release of singlet oxygen.

7. References

1. Vonnemann, J. *et al.* Virus inhibition induced by polyvalent nanoparticles of different sizes. *Nanoscale* **6**, 2353–2360 (2014).

2. Geim, A. K. & Novoselov, K. S. The rise of graphene. *Nat. Mater.* **6**, 183–191 (2007).

3. Novoselov, K. S. *et al.* Electric field effect in atomically thin carbon films. *Science* **306**, 666–669 (2004).

4. Zhang, J. *et al.* Free Folding of Suspended Graphene Sheets by Random Mechanical Stimulation. *Phys. Rev. Lett.* **104**, 166805 (2010).

5. Guo, F. *et al.* Hydration-Responsive Folding and Unfolding in Graphene Oxide Liquid Crystal Phases. *ACS Nano* **5**, 8019–8025 (2011).

6. Meng, X., Li, M., Kang, Z., Zhang, X. & Xiao, J. Mechanics of self-folding of single-layer graphene. *J. Phys. Appl. Phys.* **46**, 055308 (2013).

7. Chen, X., Zhang, L., Zhao, Y., Wang, X. & Ke, C. Graphene folding on flat substrates. *J. Appl. Phys.* **116**, 164301 (2014).

8. Hallam, T. *et al.* Controlled Folding of Graphene: GraFold Printing. *Nano Lett.* **15**, 857–863 (2015).

9. Morales-Narváez, E., Hassan, A.-R. & Merkoçi, A. Graphene Oxide as a Pathogen-Revealing Agent: Sensing with a Digital-Like Response. *Angew. Chem. Int. Ed.* **52**, 13779–13783 (2013).

10. Song, Z. *et al.* Virus capture and destruction by label-free graphene oxide for detection and disinfection applications. *Small Weinh. Bergstr. Ger.* **11**, 1171–1176 (2015).

11. Perreault, F., de Faria, A. F., Nejati, S. & Elimelech, M. Antimicrobial Properties of Graphene Oxide Nanosheets: Why Size Matters. *ACS Nano* **9**, 7226–7236 (2015).

12. Ye, S. *et al.* Antiviral Activity of Graphene Oxide: How Sharp Edged Structure and Charge Matter. *ACS Appl. Mater. Interfaces* **7**, 21571–21579 (2015).

13. Chen, J. *et al.* Graphene oxide exhibits broad-spectrum antimicrobial activity against bacterial phytopathogens and fungal conidia by intertwining and membrane perturbation. *Nanoscale* **6**, 1879–1889 (2014).

14. Akhavan, O., Choobtashani, M. & Ghaderi, E. Protein Degradation and RNA Efflux of Viruses Photocatalyzed by Graphene–Tungsten Oxide Composite Under Visible Light Irradiation. *J. Phys. Chem. C* **116**, 9653–9659 (2012).

15. Liu, S. *et al.* Antibacterial Activity of Graphite, Graphite Oxide, Graphene Oxide, and Reduced Graphene Oxide: Membrane and Oxidative Stress. *ACS Nano* **5**, 6971–6980 (2011).

16. Akhavan, O. & Ghaderi, E. Toxicity of Graphene and Graphene Oxide Nanowalls Against Bacteria. *ACS Nano* **4**, 5731–5736 (2010).

17. Akhavan, O. & Ghaderi, E. Escherichia coli bacteria reduce graphene oxide to bactericidal graphene in a self-limiting manner. *Carbon* **50**, 1853–1860 (2012).

18. Ting, S. S., Chen, G. & Stenzel, M. H. Synthesis of glycopolymers and their multivalent recognitions with lectins. *Polym. Chem.* **1**, 1392–1412 (2010).

19. Fasting, C. *et al.* Cover Picture: Multivalency as a Chemical Organization and Action Principle (Angew. Chem. Int. Ed. 42/2012). *Angew. Chem. Int. Ed.* **51**, 10419–10419 (2012).

20. Bhatia, S., Camacho, L. C. & Haag, R. Pathogen inhibition by multivalent ligand architectures. *J. Am. Chem. Soc.* **138**, 8654–8666 (2016).

21. Alexander, P. A., He, Y., Chen, Y., Orban, J. & Bryan, P. N. A minimal sequence code for switching protein structure and function. *Proc. Natl. Acad. Sci.* **106**, 21149–21154 (2009).

22. Nick Pace, C., Scholtz, J. M. & Grimsley, G. R. Forces stabilizing proteins. *FEBS Lett.* **588**, 2177–2184 (2014).

23. Fasting, C. *et al.* Multivalency as a Chemical Organization and Action Principle. *Angew. Chem. Int. Ed.* **51**, 10472–10498 (2012).

24. Graham, B. S. & Sullivan, N. J. Emerging viral diseases from a vaccinology perspective: preparing for the next pandemic. *Nat. Immunol.* **19**, 20–28 (2018).

25. Morens, D. M., Folkers, G. K. & Fauci, A. S. Emerging infections: a perpetual challenge. *Lancet Infect. Dis.* **8**, 710–719 (2008).

26. Pekosz, A. & Glass, G. E. Emerging viral diseases. *Md. Med. MM Publ. MEDCHI Md. State Med. Soc.* **9**, 11, 13–16 (2008).

27. M. Boltovets, P., M. Polischuk, O., G. Kovalenko, O. & A. Snopok, B. A simple SPR-based method for the quantification of the effect of potential virus inhibitors. *Analyst* **138**, 480–486 (2013).

28. Chiodi, E., Marn, A., Geib, M. & ünlü, M. S. The Role of Surface Chemistry in the Efficacy of Protein and DNA Microarrays for Label-Free Detection: An Overview. *Polymers* **13**, 1026 (2021).

29. Antiviral potential of nanomaterials: The fight against viruses. in *Antimicrobial Activity of Nanoparticles* 101–132 (Elsevier, 2023). doi:10.1016/B978-0-12-821637-8.00005-5.

30. Payne, S. Methods to Study Viruses. *Viruses* 37–52 (2017) doi:10.1016/B978-0-12-803109-4.00004-0.

31. Riss, T. L. *et al.* Cell Viability Assays. in *Assay Guidance Manual* (eds. Markossian, S. et al.) (Eli Lilly & Company and the National Center for Advancing Translational Sciences, Bethesda (MD), 2004).

32. Gholami, M. F. *et al.* Functionalized Graphene as Extracellular Matrix Mimics: Toward Well-Defined 2D Nanomaterials for Multivalent Virus Interactions. *Adv. Funct. Mater.* **27**, 1606477 (2017).

33. The Nobel Prize in Physics 2010. *NobelPrize.org* https://www.nobelprize.org/prizes/physics/2010/summary/.

34. Le, N. B. & Woods, L. M. Folded graphene nanoribbons with single and double closed edges. *Phys. Rev. B* **85**, 035403 (2012).

35. Ghosh, S. *et al.* Extremely high thermal conductivity of graphene: Prospects for thermal management applications in nanoelectronic circuits. *Appl. Phys. Lett.* **92**, 151911 (2008).

36. Nair, R. R. *et al.* Fine structure constant defines visual transparency of graphene. *Science* **320**, 1308 (2008).

37. Cai, W., Zhu, Y., Li, X., Piner, R. D. & Ruoff, R. S. Large area few-layer graphene/graphite films as transparent thin conducting electrodes. *Appl. Phys. Lett.* **95**, 123115 (2009).

38. Dorn, M., Lange, P., Chekushin, A., Severin, N. & Rabe, J. P. High contrast optical detection of single graphenes on optically transparent substrates. *J. Appl. Phys.* **108**, 106101 (2010).

39. Lee, C., Wei, X., Kysar, J. W. & Hone, J. Measurement of the elastic properties and intrinsic strength of monolayer graphene. *Science* **321**, 385–388 (2008).

40. Adetayo, A. & Runsewe, D. Synthesis and Fabrication of Graphene and Graphene Oxide: A Review. *Open J. Compos. Mater.* **9**, 207–229 (2019).

41. Lange, P., Dorn, M., Severin, N., Vanden Bout, D. A. & Rabe, J. P. Single- and Double-Layer Graphenes as Ultrabarriers for Fluorescent Polymer Films. *J. Phys. Chem. C* **115**, 23057–23061 (2011).

42. Sreeprasad, T. S. & Berry, V. How Do the Electrical Properties of Graphene Change with its Functionalization? *Small* **9**, 341–350 (2013).

43. Beléndez, T., Neipp, C. & Beléndez, A. Large and small deflections of a cantilever beam. *Eur. J. Phys.* **23**, 371–379 (2002).

44. Lu, Q., Arroyo, M. & Huang, R. Elastic bending modulus of monolayer graphene. *J. Phys. Appl. Phys.* **42**, 102002 (2009).

45. Gholami, M. F., Severin, N. & Rabe, J. P. *Folding of Graphene and Other Two-Dimensional Materials*. (transcript, 2016).

46. Neto, A. C., Guinea, F., Peres, N. M., Novoselov, K. S. & Geim, A. K. The electronic properties of graphene. *Rev. Mod. Phys.* **81**, 109 (2009).

47. Warner, J. H., Schaffel, F., Rummeli, M. & Bachmatiuk, A. *Graphene: Fundamentals and Emergent Applications*. (Newnes, 2012).

48. Avouris, P. Graphene: Electronic and Photonic Properties and Devices. *Nano Lett.* **10**, 4285–4294 (2010).

49. Park, S. & Ruoff, R. S. Chemical methods for the production of graphenes. *Nat. Nanotechnol.* **4**, 217–224 (2009).

50. Hummers, W. S. & Offeman, R. E. Preparation of Graphitic Oxide. *J. Am. Chem. Soc.* **80**, 1339–1339 (1958).

51. Dreyer, D. R., Park, S., Bielawski, C. W. & Ruoff, R. S. The chemistry of graphene oxide. *Chem. Soc. Rev.* **39**, 228–240 (2009).

52. Dreyer, D. R., Ruoff, R. S. & Bielawski, C. W. From Conception to Realization: An Historial Account of Graphene and Some Perspectives for Its Future. *Angew. Chem. Int. Ed.* **49**, 9336–9344 (2010).

53. Lerf, A., He, H., Forster, M. & Klinowski, J. Structure of Graphite Oxide Revisited. *J. Phys. Chem. B* **102**, 4477–4482 (1998).

54. He, H., Klinowski, J., Forster, M. & Lerf, A. A new structural model for graphite oxide. *Chem. Phys. Lett.* **287**, 53–56 (1998).

55. Gao, W., Alemany, L. B., Ci, L. & Ajayan, P. M. New insights into the structure and reduction of graphite oxide. *Nat. Chem.* **1**, 403–408 (2009).

56. Eda, G., Mattevi, C., Yamaguchi, H., Kim, H. & Chhowalla, M. Insulator to Semimetal Transition in Graphene Oxide. *J. Phys. Chem. C* **113**, 15768–15771 (2009).

57. Yan, J.-A. & Chou, M. Y. Oxidation functional groups on graphene: Structural and electronic properties. *Phys. Rev. B* **82**, 125403 (2010).

58. Stankovich, S. *et al.* Graphene-based composite materials. *Nature* **442**, 282–286 (2006).

59. Gómez-Navarro, C. *et al.* Electronic Transport Properties of Individual Chemically Reduced Graphene Oxide Sheets. *Nano Lett.* **7**, 3499–3503 (2007).

60. Rezania, B., Severin, N., Talyzin, A. V. & Rabe, J. P. Hydration of bilayered graphene oxide. *Nano Lett.* **14**, 3993–3998 (2014).

61. Boehm, H. P., Setton, R. & Stumpp, E. Nomenclature and terminology of graphite intercalation compounds (IUPAC Recommendations 1994). *Pure Appl. Chem.* **66**, 1893–1901 (1994).

62. Wu, J., Pisula, W. & Müllen, K. Graphenes as Potential Material for Electronics. *Chem. Rev.* **107**, 718–747 (2007).

63. Fan, X. *et al.* Deoxygenation of Exfoliated Graphite Oxide under Alkaline Conditions: A Green Route to Graphene Preparation. *Adv. Mater.* **20**, 4490–4493 (2008).

64. McAllister, M. J. *et al.* Single Sheet Functionalized Graphene by Oxidation and Thermal Expansion of Graphite. *Chem. Mater.* **19**, 4396–4404 (2007).

65. Blackman, L. C. F. & Ubbelohde, A. R. J. P. Stress recrystallization of graphite. *Proc. R. Soc. Lond. Ser. Math. Phys. Sci.* **266**, 20–32 (1962).

66. Kozbial, A. *et al.* Study on the Surface Energy of Graphene by Contact Angle Measurements. *Langmuir* **30**, 8598–8606 (2014).

67. Konkolewicz, D., Monteiro, M. J. & Perrier, S. Dendritic and Hyperbranched Polymers from Macromolecular Units: Elegant Approaches to the Synthesis of Functional Polymers. *Macromolecules* **44**, 7067–7087 (2011).

68. Haag, R., Sunder, A. & Stumbé, J.-F. An approach to glycerol dendrimers and pseudo-dendritic polyglycerols. *J. Am. Chem. Soc.* **122**, 2954–2955 (2000).

69. Sunder, A., Hanselmann, R., Frey, H. & Mülhaupt, R. Controlled synthesis of hyperbranched polyglycerols by ring-opening multibranching polymerization. *Macromolecules* **32**, 4240–4246 (1999).

70. Wilms, D., Stiriba, S.-E. & Frey, H. Hyperbranched Polyglycerols: From the Controlled Synthesis of Biocompatible Polyether Polyols to Multipurpose Applications. *Acc. Chem. Res.* **43**, 129–141 (2010).

71. Svenson, S. & Tomalia, D. A. Dendrimers in biomedical applications--reflections on the field. *Adv. Drug Deliv. Rev.* **57**, 2106–2129 (2005).

72. Haag, R. & Kratz, F. Polymer Therapeutics: Concepts and Applications. *Angew. Chem. Int. Ed.* **45**, 1198–1215 (2006).

73. Roizman, B. The family Herpesviridae: a brief introduction. *Fields Virol.* (2001).

74. Grunewald, K. *et al.* Three-dimensional structure of herpes simplex virus from cryo-electron tomography. *Science* **302**, 1396–1398 (2003).

75. Zhou, Z. H. *et al.* Seeing the herpesvirus capsid at 8.5 Å. *Science* **288**, 877–880 (2000).

76. Brown, J. C. & Newcomb, W. W. Herpesvirus capsid assembly: insights from structural analysis. *Curr. Opin. Virol.* **1**, 142–149 (2011).

77. Laquerre, S. *et al.* Heparan sulfate proteoglycan binding by herpes simplex virus type 1 glycoproteins B and C, which differ in their contributions to virus attachment, penetration, and cell-to-cell spread. *J. Virol.* **72**, 6119–6130 (1998).

78. Mårdberg, K., Trybala, E., Glorioso, J. C. & Bergström, T. Mutational analysis of the major heparan sulfate-binding domain of herpes simplex virus type 1 glycoprotein C. *J. Gen. Virol.* **82**, 1941–1950 (2001).

79. Johnson, C. A. *et al.* Orientation determination in the 3D reconstruction of icosahedral viruses using a parallel computer. in *Supercomputing'94: Proceedings of the 1994 ACM/IEEE Conference on Supercomputing* 550–559 (IEEE, 1994).

80. Ge, P. *et al.* Cryo-EM model of the bullet-shaped vesicular stomatitis virus. *Science* **327**, 689–693 (2010).

81. Green, T. J., Zhang, X., Wertz, G. W. & Luo, M. Structure of the vesicular stomatitis virus nucleoprotein-RNA complex. *Science* **313**, 357–360 (2006).

82. Lichty, B. D., Power, A. T., Stojdl, D. F. & Bell, J. C. Vesicular stomatitis virus: re-inventing the bullet. *Trends Mol. Med.* **10**, 210–216 (2004).

83. Stojdl, D. F. *et al.* VSV strains with defects in their ability to shutdown innate immunity are potent systemic anti-cancer agents. *Cancer Cell* **4**, 263–275 (2003).

84. Coldham, I. & Hufton, R. Intramolecular dipolar cycloaddition reactions of azomethine ylides. *Chem. Rev.* **105**, 2765–2810 (2005).

85. Chua, C. K. & Pumera, M. Covalent chemistry on graphene. *Chem. Soc. Rev.* **42**, 3222–3233 (2013).

86. Sakellariou, G., Ji, H., Mays, J. W., Hadjichristidis, N. & Baskaran, D. Controlled Covalent Functionalization of Multiwalled Carbon Nanotubes using [4 + 2] Cycloaddition of Benzocyclobutenes. *Chem. Mater.* **19**, 6370–6372 (2007).

87. Kumar, I., Rana, S. & Cho, J. W. Cycloaddition Reactions: A Controlled Approach for Carbon Nanotube Functionalization. *Chem. – Eur. J.* **17**, 11092–11101 (2011).

88. Faghani, A. Synthesis and controlled non-destructive covalent functionalization of low-dimensional carbon nanomaterials. (2020) doi:10.17169/refubium-26965.

89. Schwartz, E. *et al.* Synthesis, Characterization, and Surface Initiated Polymerization of Carbazole Functionalized Isocyanides. *ACS Publications* https://pubs.acs.org/doi/pdf/10.1021/cm903664g (2010) doi:10.1021/cm903664g.

90. Zhao, L. *et al.* Chromatographic Separation of Highly Soluble Diamond Nanoparticles Prepared by Polyglycerol Grafting. *Angew. Chem. Int. Ed.* **50**, 1388–1392 (2011).

91. Donskyi, I., Achazi, K., Wycisk, V., Böttcher, C. & Adeli, M. Synthesis, self-assembly, and photocrosslinking of fullerene-polyglycerol amphiphiles as nanocarriers with controlled transport properties. *Chem. Commun.* **52**, 4373–4376 (2016).

92. Ziem, B. Polyvalent Virus Inhibitors Based on Functionalized Carbon Nanoarchitectures. (2017) doi:10.17169/refubium-8233.

93. Türk, H., Haag, R. & Alban, S. Dendritic polyglycerol sulfates as new heparin analogues and potent inhibitors of the complement system. *Bioconjug. Chem.* **15**, 162–167 (2004).

94. Blotny, G. Recent applications of 2,4,6-trichloro-1,3,5-triazine and its derivatives in organic synthesis. *Tetrahedron* **62**, 9507–9522 (2006).

95. Christenson, H. K. & Thomson, N. H. The nature of the air-cleaved mica surface. *Surf. Sci. Rep.* **71**, 367–390 (2016).

96. Fukuma, T., Ueda, Y., Yoshioka, S. & Asakawa, H. Atomic-Scale Distribution of Water Molecules at the Mica-Water Interface Visualized by Three-Dimensional Scanning Force Microscopy. *Phys. Rev. Lett.* **104**, 016101 (2010).

97. Faghani, A. *et al.* Controlled Covalent Functionalization of Thermally Reduced Graphene Oxide To Generate Defined Bifunctional 2D Nanomaterials. *Angew. Chem. Int. Ed.* **56**, 2675–2679 (2017).

98. Craig, B. D. & Anderson, D. S. *Handbook of Corrosion Data*. (ASM international, 1994).

99. Binnig, G., Quate, C. F. & Gerber, Ch. Atomic Force Microscope. *Phys. Rev. Lett.* **56**, 930–933 (1986).

100. Binnig, G. & Rohrer, H. Scanning tunneling microscopy---from birth to adolescence. *Rev. Mod. Phys.* **59**, 615–625 (1987).

101. Overney, R. & Meyer, E. Tribological Investigations Using Friction Force Microscopy. *MRS Bull.* **18**, 26–35 (1993).

102. Liu, W., Bonin, K. & Guthold, M. Easy and direct method for calibrating atomic force microscopy lateral force measurements. *Rev. Sci. Instrum.* **78**, 063707 (2007).

103. Sheng, Czajkowsky, & Shao. AFM tips: how sharp are they? *J. Microsc.* **196**, 1–5 (1999).

104. Phys. Rev. B 81, 054302 (2010) - Dynamical characterization of vibrating AFM cantilevers forced by photothermal excitation. https://journals.aps.org/prb/abstract/10.1103/PhysRevB.81.054302.

105. Severin, N. *et al.* Atomic resolution with high-eigenmode tapping mode atomic force microscopy. *Phys. Rev. Res.* **4**, 023149 (2022).

106. Nemes-Incze, P., Osváth, Z., Kamarás, K. & Biró, L. P. Anomalies in thickness measurements of graphene and few layer graphite crystals by tapping mode atomic force microscopy. *Carbon* **46**, 1435–1442 (2008).

107. Heinz, W. F. & Hoh, J. H. Spatially resolved force spectroscopy of biological surfaces using the atomic force microscope. *Trends Biotechnol.* **17**, 143–150 (1999).

108. Tschoegl, N. W. *The Phenomenological Theory of Linear Viscoelastic Behavior: An Introduction*. (Springer Science & Business Media, 2012).

109. Garcia, R. Nanomechanical mapping of soft materials with the atomic force microscope: methods, theory and applications. *Chem. Soc. Rev.* **49**, 5850–5884 (2020).

110. Weisenhorn, A. L., Khorsandi, M., Kasas, S., Gotzos, V. & Butt, H.-J. Deformation and height anomaly of soft surfaces studied with an AFM. *Nanotechnology* **4**, 106 (1993).

111. Derjaguin, B. V., Muller, V. M. & Toporov, Yu. P. Effect of contact deformations on the adhesion of particles. *J. Colloid Interface Sci.* **53**, 314–326 (1975).

112. Pfreundschuh, M., Martinez-Martin, D., Mulvihill, E., Wegmann, S. & Muller, D. J. Multiparametric high-resolution imaging of native proteins by force-distance curve–based AFM. *Nat. Protoc.* **9**, 1113–1130 (2014).

113. Wang, Y., Alsmeyer, D. C. & McCreery, R. L. Raman spectroscopy of carbon materials: structural basis of observed spectra. *Chem. Mater.* **2**, 557–563 (1990).

114. Raman, C. V. & Krishnan, K. S. A New Type of Secondary Radiation. *Nature* **121**, 501–502 (1928).

115. Atkins, P., Paula, J. de & Friedman, R. *Physical Chemistry: Quanta, Matter, and Change*. (OUP Oxford, 2014).

116. Dresselhaus, M. S., Dresselhaus, G., Saito, R. & Jorio, A. Raman spectroscopy of carbon nanotubes. *Phys. Rep.* **409**, 47–99 (2005).

117. Scenev, V. Electronic properties of graphene and other carbon-based hybrid materials for flexible electronics. (Humboldt-Universität zu Berlin, Mathematisch-Naturwissenschaftliche Fakultät, 2014). doi:10.18452/17069.

118. Orlando, A. *et al.* A Comprehensive Review on Raman Spectroscopy Applications. *Chemosensors* **9**, 262 (2021).

119. Ferrari, A. C. *et al.* Raman Spectrum of Graphene and Graphene Layers. *Phys. Rev. Lett.* **97**, 187401 (2006).

120. Malard, L. M., Pimenta, M. A., Dresselhaus, G. & Dresselhaus, M. S. Raman spectroscopy in graphene. *Phys. Rep.* **473**, 51–87 (2009).

121. Ferrari, A. C. Raman spectroscopy of graphene and graphite: Disorder, electron–phonon coupling, doping and nonadiabatic effects. *Solid State Commun.* **143**, 47–57 (2007).

122. Casiraghi, C., Pisana, S., Novoselov, K. S., Geim, A. K. & Ferrari, A. C. Raman fingerprint of charged impurities in graphene. *Appl. Phys. Lett.* **91**, 233108 (2007).

123. Tuinstra, F. & Koenig, J. L. Raman Spectrum of Graphite. *J. Chem. Phys.* **53**, 1126–1130 (2003).

124. Ferrari, A. C. *et al.* The Raman Fingerprint of Graphene.

125. Ferrari, A. C. Raman spectroscopy of graphene and graphite: Disorder, electron–phonon coupling, doping and nonadiabatic effects. *Solid State Commun.* **143**, 47–57 (2007).

126. De Silva, K. K. H., Viswanath, P., Rao, V. K., Suzuki, S. & Yoshimura, M. New Insight into the Characterization of Graphene Oxide and Reduced Graphene Oxide Monolayer Flakes on Si-Based Substrates by Optical Microscopy and Raman Spectroscopy. *J. Phys. Chem. C* **125**, 7791–7798 (2021).

127. Lin, H., Cojal González, J. D., Severin, N., Sokolov, I. M. & Rabe, J. P. Reversible Switching of Charge Transfer at the Graphene–Mica Interface with Intercalating Molecules. *ACS Nano* **14**, 11594–11604 (2020).

128. Lee, J. E., Ahn, G., Shim, J., Lee, Y. S. & Ryu, S. Optical separation of mechanical strain from charge doping in graphene. *Nat. Commun.* **3**, 1024 (2012).

129. Stampfer, C. *et al.* Raman imaging of doping domains in graphene on Si O 2. *Appl. Phys. Lett.* **91**, 241907 (2007).

130. Ziem, B. *et al.* Size-dependent inhibition of herpesvirus cellular entry by polyvalent nanoarchitectures. *Nanoscale* **9**, 3774–3783 (2017).

131. Ziem, B. *et al.* Highly Efficient Multivalent 2D Nanosystems for Inhibition of Orthopoxvirus Particles. *Adv. Healthc. Mater.* **5**, 2922–2930 (2016).

132. Guday, G. *et al.* Scalable Production of Nanographene and Doping via Nondestructive Covalent Functionalization. *Small* **15**, 1805430 (2019).

133. Faghani, A. *et al.* Metal-Assisted and Solvent-Mediated Synthesis of Two-Dimensional Triazine Structures on Gram Scale. *J. Am. Chem. Soc.* **142**, 12976–12986 (2020).

134. Butt, H.-J. & Jaschke, M. Calculation of thermal noise in atomic force microscopy. *Nanotechnology* **6**, 1–7 (1995).

135. Calizo, I., Balandin, A. A., Bao, W., Miao, F. & Lau, C. N. Temperature Dependence of the Raman Spectra of Graphene and Graphene Multilayers. *Nano Lett.* **7**, 2645–2649 (2007).

136. Elveborg, S., Monteil, V. M. & Mirazimi, A. Methods of Inactivation of Highly Pathogenic Viruses for Molecular, Serology or Vaccine Development Purposes. *Pathogens* **11**, 271 (2022).

137. Lin, H. *et al.* Insight into the wetting of a graphene-mica slit pore with a monolayer of water. *Phys. Rev. B* **95**, 195414 (2017).

138. Shearer, C. J., Slattery, A. D., Stapleton, A. J., Shapter, J. G. & Gibson, C. T. Accurate thickness measurement of graphene. *Nanotechnology* **27**, 125704 (2016).

139. Jung, I. *et al.* Characterization of Thermally Reduced Graphene Oxide by Imaging Ellipsometry. *J. Phys. Chem. C* **112**, 8499–8506 (2008).

140. Rozada, R. *et al.* From graphene oxide to pristine graphene: revealing the inner workings of the full structural restoration. *Nanoscale* **7**, 2374–2390 (2015).

141. Carneiro, F. A. *et al.* Charged residues are involved in membrane fusion mediated by a hydrophilic peptide located in vesicular stomatitis virus G protein. *Mol. Membr. Biol.* **23**, 396–406 (2006).

142. Mastromarino, P., Conti, C., Goldoni, P., Hauttecoeur, B. & Orsi, N. Characterization of Membrane Components of the Erythrocyte Involved in Vesicular Stomatitis Virus Attachment and Fusion at Acidic pH. *J. Gen. Virol.* **68**, 2359–2369 (1987).

143. Carneiro, F. A., Bianconi, M. L., Weissmüller, G., Stauffer, F. & Da Poian, A. T. Membrane Recognition by Vesicular Stomatitis Virus Involves Enthalpy-Driven Protein-Lipid Interactions. *J. Virol.* **76**, 3756–3764 (2002).

144. Rudd, T. R. *et al.* Heparan sulphate, its derivatives and analogues share structural characteristics that can be exploited, particularly in inhibiting microbial attachment. *Braz. J. Med. Biol. Res.* **45**, 386–391 (2012).

145. Rabenstein, D. L. Heparin and heparan sulfate: structure and function. *Nat. Prod. Rep.* **19**, 312–331 (2002).

146. Sametband, M., Kalt, I., Gedanken, A. & Sarid, R. Herpes Simplex Virus Type-1 Attachment Inhibition by Functionalized Graphene Oxide. *ACS Appl. Mater. Interfaces* **6**, 1228–1235 (2014).

147. McMahon, H. T. & Gallop, J. L. Membrane curvature and mechanisms of dynamic cell membrane remodelling. *Nature* **438**, 590–596 (2005).

148. Voeltz, G. K., Prinz, W. A., Shibata, Y., Rist, J. M. & Rapoport, T. A. A class of membrane proteins shaping the tubular endoplasmic reticulum. *Cell* **124**, 573–586 (2006).

149. Vogel, V. & Sheetz, M. Local force and geometry sensing regulate cell functions. *Nat. Rev. Mol. Cell Biol.* **7**, 265–275 (2006).

150. Reynwar, B. J. *et al.* Aggregation and vesiculation of membrane proteins by curvature-mediated interactions. *Nature* **447**, 461–464 (2007).

151. Naikoo, G. A. *et al.* 2D materials, synthesis, characterization and toxicity: A critical review. *Chem. Biol. Interact.* **365**, 110081 (2022).

152. Yang, K. *et al.* The influence of surface chemistry and size of nanoscale graphene oxide on photothermal therapy of cancer using ultra-low laser power. *Biomaterials* **33**, 2206–2214 (2012).

153. Narita, A., Wang, X.-Y., Feng, X. & Müllen, K. New advances in nanographene chemistry. *Chem. Soc. Rev.* **44**, 6616–6643 (2015).

154. Chen, J., Li, Y., Huang, L., Li, C. & Shi, G. High-yield preparation of graphene oxide from small graphite flakes via an improved Hummers method with a simple purification process. *Carbon* **81**, 826–834 (2015).

155. Cançado, L. G. *et al.* Quantifying defects in graphene via Raman spectroscopy at different excitation energies. *Nano Lett.* **11**, 3190–3196 (2011).

156. Halbig, C. E. *et al.* Quantitative investigation of the fragmentation process and defect density evolution of oxo-functionalized graphene due to ultrasonication and milling. *Carbon* **96**, 897–903 (2016).

157. Neumann, C. *et al.* Raman spectroscopy as probe of nanometre-scale strain variations in graphene. *Nat. Commun.* **6**, 8429 (2015).

158. Ferrari, A. C. *et al.* Science and technology roadmap for graphene, related two-dimensional crystals, and hybrid systems. *Nanoscale* **7**, 4598–4810 (2015).

159. Yan, J., Zhang, Y., Kim, P. & Pinczuk, A. Electric field effect tuning of electron-phonon coupling in graphene. *Phys. Rev. Lett.* **98**, 166802 (2007).

160. Das, A. *et al.* Monitoring dopants by Raman scattering in an electrochemically top-gated graphene transistor. *Nat. Nanotechnol.* **3**, 210–215 (2008).

161. Setaro, A. *et al.* Preserving π-conjugation in covalently functionalized carbon nanotubes for optoelectronic applications. *Nat. Commun.* **8**, 14281 (2017).

162. Liu, M. *et al.* Crystalline Covalent Triazine Frameworks by In Situ Oxidation of Alcohols to Aldehyde Monomers. *Angew. Chem. Int. Ed.* **57**, 11968–11972 (2018).

163. Kuhn, P., Antonietti, M. & Thomas, A. Porous, Covalent Triazine-Based Frameworks Prepared by Ionothermal Synthesis. *Angew. Chem. Int. Ed.* **47**, 3450–3453 (2008).

164. Algara-Siller, G. *et al.* Triazine-Based Graphitic Carbon Nitride: a Two-Dimensional Semiconductor. *Angew. Chem. Int. Ed.* **53**, 7450–7455 (2014).

165. Guo, X. *et al.* Mechanistic Insight into Hydrogen-Bond-Controlled Crystallinity and Adsorption Property of Covalent Organic Frameworks from Flexible Building Blocks. *Chem. Mater.* **30**, 2299–2308 (2018).

166. Liu, M., Guo, L., Jin, S. & Tan, B. Covalent triazine frameworks: synthesis and applications. *J. Mater. Chem. A* **7**, 5153–5172 (2019).

167. Wang, K. *et al.* Covalent Triazine Frameworks via a Low-Temperature Polycondensation Approach. *Angew. Chem. Int. Ed.* **56**, 14149–14153 (2017).

168. Mortensen, J. J., Hansen, L. B. & Jacobsen, K. W. Real-space grid implementation of the projector augmented wave method. *Phys. Rev. B* **71**, 035109 (2005).

169. Enkovaara, J. *et al.* Electronic structure calculations with GPAW: a real-space implementation of the projector augmented-wave method. *J. Phys. Condens. Matter* **22**, 253202 (2010).

170. Marques, M. A. L., Oliveira, M. J. T. & Burnus, T. Libxc: A library of exchange and correlation functionals for density functional theory. *Comput. Phys. Commun.* **183**, 2272–2281 (2012).

171. Ghasemi, J. & Shamsipur, M. Fluorimetric Study of Complexation of Alkali and Alkaline Earth Cations with 1,10-Phenanthroline, 2,2′-Bipyridine and 8-Hydroxyquinoline in Nonaqueous Solvents. *J. Coord. Chem.* **26**, 337–344 (1992).

172. Murugavel, R. & Korah, R. Structural Diversity and Supramolecular Aggregation in Calcium, Strontium, and Barium Salicylates Incorporating 1,10-Phenanthroline and 4,4‘-Bipyridine: Probing the Softer Side of Group 2 Metal Ions with Pyridinic Ligands. *Inorg. Chem.* **46**, 11048–11062 (2007).

173. Mitchell, P. R. & Sigel, H. Ternary complexes in solution. 28. Enhanced stability of ternary metal ion/adenosine 5’-triphosphate complexes. Cooperative effects caused by stacking interactions in complexes containing adenosine triphosphate, phenanthroline, and magnesium, calcium, or zinc ions. *J. Am. Chem. Soc.* **100**, 1564–1570 (1978).

174. Noro, S. *et al.* Porous coordination polymers with ubiquitous and biocompatible metals and a neutral bridging ligand. *Nat. Commun.* **6**, 5851 (2015).

175. Ferrari, A. C. & Robertson, J. Raman spectroscopy of amorphous, nanostructured, diamond–like carbon, and nanodiamond. *Philos. Trans. R. Soc. Lond. Ser. Math. Phys. Eng. Sci.* **362**, 2477–2512 (2004).

176. Suter, T. *et al.* Synthesis, Structure and Electronic Properties of Graphitic Carbon Nitride Films. *J. Phys. Chem. C* **122**, 25183–25194 (2018).

177. Cataldo, F. The role of Raman spectroscopy in the research on sp-hybridized carbon chains: carbynoid structures polyynes and metal polyynides. *J. Raman Spectrosc.* **39**, 169–176 (2008).

178. Wang, J. *et al.* Identifying sp–sp2 carbon materials by Raman and infrared spectroscopies. *Phys. Chem. Chem. Phys.* **16**, 11303–11309 (2014).

179. Komine, C. & Tsujimoto, Y. A small amount of singlet oxygen generated via excited methylene blue by photodynamic therapy induces the sterilization of Enterococcus faecalis. *J. Endod.* **39**, 411–414 (2013).

180. Sumitani, M., Takagi, S., Tanamura, Y. & Inoue, H. Oxygen indicator composed of an organic/inorganic hybrid compound of methylene blue, reductant, surfactant and saponite. *Anal. Sci. Int. J. Jpn. Soc. Anal. Chem.* **20**, 1153–1157 (2004).

8. Publications

8.1. Scientific Articles

1. Gholami, M. F., Lauster, D., Ludwig, K., Storm, J., Ziem, B., Severin, N., Böttcher, C., Rabe, J. P., Herrmann, A., Adeli, M., Haag, R. 2017. »Functionalized Graphene as Extracellular Matrix Mimics: Toward Well-Defined 2D Nanomaterials for Multivalent Virus Interactions.« Advanced Functional Materials, 27, (15): 1606477. https://doi.org/10.1002/adfm.201606477

2. Mohammadifar, E., Ahmadi, V., Gholami, M. F., Oehrl, A., Kolyvushko, O., Nie, C., Donskyi, I. S., Herziger, S., Radnik, J., Ludwig, K., Böttcher, C., Rabe, J. P., Osterrieder, K., Azab, W., Haag, R., Adeli, M. 2021. »Graphene-Assisted Synthesis of 2D Polyglycerols as Innovative Platforms for Multivalent Virus Interactions.« Advanced Functional Materials, 31, 2009003. https://doi.org/10.1002/adfm.202009003

3. Picht, T., Calvé, M. L., Tomasello, R., Fekonja, L., Gholami, M. F., Bruhn, M., Zwick, C., Rabe, J. P., Müller-Birn, C., Vajkoczy, P., Sauer, I. M., Zachow, S., Nyakatura, J. A., Ribault, P., Pulvermüller, F. 2021. »Letter: A Note on Neurosurgical Resection and Why We Need to Rethink Cutting.« Neurosurgery, nyab326. https://doi.org/10.1093/neuros/nyab326

4. Faghani, A., Gholami, M. F., Trunk, M., Müller, J., Pachfule, P., Vogl, S., Donskyi, I., Li, M., Nickl, P., Shao, J., Huang, M. R. S., Unger, W. E. S., Arenal, R., Koch, C. T., Paulus, B., Rabe, J. P., Thomas, A., Haag, R., Adeli, M. 2020. »Metal-Assisted and Solvent-Mediated Synthesis of Two-Dimensional Triazine Structures on Gram Scale.« Journal of the American Chemical Society, 142, (30): 12976-12986. https://doi.org/10.1021/jacs.0c02399

5. Beyranvand, S., Gholami, M. F., Tehrani, A. D., Rabe, J. P., Adeli, M. 2019. »Construction and Evaluation of a Self-Calibrating Multiresponse and Multifunctional Graphene Biosensor.« Langmuir, 35, (32): 10461-10474. https://doi.org/10.1021/acs.langmuir.9b00915

6. Guday, G., Donskyi, I. S., Gholami, M. F., Algara-Siller, G., Witte, F., Lippitz, A., Unger, W. E. S., Paulus, B., Rabe, J. P., Adeli, M., Haag, R. 2019. »Scalable Production of Nanographene and Doping via Nondestructive Covalent Functionalization.« Small, 15, (12): 1805430. https://doi.org/10.1002/smll.201805430

7. Faghani, A., Donskyi, I. S., Fardin Gholami, M., Ziem, B., Lippitz, A., Unger, W. E. S., Böttcher, C., Rabe, J. P., Haag, R., Adeli, M. 2017. »Controlled Covalent Functionalization of Thermally Reduced Graphene Oxide To Generate Defined Bifunctional 2D Nanomaterials.« Angewandte Chemie International Edition, 56, (10): 2675-2679. https://doi.org/10.1002/anie.201612422

8. Lin, W., Gholami, M. F., Beyer, P., Severin, N., Shao, F., Zenobi, R., Rabe, J. P. 2017. »Strongly enhanced Raman scattering of Cu-phthalocyanine sandwiched between graphene and Au(111).« Chemical Communications, 53, (4): 724-727. https://doi.org/10.1039/c6cc08672a

9. Ziem, B., Azab, W., Gholami, M. F., Rabe, J. P., Osterrieder, N., Haag, R. 2017. »Sizedependent inhibition of herpesvirus cellular entry by polyvalent nanoarchitectures.« Nanoscale, 9, (11): 3774-3783. https://doi.org/10.1039/c7nr00611j

10. Ziem, B., Thien, H., Achazi, K., Yue, C., Stern, D., Silberreis, K., Gholami, M. F., Beckert, F., Gröger, D., Mülhaupt, R., Rabe, J. P., Nitsche, A., Haag, R. 2016. »Highly Efficient Multivalent 2D Nanosystems for Inhibition of Orthopoxvirus Particles.« Advanced Healthcare Materials, 5, (22): 2922-2930. https://doi.org/10.1002/adhm.201600812

11. Talyzin, A. V., Klechikov, A., Korobov, M., Rebrikova, A. T., Avramenko, N. V., Gholami, M. F., Severin, N., Rabe, J. P. 2015. »Delamination of graphite oxide in a liquid upon cooling.« Nanoscale, 7, (29): 12625-12630. https://doi.org/10.1039/c5nr02564h

8.2. Books & Chapters

1) Gholami, Mohammad Fardin, Guiducci, Lorenzo, Jany, Susanne and Razghandi, Khashayar. "Rethinking Active Matter: Current Developments in Active Materials: 1 What Is Activity? An Introduction". Active Materials, edited by Peter Fratzl, Michael Friedman, Karin Krauthausen and Wolfgang Schäffner, Berlin, Boston: De Gruyter, 2022, pp. 191-222. https://doi.org/10.1515/9783110562064-011

2) Gholami, Mohammad Fardin/Severin, Nikolai/Rabe, Jürgen P. (2016). Folding of Graphene and Other Two-dimensional Materials. In: Michael Friedman/Wolfgang Schäffner (Eds.), On Folding (211-242). Bielefeld: transcript Verlag. https://doi.org/10.14361/9783839434048-009

8.3. Patents

a) Mohammed Fardin Gholami, Nikolai Severin, Jürgen P. Rabe, Vitalij Scenev 2013. Coating means for producing an electrically conductive layer and process for its preparation. DE102013225904B4 issued on 29 September 2016.

b) Vitalij Scenev, Jürgen P. Rabe, Nikolai Severin, Mohammad Fardin Gholami, Egon Steeg 2013. Coating agent, method for producing a coating agent and an electrically conductive layer and component with layer. DE102013225902B4 issued on 14 January 2021.

9. Acknowledgements

Performing a doctoral research and study along with writing a doctoral dissertation is not a stand-alone thing and requires the cooperation and collaborations of a more than just one person. From the scientific and project-related point of view I would like to begin my greetings: First and foremost, I would like to thank **Prof. Dr. Jürgen P. Rabe**, for giving me the opportunity to work on the fascinating and challenging topic of two-dimensional carbon-based materials in his multinational group. I sincerely thank the endless supports I received from him during my work. I am thankful for the great freedom and independence I was given for duration of my doctoral work which resulted in learning the critical importance of scientific language, diplomacy and communication in academia and science. I would like to express my gratitude to **Dr. Stefan Kirstein** for invaluable scientific discussions, his inputs and smart ideas in addition to his careful attention to experimental details and publications, most importantly I thank him for introducing me to the group of Prof. Rabe.

Additionally, I like to acknowledge the great and constructive feedback from the **Prof. Dr. Oliver Benson**, **Prof. Dr. Dieter Neher** and **Prof. Dr. Jürgen P. Rabe** regarding as the reviewers of this body of research and further extend my gratitude to Prof. Dr. Igor Sokolov for his guidance and scientific teachings in the process of preparation for my doctoral defense.

Furthermore, I would like to acknowledge and thank **Prof. Dr. Rainer Haag** from the Organic chemistry department of Freie Universität Berlin who provided the great opportunity for me to investigate the materials synthesized in his group and contributed with key ideas and fruitful discussions and for introducing me to **Prof. Dr. Mohsen Adeli**. From The group of Prof. Haag and Prof. Adeli, I would like to specially thank my best friend **Dr. Abbas Faghani** and **Dr. Benjamin Ziem** with their enormous effort put into the synthesis of such remarkable materials.

I am very grateful to **Dr. Nikolai Severin** for his teachings and providing helpful scientific discussions over some projects. The generous help of Physik von Makromolekülen (PMM) group members **Evi Poblenz, Sabine Schönherr, Sylwia Bojarzen**. I also would like to thank **Dr. Wiebke Fischer** for the great helps and discussions during my research. Special thanks to and my gratitude (in no particular

order) to Johannes Müller, Dr. Wang-Ing Lin, Martin Bogner, Dr. Vitalij Scenev, Dr. Philipp Lange, Dr. Manuel Gensler, Simon Gabaj, Dr. Omar Al-Khatib, Abdul Rauf, Dr. Hu Lin.

Finally, yet importantly, I would like to mention my deepest gratitude to my parents and family members for all their encouragement. I would like to close the acknowledgments with words of love for my dearest Mother, Father and my Brother, **Maryam Hezarkhani**, **Dr. Siamak Gholami and Mohammad Farzin Gholami**.

10. Declaration (Eidesstattliche Erklärung)

Hereby, I announce and confirm this PhD thesis is completely the outcome of my own work and that no other sources than those cited have been used. All annotations, which have been used from published or unpublished sources, are identified as such. The shown illustrations have been created by myself or have been marked with the corresponding references.

The experimental work has been conducted by myself, the in vitro experimentation and material synthesis were done by my colleagues at Humboldt University of Berlin and Freie university of Berlin and were acknowledged in the text. Results contained in this thesis were published and referenced as such.

I have not applied for a doctor's degree in the doctoral subject elsewhere and do not hold a corresponding doctoral degree. I have taken due note of the Faculty of Mathematics and Natural Sciences Ph.D. Regulations, published in the Official Gazette of Humboldt-Universität zu Berlin No. 42/2018 on 11/07/2018.

Mohammad Fardin Gholami

Berlin, 31.03.2023

11. Appendix

11.1. Elemental analysis on the Triazine content of TRGO-Trz (Degree of functionalization)

Table 11.1, Nitrogen content of the functionalized and non-functionalized graphene derivatives. Adopted from reference [32].

Compound	*N%*	*C%*	*H%*	*S%*
Pristine TRGO	*0.058*	*87.75*	*1.74*	*0*
TRGO-Trz @ 25 °C	*2.70*	*82.1*	*0.52*	*0*
TRGO-Trz @ 75 °C	*6.5*	*75.72*	*0.111*	*0*